

Masters Thesis

**Geological characterization and genetic aspects of
the Mafengzhen magnesite deposit
(Haicheng, Liaoning Province, NE China)**

Hannes Pluch



Leoben am 21. March 2013

Lehrstuhl für Geologie und Lagerstättenlehre
Department Angewandte Geowissenschaften und Geophysik
Montanuniversität Leoben

A-8700 LEOBEN, Peter-Tunner-Straße 5

Telefon: +43/(0)3842-402-6101

Fax: +43/(0)3842-402-6102

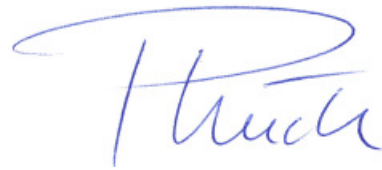
geologie@unileoben.ac.at

Affidavit

I declare in lieu of oath that I wrote this thesis and performed the associated research myself, using only literature cited in this volume.

21.03.2013

Date

A handwritten signature in blue ink, appearing to read 'Huck', written above a horizontal line.

Signature

ABSTRACT

The Aihai magnesite deposit near Haicheng (Liaoning Province, NE China) is part of the Yingke magnesite ore belt with numerous giant magnesite and talc deposits. This ore belt consists of early Proterozoic metamorphic rock series of Mg-rich carbonate formations which occur stratabound in the third section of the Dashiqiao Formation of the Liaohe Group. The Liaohe Group represents a low grade metamorphic (greenschist - lower amphibolite) volcano-sedimentary facies embedded in the Paleoproterozoic Jiao-Liao-Ji Belt at the eastern margin of the North China Craton. The North Liaohe Group is conventionally divided into four formations. The uppermost Dashiqiao formation can be sub classified into three sections. The third section consists dominantly of dolomite marbles intercalated with minor carbonaceous slates and hosting the largest magnesite deposits in the world.

The magnesite ore bodies are distributed in an area of 100 km in length 4 km width. The NE trending Aihai ore body is underlain by mica schists and intercalations of thinly bedded dolomitic marble. The ore displays metasomatic transitions to the dolomite host rocks. Occasionally the ore is interbedded with siliceous green marble. In the late Jurassic lamprophyre dyke swarms intruded the Aihai magnesite deposit, but show no concomitant alteration of the magnesite ore. The deposit is crosscut by faults hosting younger magnesite sinter. The sparry magnesite varies in colour from white, white-pink, white-yellow, white-grey and grey. The mineral crystal sizes are finely grained (< 0,5 cm) to coarsely grained (1,0 - 5,0 cm). In special parts of the deposits exceptional giant crystals up to 15cm are found. Associated mineral phases are talc, Mg-chlorite, tremolite, diopside, pyrite, graphite, and others.

Selectively mined magnesite has 46.89 wt. % of MgO, 0.93 % of CaO, 0.99 % of SiO₂, 0,44 % of Fe₂O₃ (total) and an LOI of 50.78 wt. %. The lowest MgO contents occur in the transition zones to the dolomitic marbles and in younger brittle shear zones. In turn CaO shows highest values at the contacts to the dolomitic marbles. The variation of CaO is explainable by late redolomitization and relics of dolomite inclusions. Redolomitization is mainly caused by descending surface water through

young brittle shear zones. The SiO₂ variations are caused by talc/Mg-chlorite in tension gashes and some quartz in micro joints. The silicate hosted elements Zr, Y, V, Si and Al are positively correlated. Cr and Ni are below the detection limit of 20 ppm in all magnesite samples. Most of the Aihai open pit meta-carbonates have atypical seawater-like REE+Y patterns with depleted HREE, abundant LREE and unincisive Ce anomalies. SiO₂ derives from metamorphic fluids.

The hanging wall dolomites have $\delta^{13}\text{C}_{\text{PDB}} (\text{‰})$ ratios ranging from +1,16 to +1,71 and $\delta^{18}\text{O}_{\text{SMOW}} (\text{‰})$ values from +18,37 to +20,59. Massive magnesites from the ore bed yield $\delta^{13}\text{C}_{\text{PDB}} (\text{‰})$ and $\delta^{18}\text{O}_{\text{SMOW}} (\text{‰})$ compositions of +0,01 to +1,02 and +9,47 to 11,24, respectively. The depletions of $\delta^{13}\text{C}_{\text{PDB}}$ and $\delta^{18}\text{O}_{\text{SMOW}}$ in magnesites relative to dolomites is interpreted to be the result of regional metamorphism-related hydrothermal alteration which resulted in rock recrystallization and mass exchange. This interpretation can be furthered by the younger magnesite sinter. The magnesite sinter yields $\delta^{13}\text{C}_{\text{PDB}} (\text{‰})$ and $\delta^{18}\text{O}_{\text{SMOW}} (\text{‰})$ values between -2,69 and +13,26, showing lower $\delta^{13}\text{C}_{\text{PDB}}$ and higher $\delta^{18}\text{O}_{\text{SMOW}}$ than the massive magnesite. This result supports the assumption of low temperature, meteoric, low $\delta^{13}\text{C}$ fluids interaction with massive magnesite after ore formation.

Precipitation and biogenic sedimentation generated the carbonate host rocks in the Dashiqiao Formation. They underwent hydrothermal metasomatism during the early stage of the Lüliang movement (orogeny). The mineralizing fluids came from lagoonal or diagenetic brines, which percolated down along fractures and faults to replace under-laying permeable platform carbonates. The impermeable metasediment bedrock (2nd Dashiqiao Section) caused the limited occurrence of magnesite in the third section of the Dashiqiao Formation. During the Lüliang movement the Liaohé Group was folded, regionally metamorphosed at greenschist to amphibolite facies conditions transforming the carbonates to dolomitic marble and coarsely grained magnesite marble. In the metamorphic epoch, late in the early Proterozoic, minerogenic buried seawater and brines were mobilized too. They metasomatized the Mg-rich carbonates to form some new pure magnesite bodies and veins.

Considering a thirty year mine plan, in total 21.948 million tons (Volume = 7.44 million m³) of ore can be mined. These resources can be sub-divided into 4.45 million tons of Indicated Resources and in 17.5 million tons of Inferred Resources. The calculation of Indicated Resources is based on geological field investigations and on actual mining data.

TABLE OF CONTENTS

1	Geographical Overview	1
1.1	Geological setting	2
1.1.1	Overview	2
1.1.2	North China Craton (NCC)	3
1.1.3	Tectonic subdivision and the tectonic belts	5
1.1.4	Liaohe Group	8
2	Magnesite Deposits China	12
2.1	Genetic Models	16
2.2	Geological frame and the genetic models for the giant magnesite deposits in the Haicheng-Dashiqiao district	18
3	Petrography and texture of host rocks, magnesite ore and late mineralizations	27
3.1	Micaschist	28
3.2	Thinly banded dolomite marble	32
3.3	Siliceous green banded calcite marble	34
3.4	High-Mg potassic lamprophyre dykes	38
3.5	White fine-grained magnesite	40
3.6	Grey fine-grained magnesite	42
3.7	Dark medium-grained magnesite, containing talc and Mg-chlorite	44
3.8	Dark grey/white mottled magnesite	46
3.9	Magnesite sinter veins	48
3.10	Talc/Mg-chlorite bound to tectonized zones	50
3.11	Fibrous sepiolite on slickenside surfaces	51
4	Geochemistry of the magnesite ore and the related rocks	53
4.1	Major Elements	53
4.1.1	Magnesite ore	55
4.1.2	Carbonaceous schists (siliceous green marble)	56
4.1.3	Dolomitic marbles	56
4.1.4	Micaschists with calcite inclusions	56
4.1.5	Lamprophyre dikes	56
4.2	Trace Elements	60

4.3	Rare earth elements (REE)	62
4.4	Stable isotope geochemistry	71
5	Magnesite 3D deposit model	80
5.1	Gemcom Surpac.....	81
5.2	Modeling of the magnesite deposit.....	82
5.3	Geostatistics: Inverse Distance vs. Ordinary Kriging	86
5.4	Magnesite resource calculation	96
6	Discussion	101

FIGURES

Figure 1: (a) Geographical map of NE China, red box marks the enlarged area (b). (b) Detailed geographic map showing the position of the Aihai open pit magnesite mining operation (red star) and the two villages Qushugou and Mafengzhen (red boxes).....	1
Figure 2: Map of the Paleoproterozoic Jiao-Liao-Ji Belt in the Eastern Block of the North China Craton showing the Northern Liaoning-Southern Jilin Complex, Southern Liaoning-Nangrim Complex and the Eastern Shandong Complex (modified from Zhao et al.,1998).....	3
Figure 3: Overview map of the three-fold tectonic subdivision of the NCC showing the southern border of Central Asian Orogenic Belt (CAOB), Central China Orogen (CCO), Trans North China Orogen (TNCO), Western Block (WB), and Eastern Block (EB). The red star marks the position of the Haicheng-Dashiqiao magnesite ore belt (modified after Li et al., 2011).	4
Figure 4: Map of the tectonic subdivision of the Archean to Paleoproterozoic basement of the NCC; the red star shows the position of the Haicheng magnesite district (Zhao et al., 2005).	5
Figure 5: P-T-t paths of the Liaohe Group and its equivalents.①,④, after Li et al. (2001);②,⑥ after He and Ye (1998);③,⑤ modified after Lu et al. (1996). 1—Archean basement; 2—Palaeoproterozoic granite; 3—Neoproterozoic strata; 4—Liaohe Group and equivalent; 5—major faults; 6—Mesozoic plutons; 7—Mesozoic strata. Ky—Kyanite; And—Andalusite; Sill—Sillimanite.....	7
Figure 6: Distribution of the Paleoproterozoic Liaohe assemblage and Liaoji granitoids. MDSZ: major detachment shear zone; QZSZ: Qinglongshan–Zaoerling shear zone (modified after Li et al., 2004).	9
Figure 7: Simplified profile of vertical stratification of the metamorphic Liaohe Group. 1-Archean basement, 2-Paleoproterozoic layered granite, 3-kyanite/staurolite zone, 4- garnet/tremolite zone, 5-biotite chlorite zone(lower-T talc zone), 6-andalusite-cordierite or, 7-main sliding zones,8- bedding-parallel structural plane and sence of ductile sliding (Li et al., 1998).	10

Figure 8: Lithostratigraphic units of the North and South Liaohe Groups (after Luo et al, 2006).....	11
Figure 9: World magnesite resource distribution (modified after Wilson & Ebner, 2005).	12
Figure 10: Magnesite mined in the world (2009) (Weber et al. 2011)	13
Figure 11: The diagram shows the annual magnesite production between 2003 and 2009 (Weber et al. 2011).	14
Figure 12: Aerial image of the Yingke ore belt (Dashiqiao-Haicheng Magnesite District). Red boxes mark areas with great numbers of magnesite (talc) producers and the investigation area.....	15
Figure 13: Tetrahedral solid solution field of the trigonal calcite- and dolomite series. 1 Dolomite, 2 Huntite, 3 Kutnahorit (Godovikov, 1975).....	16
Figure 14: Simplified geological map of the Haicheng-Dashiqiao (Yingke) magnesite ore belt (modified after Jiang et al., 2004).	19
Figure 15: Lamprophyre dikes in the Aihai magnesite open pit.	21
Figure 16: Model of the sedimentary environment from the Haicheng-Dashiqiao ore district (modified after Chen &Cai, 2000).	22
Figure 17: Model of the compression of the Liaohe Group, caused by the Lüliang movement (modified after Chen &Cai, 2000).	23
Figure 18: Geological map showing the tectonic subdivision for the early Proterozoic rift system and magnesite/talc deposits (modified from Chen & Wang,1994). 1: Archean craton; rift areas (2-4); 2: north slope zone; 3: inner depression zone; 4: shallow zone; 5: mantle uplift; 6: boundary (deep fault) of tectonic zones; 7: shear fault; 8: extension fault; 9: basic rock; 10: interred uplift; mineral deposits (11-17); 11: boron; 12: talc; 13: serpenite (Xiuyan jade); 14: brucite; 15: diopside and tremolite; 16: clinochlorite; 17: fibrous sepiolite	24
Figure 19: Minerogenic system of the magnesite deposits in the Dashiqiao Formation. * The peak of the metamorphic event is 1.9 Ga. Associated mineral phases from the different stages: 1) calcite, dolomite, magnesite; 2) magnesite, dolomite; 3) talc (genesis of the talc deposits), magnesite, dolomite, serpentine, diopside, tremolite, clinochlorite; 4) fibrous sepiolite.....	26
Figure 20: Geological cross section of the Aihai Magnesite open-pit.	27
Figure 21: Tectonized border between micaschist and magnesite ore layers.	28

Figure 22: Calcite veins and small bodies in the micaschist.	29
Figure 23: (a) typical rusty brown micaschist; (b) micaschist with calcite veins.	30
Figure 24: Microscope image of the micaschist (image length 4x)	31
Figure 25: Micaschist with calcite veins (image length 4x).	32
Figure 26: Folded banded dolomite marble outcrop.	33
Figure 27: Thinly banded dolomite marble, with clayey intercalations.	33
Figure 28: Photomicrograph of banded dolomite (image length 10x).	34
Figure 29: Siliceous green banded marble, with streaky-wavy structure in the lower part of the image.	35
Figure 30: Banded marble with alternating light and gray layers.	36
Figure 31: Calcite with accessory tremolite. (4x)	37
Figure 32: Transition between gray and light layers (4x).	38
Figure 33: Greenish black groundmass with phenocrysts (black dots).	39
Figure 34: Discordant lamprophyre dyke (bench face). Dyke thickness 1,5m.	39
Figure 35: Typical lamprophyric (panidiomorphic) texture (4x).	40
Figure 36: White fine-grained magnesite outcrop, with magnesite sinter veins crosscutting dark grey magnesit.	41
Figure 37: Polished specimen from the white fine-grained magnesite. Sugar like crystal-structure.	41
Figure 38: Photomicrograph of the white fine-grained magnesite. A points to relatively coarse crystals with no inclusions; B marks coarse crystals with inclusions of dolomitic relics; C indicates fine crystals of undulatory extinction. (4x).	42
Figure 39: Grey fine-grained magnesite outcrop with stylolites.	43
Figure 40: Polished specimen of pure magnesite with slightly lighter and darker areas.	43
Figure 41: Photomicrograph of the grey fine-grained magnesite. Coarser crystals with dolomitic inclusions and finer crystals, which are interlocking along their boundaries (10x).	44
Figure 42: Dark medium grained magnesite, with tension gashes, which are filled with talc and Mg-chlorite.	45
Figure 43: Polished hand specimen of dark medium grained magnesite with tension gash. A shows the dark intact magnesite rock. B displays the core of the refilled	

material, mainly talc. C represents the border zones of the vein, which consist of talc and Mg-chlorite.....	45
Figure 44: (a) Talc and Mg-chlorite intergrowth (10x). (b) Talc and magnesite intergrowth (4x).....	46
Figure 45: Outcrop of the dark grey/white mottled magnesite with talc filled tension gashes.....	47
Figure 46: Polished specimen with irregular zebra replacement bands.....	47
Figure 47: Photomicrograph of mottled magnesite. A represents the coarse magnesite crystals with dolomitic inclusions. B Graphite. C Primary autogenous quartz.(10x)	48
Figure 48: Outcrop of high quality ore with magnesite sinter veins.....	49
Figure 49: Polished specimen of a magnesite breccia. The magnesite clast is overgrown by magnesite sinter.....	49
Figure 50: (a)+(b) Photomicrographs of magnesite sinters, illustrating the different crystallization stages. (4x)	50
Figure 51: Talc/Mg-chlorite hosting shear zone.....	51
Figure 52: Fibrous sepiolite on a slickenside surface.	52
Figure 53: Total Fe ₂ O ₃ +SiO ₂ -CaO-MgO ternary diagram for meta-carbonate rocks from the magnesite Aihai open-pit (thirdsection of the Dashiqiao Formation). Open red circles – magnesiteore, open red circle with cross – magnesitic marble with talc/Mg-chlorite, blue triangle – dolomitic marbles, green rectangle with cross – carbonaceous slates.....	57
Figure 54: MgO-Fe ₂ O ₃ variation diagram of dolomite host rocks and magnesite ore in the Aihai magnesite open-pit. Open red circles – magnesiteore, open red circle with cross – magnesite marble with talc/Mg-chlorite, blue triangle – dolomite marbles. Red ellipsoid – high iron subdomain and blue ellipsoid – low iron subdomain.....	58
Figure 55: MnO-Fe ₂ O ₃ variation diagram of dolomite host rocks and magnesite ore in the Aihai magnesite open-pit. Open red circles – magnesite ore, open red circle with cross – magnesitic marble with talc/Mg-chlorite, blue triangle – dolomitic marbles.....	59
Figure 56: Variation diagrams and their correlation coefficients between SiO ₂ , Al ₂ O ₃ , K ₂ O and TiO ₂ from all magnesite samples.	60

Figure 57: Positive correlation ($r = 0.52$) between the Al_2O_3 content and the total LREE content. Open red circles – magnesite ore, blue triangles – dolomitic marble. 65

Figure 58: Shale normalized REE+Y patterns of the Dashiqiao Formation magnesite ore. (a) Almost uncontaminated magnesite ore. (b) Magnesite ore adjunct to brittle faults. (c) Magnesite ore precipitated in fissures. 67

Figure 59: Shale normalized patterns of the dolomitic host rock. 68

Figure 60: normalized patterns of the carbonaceous schists. 69

Figure 61: Shale normalized patterns of the mica schist (9-1) and the mica schist with calcite inclusion (9-2). 69

Figure 62: C and O isotope data of host rock marbles and magnesites from the magnesite deposits in eastern Liaoning province. 73

Figure 63: C and O isotope variations of selected carbonates from the Aihai magnesite open pit. The groups represent the Mclust cluster. 77

Figure 64: Plot of $\delta^{13}C$ vs. $\delta^{18}O$ comparing the Dashiqiao Formation results with magnesites from other deposits. Data are from: Coorong Lagoon, South Australia (Zachmann, 1989); Lagoon, Adelaide, South Australia (Botz & von der Borch, 1984); magnesite deposits of Yugoslavia (Fallick et al., 1991); Serbia sedimentary magnesites (Kralik et al., 1989); Eugui, Spain, Carboniferous, coarse-grained, spar magnesite (Kralik & Hoefs, 1978); Adelaide Syncline, Copper Claim, Australia, Neoproterozoic, fine-grained, banded magnesite (Lambert et al., 1984); Rum Jungle, Northern Territory, Australia, Paleoproterozoic, coarse-grained, spar magnesite (Aharon, 1988); Barton, Zimbabwe, Archaean, fine-grained, banded magnesite (Perry & Tan, 1972). 79

Figure 65: 3D computer model of the Aihai magnesite deposit. View to the SW. 81

Figure 66: Drillholes with different ore grades from the open pit area. View to SSW. Green → ore zones, Blue → dolomite, Black → drillcore “lost”. 82

Figure 67: Ore strings showing the partition of the magnesite deposit. The brown plane adumbrates the magnesite footwall. View to the NNW. 83

Figure 68: Solid model of the Aihai magnesite deposit. View to the SE. 84

Figure 69: Constraint block model of the Aihai magnesite deposit. View to SW. 85

Figure 70: Digital terrain model (DTM) of the surface with 10m contour lines (grey). Green: natural landscape; grey: mining area; red dashed line: outline of the

concession area; blue: bench toes; red: bench crests; light green: hauling roads, orange dashed lines	86
Figure 71: Histograms representation of all available chemical data of the ore drill cores. Data outside the ore body are neglected and handled as waste material.....	88
Figure 72: Surpac window with variogram calculation parameters calculation of the MgO distribution. Dip direction of the ore body 200°; dip 50° and the full spread angle is 90°	89
Figure 73: Variogram model of the MgO distribution. Green line → variance; Red line → variogram model; Black line → experimental variogram; Blue points → variogram structure.....	90
Figure 74: Drill hole section inside the ore body showing the MgO grades [%].	91
Figure 75: Search ellipsoid parameters.	92
Figure 76: (a) Block model of the Aihai magnesite deposit; colored blocks were assigned quality grades through IDS estimation. Grey blocks are not affected by the IDS weighting, because they are outside of the search ellipsoid and (b) shows only the estimated blocks. It is obvious that the predicted blocks are accumulated around the drill holes where nearby data are available. The block colors according to MgO content. Red → MgO ≥47%; Orange → MgO 46-47%; Yellow → MgO 45-46%; Green → MgO 43-45%; Blue → MgO 41-43%. Red dashed lines are section lines (Figure 77). View to the SW.....	94
Figure 77: Vertical sections of the block model with drill-holes (color code see Figure 12). The green planes display the topographical surface.	95
Figure 78: The general relationship between exploration results, mineral resources and ore reserves (AusIMM, 2005).	96
Figure 79: (a) Actual open pit situation. (b) Long term mine plan with the ultimate pit design after 30 years. Proposed pit bottom is 200m above sea level then. (c) Ultimate pit design including the block model. Red → magnesite ore; Blue → overburden. (d) Ultimate pit design with the mineable magnesite ore, displayed as red blocks.....	98
Figure 80: North-South cross section of the ultimate pit design, showing two different overall slope angles.	99
Figure 81: The diagram shows the ore/waste ratios for the different elevation steps (10m ranges).	100

TABLES

Table 1: Major elements [%] analyses from the rock samples;*younger magnesite precipitation in fissures (magnesium sinter);** rock samples adjunct to faults.....	55
Table 2: REE analyses (ppm) of host rocks and magnesite from the Aihai magnesite open-pit; *younger magnesite precipitation in fissures (magnesium sinter);** rock samples adjunct to faults.	64
Table 3: C and O isotope data of host rocks and magnesite ores of the eastern Liaoning province.	73
Table 4: C and O isotope data of selected carbonates from the Aihai magnesite open pit. The group ID represents the Mclust cluster.	76
Table 5: Comparative review of methods of design and modeling in mining and geology (Miladinovic et al., 2011).	80
Table 6: Grades of magnesite ore (Standard → Liaoning Geological Survey Bureau).	93

Geographical Overview

The Aihai magnesite open-pit is located 0,5 kilometer in the NE of the small village Qushugou. Mafengzhen is the adjacent larger village, which is in the Haicheng district in eastern Liaoning Province of China (Figure 1).

The geographical longitude of the open pit mining is $123^{\circ}01'49'' \sim 123^{\circ}02'11''$ and the degree of latitude is $40^{\circ}47'11'' \sim 40^{\circ}47'32''$. The bottom of the open-pit is 300 meters above sea level and the highest point of the open pit has an elevation of 460 meters above sea level.

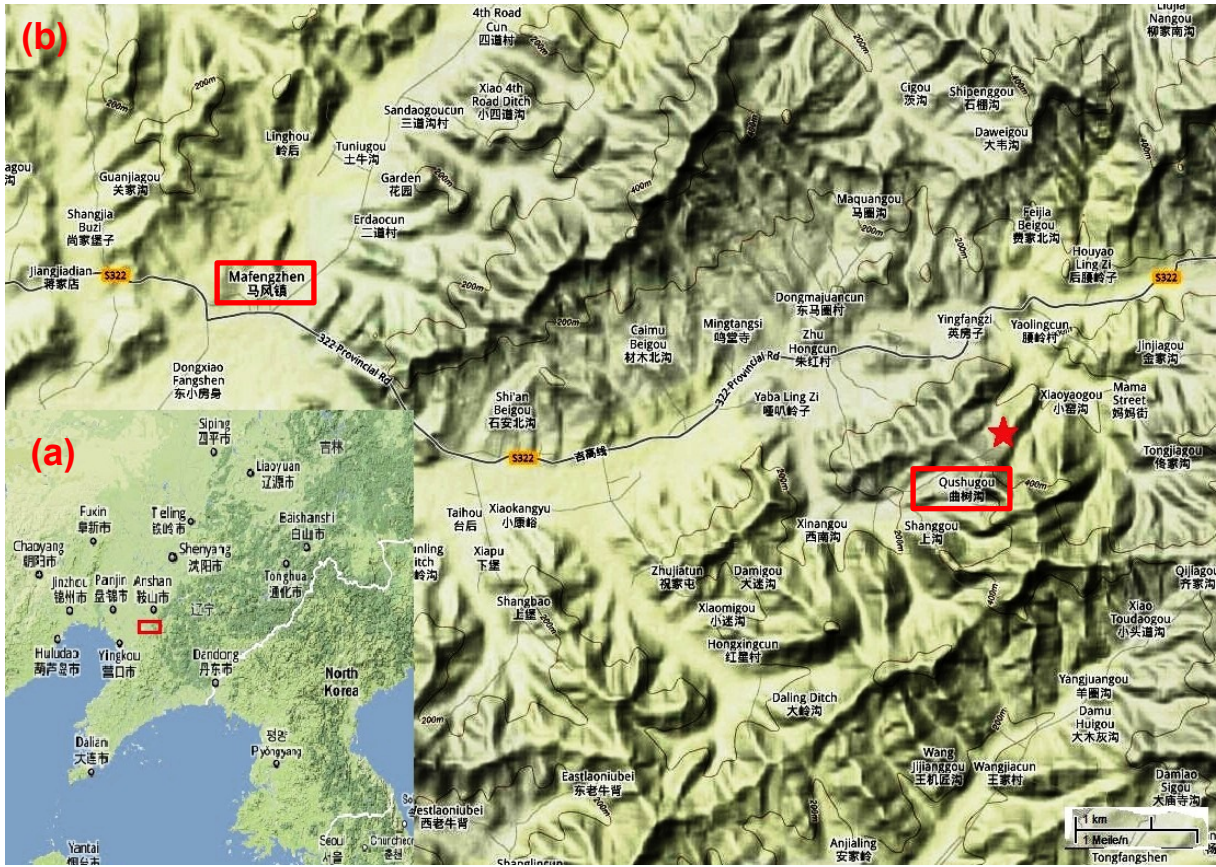


Figure 1: (a) Geographical map of NE China, red box marks the enlarged area (b). (b) Detailed geographic map showing the position of the Aihai open pit magnesite mining operation (red star) and the two villages Qushugou and Mafengzhen (red boxes).

The mining area is dominated by uplands. The highest mountain has an altitude of 559,52 meters above sea-level. Typical for the uplands are the V-shaped valleys and subordinate U-shaped valleys. The river system in the mining area is seasonal. The

water of the catchment area runs off into the Mafengzhen River, which is the on-site preflooder.

The prevailing monsoon climate in NE China is characterized by a warm, rainy summer monsoon and a cold, dry winter monsoon. The average amount of precipitation is 700~800mm, maximum precipitation happens in July-August. The historical average maximum precipitation was 1080mm in the year 1964. The annual average temperature is around 8,4°C. In the summer month (June-August) the average temperature is 29-31°C; in the winter month (December-February) the average temperature is around -16-17°C.

The Aihai magnesite open pit is easy accessible through the provincial road S322 from Haicheng city, the distance amounts 30 kilometers. The next bigger port, Bayuquan port, is around 90 kilometers away from Haicheng and is by the Bohai Sea.

1.1 Geological setting

1.1.1 Overview

The Aihai magnesite deposit is part of the Haicheng-Dashiqiao (Yingke) magnesite ore belt, comprising numerous giant magnesite deposits. The Yingke ore belt is made up of in early Proterozoic metamorphic rock series of Mg-rich carbonate formations in the eastern Liaoning province. The giant magnesite deposits in the Yingke ore belt are stratabound in the upper part of the Dashiqiao Formation of the Liaohe Group (Zhang, 1984). The Liaohe Group represents a lowgrade metamorphic (greenschist - lower amphibolite) volcano-sedimentary facies. The Liaohe Group is embedded in the Jiao-Liao-Ji Belt (Figure 2). The Paleoproterozoic Jiao-Liao-Li Belt (orogen) lies at the eastern margin of the North China Craton (NCC), with its northern segment intervening between the Northern Liaoning-Southern Jilin Complex (Longgang Block), the Southern Liaoning-Nangrim Complex (Nangrim Block) and its southern segment extend across the Bohai Sea into the Eastern Shandong Complex (Li et al., 1995).

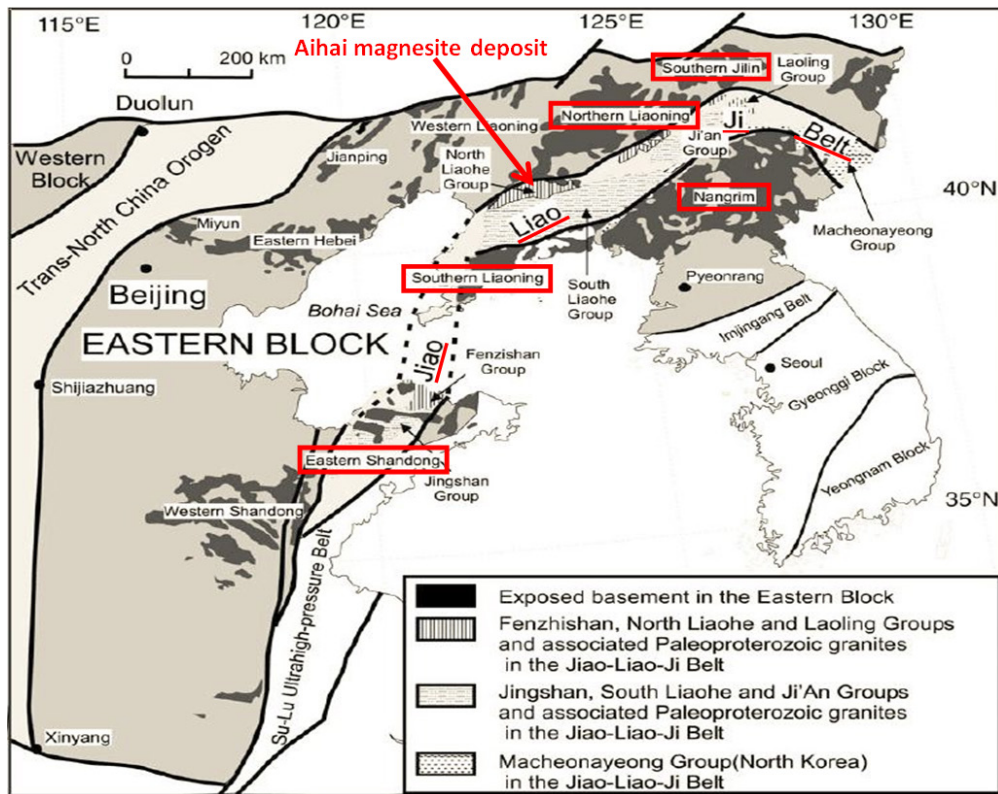


Figure 2: Map of the Paleoproterozoic Jiao-Liao-Ji Belt in the Eastern Block of the North China Craton showing the Northern Liaoning-Southern Jilin Complex, Southern Liaoning-Nangrim Complex and the Eastern Shandong Complex (modified from Zhao et al.,1998)

1.1.2 North China Craton (NCC)

The North China Craton is a general term used for the Chinese part of the Precambrian Sino-Korea Craton. The NCC covers ca. 1,5 million square kilometers. The basement of the NCC consists of variably exposed Archean to Paleoproterozoic rocks, including TTG (Tonalitic-Trondhjemitic-Granodioritic) gneiss, granite, charnockite, migmatite, amphibolite, greenschist, pelitic schist, Al-rich gneiss (khondalite), banded iron formation (BIF), calc-silicate rock and marble (Wu et al., 1991, 1998; Kusky & Li, 2003). The Archean to Paleoproterozoic basement was formed during four different processes, named the Qianxi (> 3,0 Ga), Fuping (3,0-2,5 Ga), Wutai (2,5-2,4 Ga) and Lüliang (2,4-1,8 Ga) event (Huang, 1977; Shen&Quian, 1995). Each of them was closed by a significant tectonic event called Quianxi, Fuping, Wutai and Lüliang movement, were postulated at ca.3,0 Ga, ca. 2,5 Ga, ca. 2,4 Ga and 1,8 Ga, respectively (Huang, 1977; Cheng, 1994).

The tectonic history of the Paleoproterozoic rocks in the interiors of the Eastern and Western Blocks is still poorly known. Herein two current models from Zhao et al. (2001) and from Kusky & Li (2003) are discussed. Zhao et al. (2001) represent the idea of a three-fold tectonic subdivision of the North China Craton (Figure 3). Regarding to this subdivision, the basement of the craton can be divided into two separated Archean to Paleoproterozoic blocks, named the Eastern (EB) and Western Block (WB), segmented by the Trans-North China Orogen (TNCO). In the last decade various information, regarding the lithological, structural, metamorphic and geochronological data were gathered. Based on these data Zhao (2001) suggested that the Trans-North China Orogen represents a Paleoproterozoic collisional orogen between the EB and WB. The Eastern and Western Blocks were amalgamated to form the North China Craton at ca. 1,85 Ga. Li et al. (2000) and Kusky & Li (2003) conform with a similar model for the subdivision of the NCC, but they postulate a different age for the amalgamation. The collisional event is 2,5 Ga (amalgamation). They interpreted the younger event at 1,85 Ga as the Lüliang event, which represents an intercontinental rift stage within the craton.

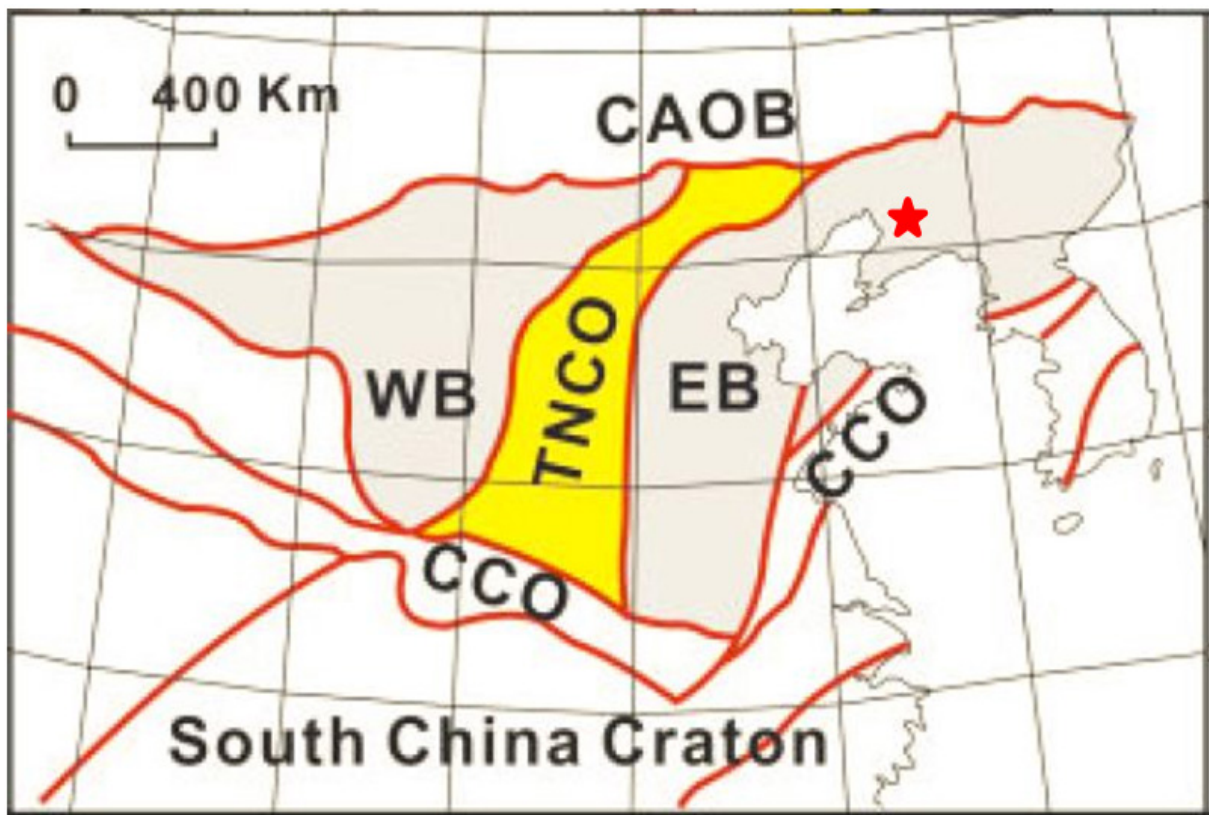


Figure 3: Overview map of the three-fold tectonic subdivision of the NCC showing the southern border of Central Asian Orogenic Belt (CAOB), Central China Orogen (CCO), Trans North China

Orogen (TNCO), Western Block (WB), and Eastern Block (EB). The red star marks the position of the Haicheng-Dashiqiao magnesite ore belt (modified after Li et al., 2011).

1.1.3 Tectonic subdivision and the tectonic belts

The Western Block of the NCC is divided by the Khondalite Belt, which separate the Western Block into the Yinshan Block in the north and the Ordos Block in the south. The Khondalite Belt represents an accretionary belt, formed by the amalgamation of the Ordos and Yinshan Block. The Jiao-Liao-Ji Belt divides the Eastern Block into the Longgang Block in the north and the Nangrim Block in the south (Figure 4). The Jiao-Liao-Ji Belt constitutes the opening and closing of an inter-continental rift zone. Therefore, the Archean to Paleoproterozoic basement of the North China Craton consist of four micro continental blocks (the Yinshan and Ordos blocks forming the Western Block and the Longgang and Nangrim blocks forming the Eastern Block) and three Paleoproterozoic orogenic belts (Khondalite Belt, Jiao-Liao-Ji Belt, and Trans North China Orogen) (Zhao et al., 2010).

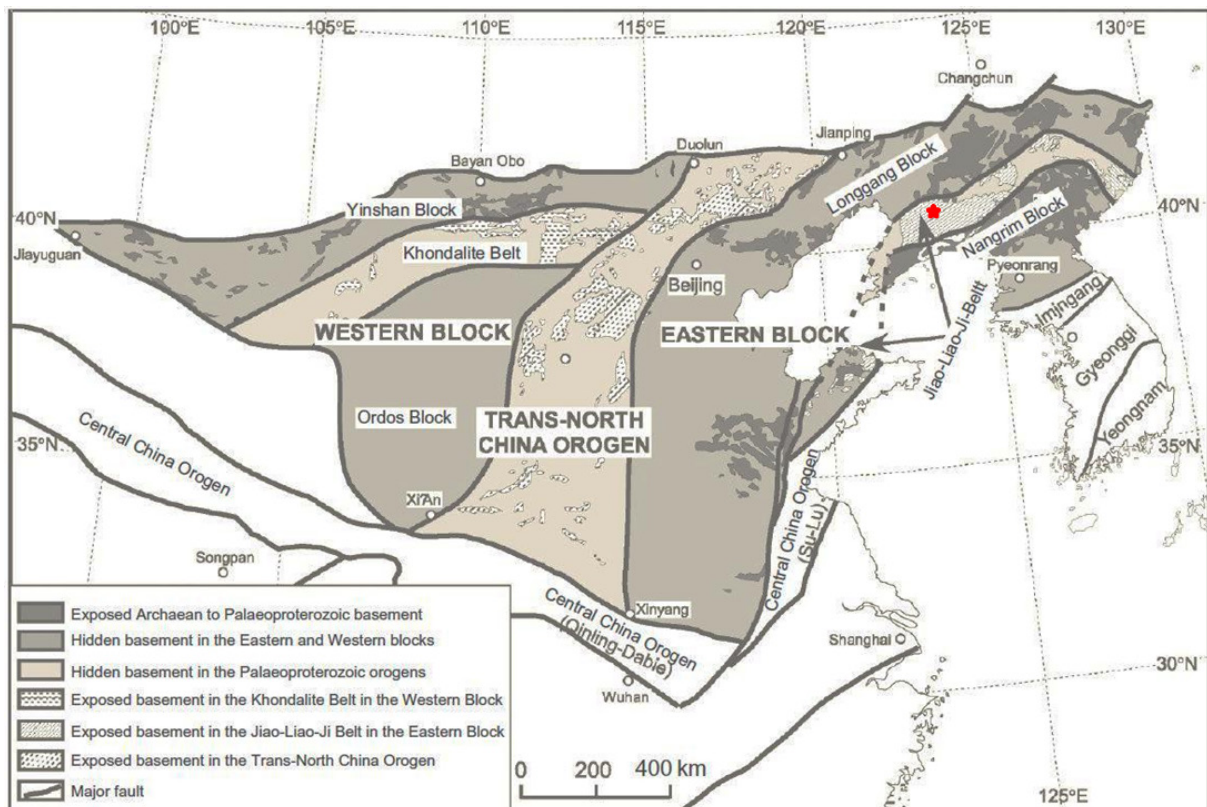


Figure 4: Map of the tectonic subdivision of the Archean to Paleoproterozoic basement of the NCC; the red star shows the position of the Haicheng magnesite district (Zhao et al., 2005).

The Khondalite Belt is a nearly E-W trending belt (Figure 4), which consists predominantly of high-grade graphite-bearing pelitic gneisses/ granulites, garnet quartzites, felsic paragneisses, calc-silicate rocks, and marbles (Condie et al., 1992). The timing of collision between the Yinshan and Ordos blocks along the Khondalite Belt to form the Western Block has not been well constrained until recently. Based on ICP-MS U-Pb zircon dating technique, Yin et al. (2009) obtained metamorphic zircon ages of 1949 ± 12 Ma, 1954 ± 22 Ma and 1941 ± 24 Ma from the pelitic granulites (westernmost part of the Khondalite Belt). This information proposes an amalgamation time of the Ordos Block and the Yinshan Block around 1,95 Ga (Zhao, 2009).

The Jiao-Liao-Ji Belt is a well preserved and vast Paleoproterozoic tectonic belt in the eastern margin of the Eastern Block (Figure 4 and Figure 2), which shows a history of intense deformation, complex stratigraphic relationships and formation of an array of large industrial mineral deposits (Zhang et al., 1988; Jiang et al., 1997; Li & Zhao, 2007).

The Belt consists of greenschist to lower amphibolite facies metamorphic sedimentary and volcanic successions, including the Fengzishan and Jingshan groups in the eastern Shandong, the South and North Liaohe Groups in eastern Liaoning, the Ji'an and Laoling groups in southern Jilin, and possibly the Macheoayeong Group in North Korea. They are transitional from basal clastic-rich sequence and a lower bimodal volcanic sequence, through a middle carbonate-rich sequence, to an upper pelite rich sequence (Li & Zhao, 2007; Li et al., 2005). Voluminous Paleoproterozoic granitoids (Liaoji granitoids) and mafic intrusions are associated with the sedimentary and volcanic rocks in the Jiao-Liao-Ji belt. Available geochronological data show that most of the sedimentary and volcanic successions and pre-tectonic (gneissic) granites in the Jiao-Liao-Ji Belt were formed in the period ca. 2,2-2,0 Ga, metamorphosed and deformed at 1,9 Ga. (Luo et al., 2004; Li et al., 2005; Li & Zhao, 2007). Yin and Nie (1996) obtained a biotite $^{40}\text{Ar}/^{39}\text{Ar}$ age of 1896 ± 7 Ma from the Liaohe Group, interpreted as a metamorphic age. The Jiao-Liao-Ji Belt can be further subdivided into a northern part, which contains the Fenzishan, North Liaohe, and Laoling groups, and southern part that consists of the Jingshan, South Liaohe, and Ji'an groups. This outline is based on stratigraphic correlation

from Zhao et al., 2005. The southern and northern zones are separated by ductile shear zones and faults (Li et al., 2005). The metamorphic evolution of the two belts is characterized by different metamorphic P-T paths: clockwise P-T paths reconstructed for the northern part and anticlockwise P-T paths for the southern part (Lu et al., 1996; He & Ye, 1998) (Figure 5).

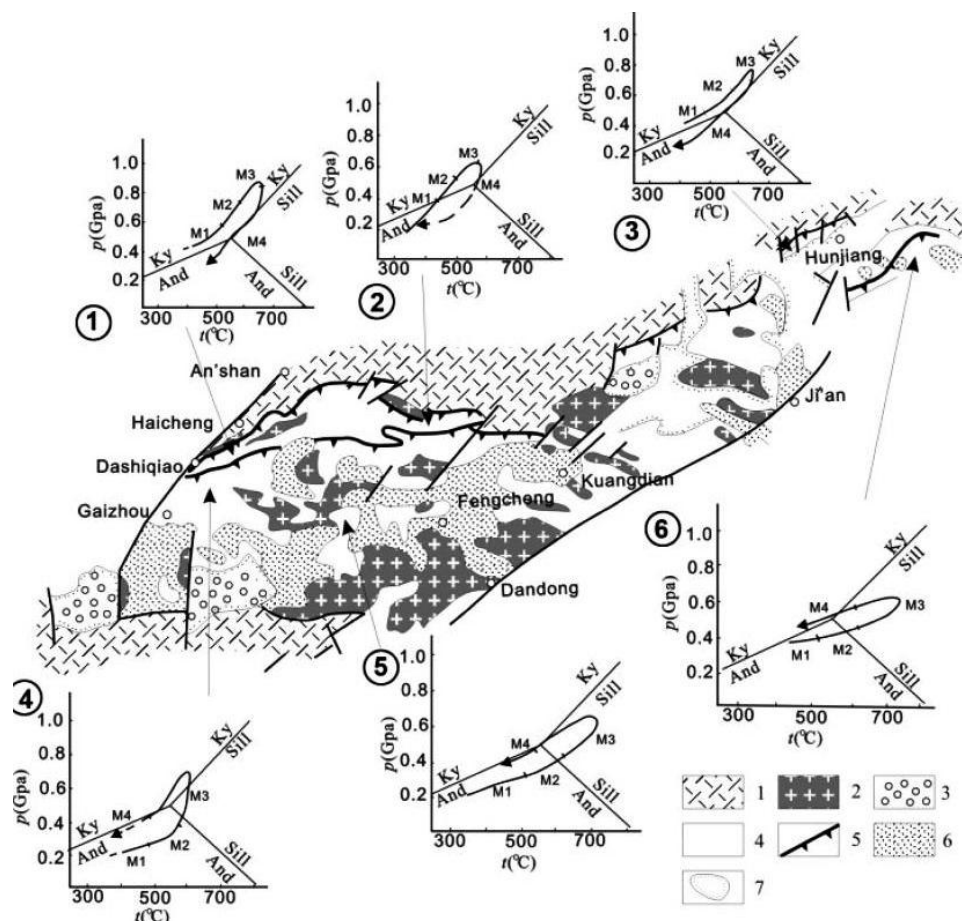


Figure 5: P-T-t paths of the Liaohe Group and its equivalents. ①, ④, after Li et al. (2001); ②, ⑥ after He and Ye (1998); ③, ⑤ modified after Lu et al. (1996). 1—Archaean basement; 2—Palaeoproterozoic granite; 3—Neoproterozoic strata; 4—Liaohe Group and equivalent; 5—major faults; 6—Mesozoic plutons; 7—Mesozoic strata. Ky—Kyanite; And—Andalusite; Sill—Sillimanite.

Controversy has surrounded the tectonic setting and evolution of the Liao-Jiao-Ji Belt. Three tectonic models have been proposed: continental – arc collision (Hu, 1992; Bai, 1993; Faure et al., 2004), continent-continent (terranes) collision (He & Ye, 1998) and a rifting model (Yang et al., 1988; Liu et al., 1997; Li et al., 2001). The rift model suggests that two Archean basement complexes on the north/south sides of the Liaohe Group and the Liaoji granitoids were a single continental block that underwent early Paleoproterozoic rifting and then closed upon itself in the late

Paleoproterozoic (Yang et al., 1988; Liu et al., 1997; Li et al., 2001). One of the major lines of evidence for the rift model include the presence of bimodal volcanics in both the North and the South Liaohe Groups, represented by large amounts of greenschist to amphibolite facies metamorphosed metabasic rocks and minor meta-rhyolites in the Li'eryu Formation (Zhang & Yang, 1988). Another evidence is the existence of the ca. 2,5 Ga TTG basement gneisses and the 2,46 Ga mafic dyke swarms flanking the north and south sides of the Liaohe Group (Zhang & Yang, 1988).

The Trans North China Orogen is a nearly S-N trending zone, ca. 1200 km long and 100-300 km wide (Figure 4). It consists of Neoproterozoic to Paleoproterozoic TTG gneisses, supracrustal rocks (metamorphosed sedimentary and volcanic rocks), mafic dikes, and syn- or post-syntectonic granites. Geochemical data suggest that most of these rocks developed in continental magmatic arc, island –arc, or back arc basin environments (Bai et al., 1992; Wang et al., 2004). Extensive SHRIMP U-Pb zircon and Sm-Nd dating techniques have been applied to determine the timing of metamorphism of the TNCO. In the Chengde Complex (part of the TNCO), for example, Mao et al. (1999) obtained a zircon U-Pb lower intercept age of 1817 ± 17 Ma, interpreted as the time of the high pressure metamorphic event. In the Xuanhua Complex, Guo and Zhai (2001) obtained a garnet Sm–Nd age of 1842 ± 38 Ma and SHRIMP U–Pb metamorphic zircon ages of 1872 ± 16 Ma and 1819 ± 16 Ma from the high-pressure granulites, also interpreted as the age of the high-pressure metamorphic event.

1.1.4 Liaohe Group

The North and South Liaohe Groups, main lithostratigraphic units of the Jiao-Liao-Ji Belt, occur along a long, linear north-east-east trending belt that extends from Haicheng, Dashiqiao and Gaixian in the southwest, through Fengcheng in the central, to Hunjiang in the northeast (Figure 6). The North Liaohe Group is conventionally divided into four formations as shown in Figure 7. The lowermost Langzishan Formation (250 to 1280 m thick), unconformably overlying the late Archean Anshan Complex, is composed of basal conglomerate-bearing quartzites, transitional upwards to chlorite-sericite quartz schists, phyllites, garnet-bearing mica schists and

kyanite-bearing mica schists. The conformably overlying Li'eryu Formation (370 – 800m thick) consists of boron-bearing volcano-sedimentary successions metamorphosed to fine-grained felsic gneiss, amphibolites and mica quartz schist. The Gaojiayu Formation composed of garnet-bearing mica schists, major graphite-bearing mica schists and kyanite mica schists. The Gaojiayu Formation overlaps by the Dashiqiao Formation that consists dominantly of dolomite marbles intercalated with minor carbonaceous schists and mica schists, hosting the largest magnesite deposits in the world (Zhang and Yang, 1988; Liu et al., 1997). The South Liaohe Group also contains four formations: Li'eryu, Gaojiayu, Dashiqiao and the Gaixian Formations, of which the first three formations are comparable in their stratigraphy to the corresponding formations in the North Liaohe Group (Figure 7). The difference between the South and North Liaohe Group is the absence of the Langzishan Formation and the presence of the uppermost Gaixian Formation in the South Liaohe Group.

The Gaixian Formation encloses phyllites, andalusite-cordierite mica schists, staurolite mica schists and sillimanite mica schists, with minor quartzite and marble (Li et al., 2005).

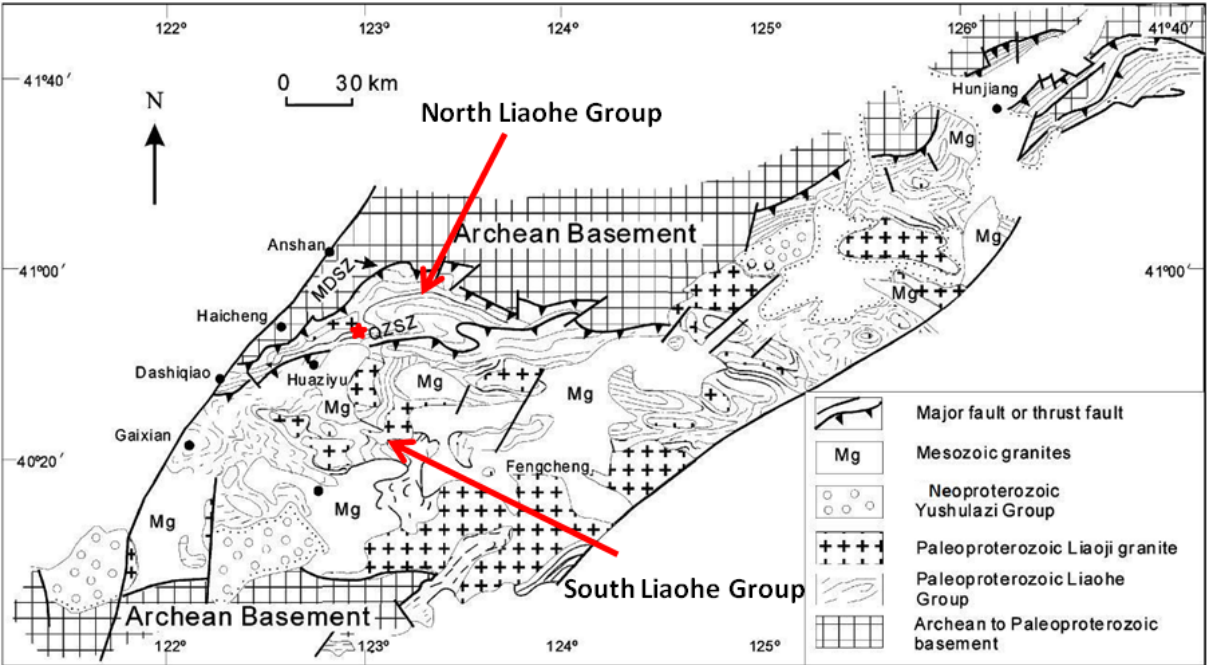


Figure 6: Distribution of the Paleoproterozoic Liaohe assemblage and Liaoji granitoids. MDSZ: major detachment shear zone; QZSZ: Qinglongshan–Zaoerling shear zone (modified after Li et al., 2004).

The younger Yushulazi and Yongning formations cover the Liaohe group, but do not belong to the Liaohe Group. The Yushulazi Formation was deposited at some time between 1,05 Ga and 0,9 Ga, prior to the sedimentation of the 0,9 – 0,8 Ga Yonging Formation. These formations consist of basal conglomerate-bearing quartzites, transitional upwards to quartzites (Luo et al., 2006) (Figure 8). Associated with the Liaohe Group are voluminous Paleoproterozoic granitoid plutons and mafic intrusions. The granitoid plutons, named the Liaoji Granite (Yang & Zhang, 1988), are composed predominantly of A-type-monzogranites with minor rapakivi granites. Figure 7 (Li et al., 1998) shows a simplified profile of vertical stratification of the metamorphic Liaohe Group with parallel ductile shear zones.

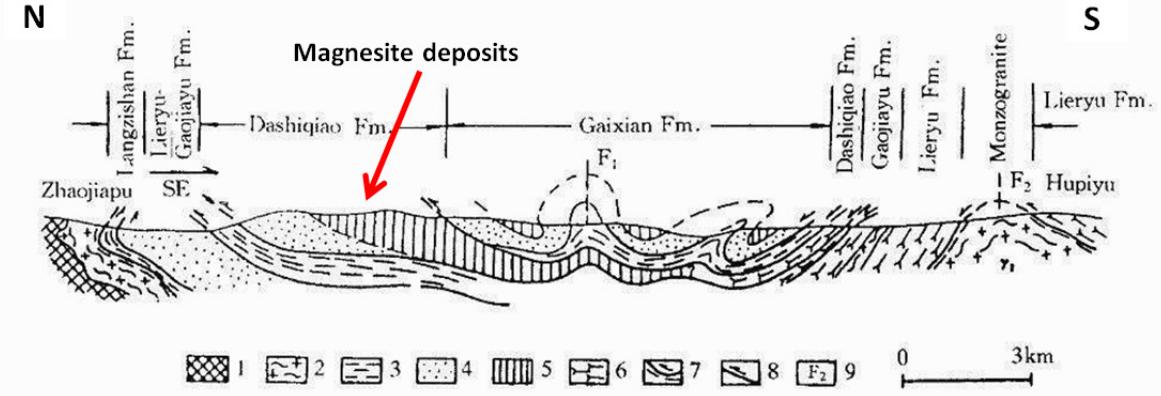


Figure 7: Simplified profile of vertical stratification of the metamorphic Liaohe Group. 1- Archean basement, 2-Paleoproterozoic layered granite, 3-kyanite/staurolite zone, 4-garnet/tremolite zone, 5-biotite chlorite zone(lower-T talc zone), 6-andalusite-cordierite or, 7-main sliding zones,8- bedding-parallel structural plane and sence of ductile sliding (Li et al., 1998).

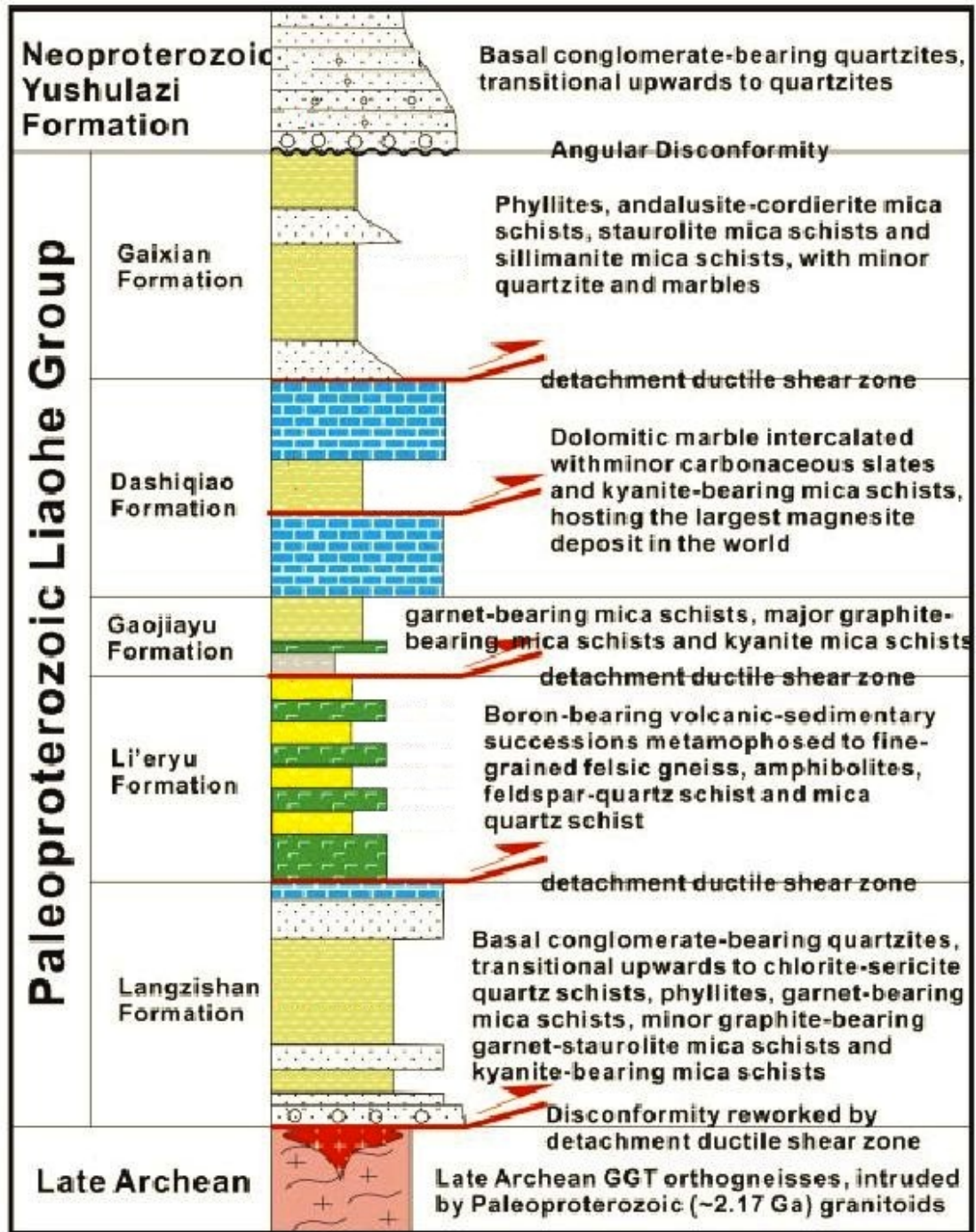


Figure 8: Lithostratigraphic units of the North and South Liaohe Groups (after Luo et al, 2006).

Magnesite Deposits China

Magnesite (magnesium carbonate, MgCO_3) is an important magnesium mineral with a maximum magnesia (MgO) content of 47.8% and of 52.2% CO_2 . It is the world's most important source of magnesia. Magnesite (MgCO_3) is a rare rock forming mineral occurring in different marine and non-marine geological settings due to the geochemical relations of silicon, iron and calcium. In carbonate terrains, magnesite is rock-forming and is the main mineralic constituent of largely monomineralic masses.

Magnesite is an essential raw material for basic refractories: after heating and sintering, the product known as "caustic magnesite" (700-1000°C) and "dead burned magnesite" (1600-1800°C). The latter one has the composition MgO (periclase). The major part of magnesium metal is at present only produced from seawater and brines.

World magnesite resources are estimated over 12 billion tonnes and are primarily located in China, DPR Korea, Russia, Slovakia, India, etc. (Figure 9). Over 92% of magnesite resources are sedimentary-hosted sparry type (Veitsch type), and around 8 % are of the cryptocrystalline type (Kraubath type & Bela Stena type). The magnesite resources in China are dominated by sparry magnesite.

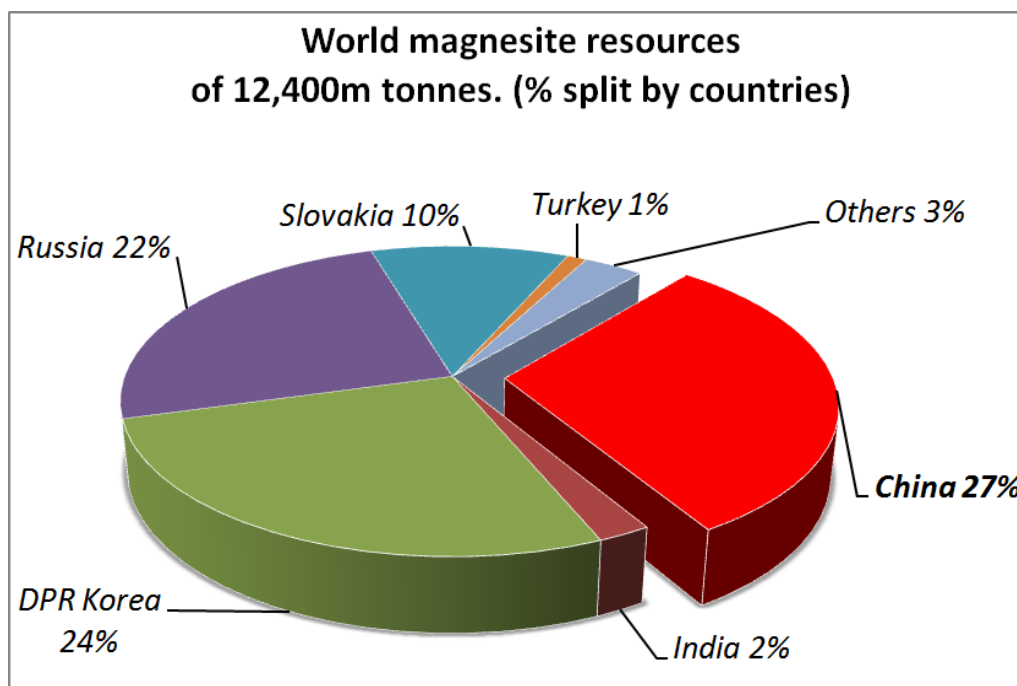


Figure 9: World magnesite resource distribution (modified after Wilson & Ebner, 2005).

The worldwide magnesite production was around 17,4m. tonnes in the year 2005, compared to the year 2009 it was 24,4m. tonnes of magnesite (Figure 10). The worldwide mining production of magnesite increased between 2005 and 2009 over 39,9%. About 86% of the magnesite mined is sparry type and 14% is cryptocrystalline (Wilson & Ebner, 2005).

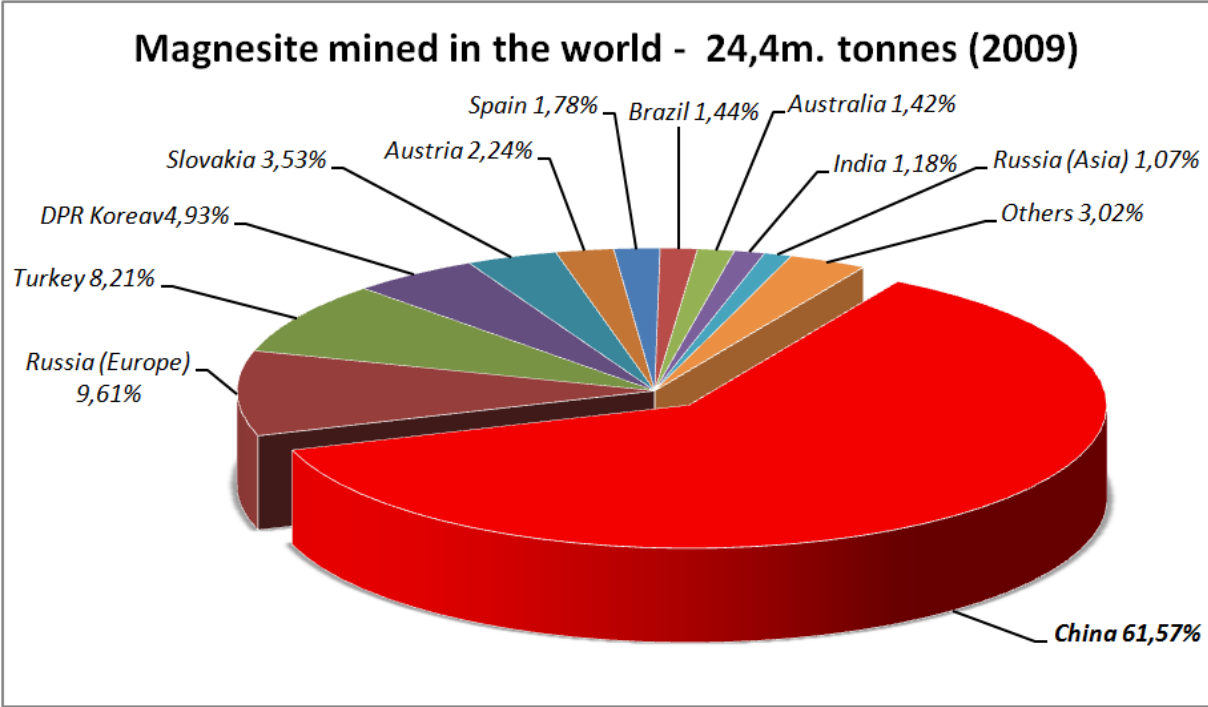


Figure 10: Magnesite mined in the world (2009) (Weber et al. 2011)

The diagram in Figure 11 represents the annual magnesite mining production from China, in a time range from 2003 up to 2009. In the period from 2006-2007 the magnesite production rose sharply (doubling of production). After the year 2007 the mining production stayed at the same with variations +/- 1 million tonne.

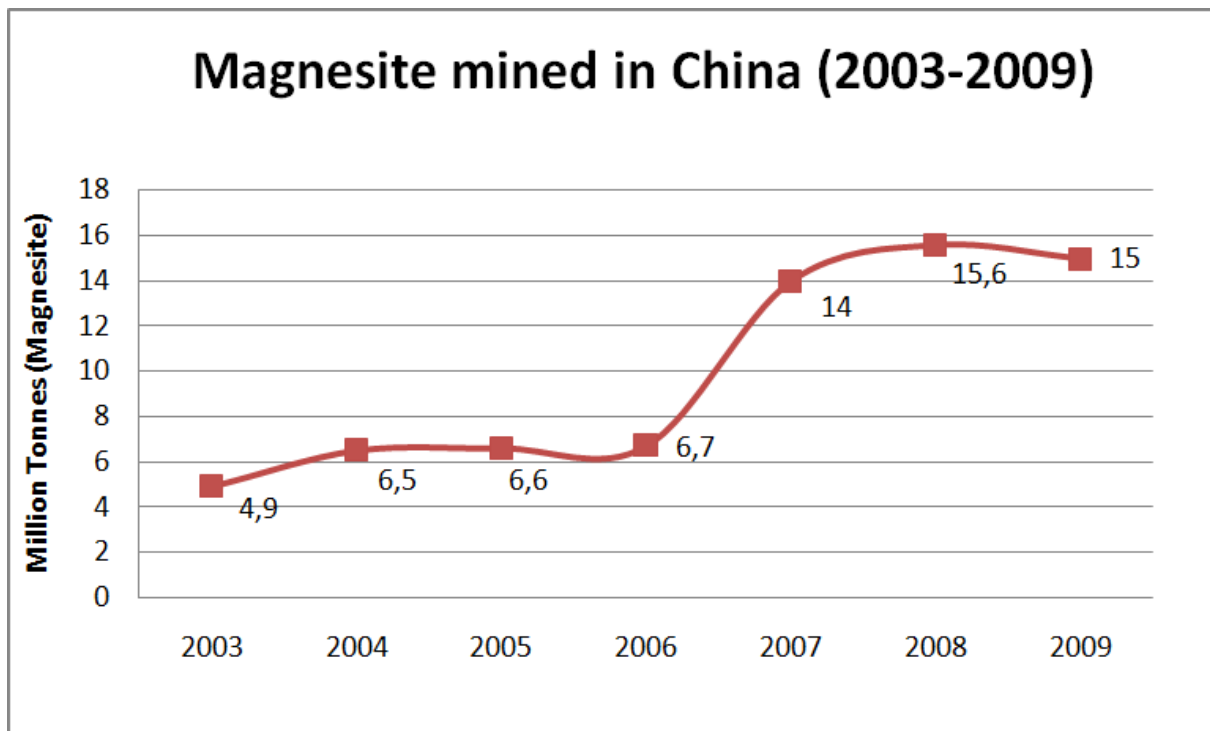


Figure 11: The diagram shows the annual magnesite production between 2003 and 2009 (Weber et al. 2011).

Apart from one producer in Shandong province, central eastern China, the country's magnesite resources and production are concentrated around the cities of Haicheng and Dashiqiao in Liaoning province, north-east China. The Haicheng-Dashiqiao Magnesite Belt (Yingke ore belt) hosts the majority of producers. In total these may number 200-300 of large, medium, and many small scale producers (Figure 12). However, the provincial government is attempting to streamline the suppliers into fewer, more cost efficient enterprises, and evolve and diversify their product base.

Most of the large producers supply domestic and overseas markets, and also operate integrated refractory brick and monolithic plants, also for domestic and export markets.

Leading Chinese magnesite producers include Xiyang Group, Jiachen Group, Liaoning Houying Group, Haicheng Huayin Group, Haicheng Huayu Group, and Liaoning Jinding Magnesite Group.

While China’s magnesite industry will remain an important and active sector of China’s industrial minerals business, it will increasingly be focused on supplying domestic markets and SE Asia market.

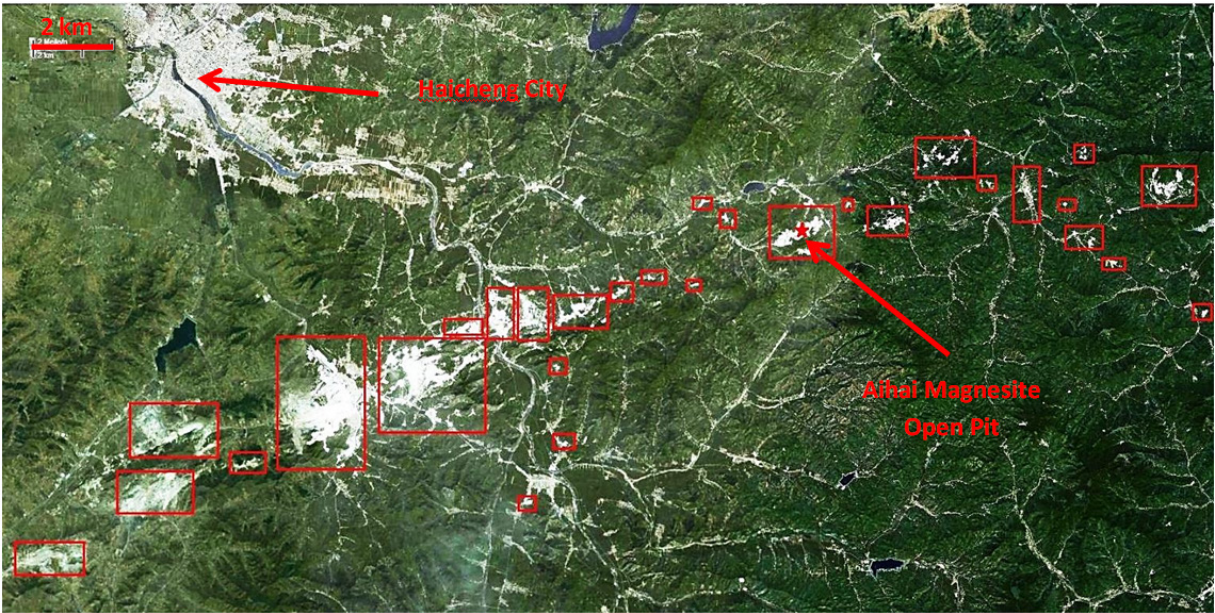


Figure 12: Aerial image of the Yingke ore belt (Dashiqiao-Haicheng Magnesite District). Red boxes mark areas with great numbers of magnesite (talca) producers and the investigation area.

Regarding magnesite exports, there have been at least five consecutive varieties of an exporters’ syndicate since 2000. Each version had commendable purposes, but after a few months to a year the syndicates broke up over disagreements on prices and procedures or simply because of indifferences. The associations for magnesite exports have universally targeted to boost the price of exported grades.

During 2008 a considerable part from the Chinese magnesite product was bootlegged. The smuggling course supposedly runs via the South Korean port of Kunsan en route to Rotterdam. This illegal “source” has seemingly been prevented by Chinese government authorities, but not without consequences.

It is believed that the smuggling drastic measures alone has been the biggest impact on bottleneck and prices of late and is estimated to have taken about 700,000 tonnes per year out of the market. This has increased prices significantly and has had a major influence on demand for export licenses (as well as driving speculation that smuggling may soon resume) (O’Discroll, 2008).

1.2 Genetic Models

Magnesite has a similar crystal structure than calcite and dolomite, hence its inclusion into the calcite mineral group. The differentiation between the magnesite crystal structure and the calcite structure is that the magnesite crystal structure has a slightly smaller cell due to the smaller size of the magnesium ion. The difference between the ionic diameters of Mg^{2+} and Fe^{2+} ($Mg^{2+}=0.65 \text{ \AA}$, $Fe^{2+}=0.79 \text{ \AA}$), is not as great as that between Ca^{2+} (0.99 \AA) and Mg^{2+} , Fe and Mg substitute for each other and form the isomorphous series from magnesite through breunnerite (5 - 30% $FeCO_3$) to siderite ($FeCO_3$), and from dolomite to $CaCO_3 \cdot FeCO_3$ (Figure 13).

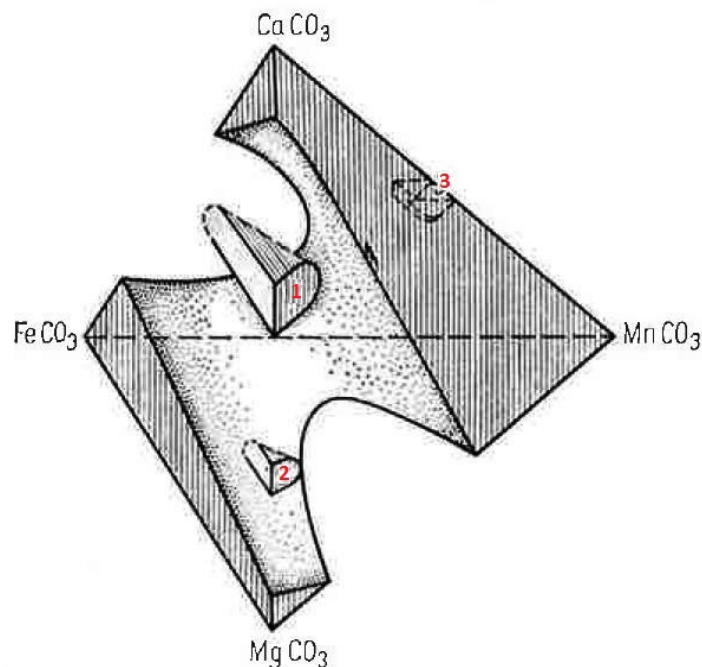


Figure 13: Tetrahedral solid solution field of the trigonal calcite- and dolomite series. 1 Dolomite, 2 Huntite, 3 Kutnahorit (Godovikov, 1975).

The mineralogical characteristics and physical properties of Magnesite are described by Wilson & Ebner (2005):

- Color is white or grey, also tinted yellow or brown.
- Lustre is vitreous.
- Transparency crystals are translucent to transparent only in individual crystals.
- Crystal system is trigonal.

- Crystal Habits are usually massive forms such as lamellar, fibrous and coarse to fine grained rocks. Crystals are extremely rare, but when found they are in the form of rhombohedral or hexagonal prisms
- Cleavage is perfect in three directions forming rhombohedrons.
- Fracture is conchoidal to uneven
- Hardness is 4-4,5.
- Specific gravity is approximately 3,0 (average).
- Streak is white.
- Associated Minerals are calcite, dolomite, aragonite, strontianite and serpentine.
- Other characteristics: effervesces easily only in hot dilute hydrochloric acid.
- Best field indicators are crystal habit, reaction to acid, occurrence and cleavage.

Magnesite occurs in various geological environments, but as ore it forms three main types of deposits (Wilson & Ebner, 2005).

1. Sparry (crystalline) magnesite hosted in carbonate rocks: Veitsch Type
2. Cryptocrystalline magnesite hosted in ultramafic rocks: Kraubath Type
3. Cryptocrystalline precipitations in young clastic freshwater sediments: Bela Stena type

They differ in the form/grade of crystallization, specific rock assemblages, geological environments and mineralization process. They are named according to their type deposits, from where they have been described and introduced to the geological literature for the first time.

The occurring magnesite deposits in the Liaoning province (Haicheng-Dashiqiao magnesite district) appertain to the Veitsch-Type. The sparry magnesite deposits of the Veitsch Type are hosted and controlled by Precambrian to Carboniferous carbonate-rocks, mainly dolomitic. These carbonates represent marine, shallow sea water environments. On the basis of field discoveries and geochemical parameters a

metasomatic genetic model is predated. It is expected that the source of the Mg-rich fluids are marine evaporates, formation waters, evaporated brines and/or metamorphic hydrothermal fluids (Pohl, 1992).

The shape of the deposit forms layers and lens and irregular stocks of monomineralic magnesite ore. Often the layered texture and the magnesite-dolomite boundaries are angular to the sedimentary bedding that mostly can hardly be distinguished. In the metasomatic transition zones dolomitic interlocking are common. In some cases the magnesite is associated with pelite, sandstone, conglomerate and basic volcanics and mostly occurs in low medium grade metamorphic terrains.

In metamorphic terrains the genesis of sparry magnesite is pre-metamorphic. During a metamorphic event a recrystallization proceeds, this recrystallization has a minimal influence on the character of the magnesite, due to the monomineralic composition. But it is entirely possible that silicate mineral phases can be formed; e.g. talc. The occurring talc has many various manifestations and dimensions- veins, lenticular lumps and even massive bodies, which are exploitable. The talc appearance is caused by the reaction between SiO_2 -rich hydrothermal fluids and the magnesite/dolomite or through metamorphic mineral reaction. The above mentioned process bred reduction in quality; another quality decreasing process is the redolomitization of the magnesite, through descending surface waters (Wilson & Ebner, 2005).

1.3 Geological frame and the genetic models for the giant magnesite deposits in the Haicheng-Dashiqiao district

The giant magnesite deposits occur in the Dashiqiao Formation in the eastern Liaoning province, NE China. The early Proterozoic Dashiqiao Formation forms Mg-rich carbonate and argillite rock sequences. The Haicheng-Dashiqiao ore belt (magnesite district) is strictly controlled by the third section of the Dashiqiao Formation (Figure 14). The Dashiqiao formation can be subdivided into three sections. In the first section magnesite ore bodies are missing, this section is dominated by calcite and dolomite marbles. The second section represents micaschists; and the third one is mainly composed of magnesite, magnesian- and

dolomitic marbles with phyllite thin layers in the top (Jiang et al., 2004). Talc deposits are always associated with the magnesite deposits, but frequently associated with fault zones. These talc deposits are of metasomatic origin. The talc and magnesite ore bodies are surrounded by dolomitic and magnesitic marbles.

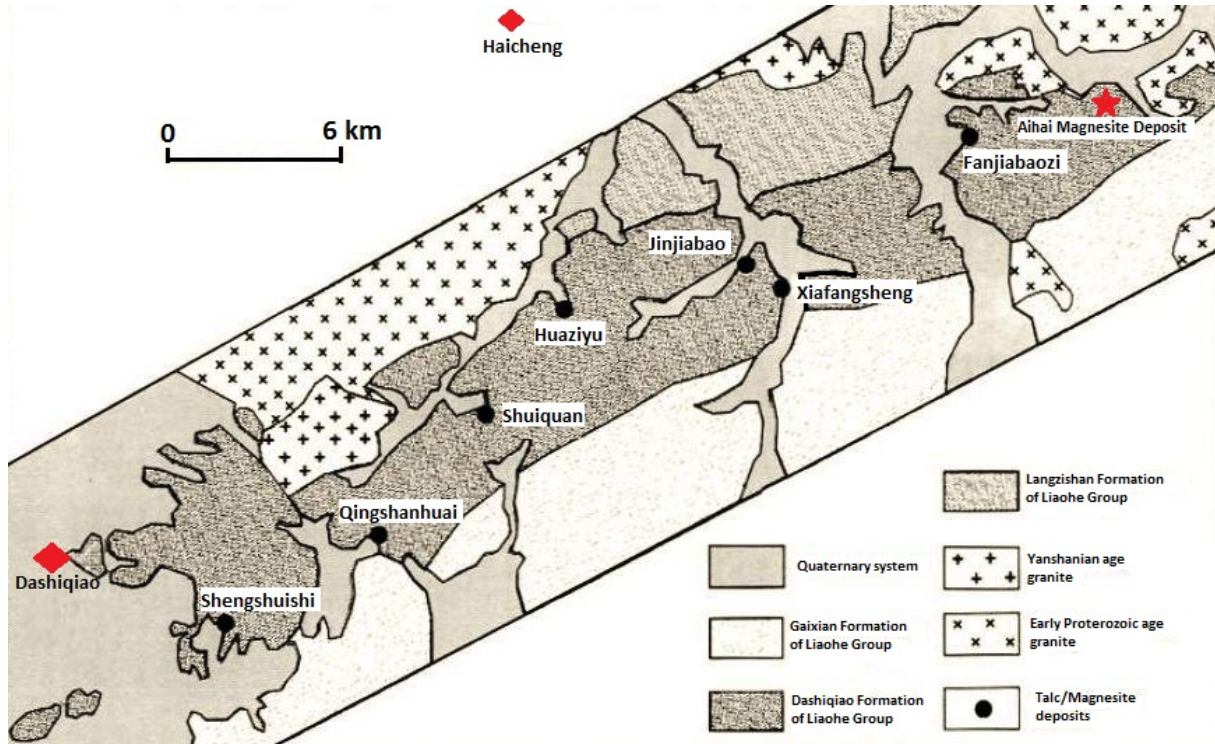


Figure 14: Simplified geological map of the Haicheng-Dashiqiao (Yingke) magnesite ore belt (modified after Jiang et al., 2004).

The magnesite ore bodies are distributed in a large area, over 100 km extension and 4 km wide in the eastern Liaoning province. The ore bodies show mostly NE trending and they are concordant with the host rocks. The shape of the ore bodies are bed like and in the lateral extension they are transforming to dolomitic marble. Another characteristic is that the ore beds are interbedded with metamorphosed sedimentary rocks.

The typical composition of the magnesite deposits in the eastern Liaoning province after Jiang et al., 2004 (ascending order):

- Main magnesite ore body; subdivided in three ore beds.
 - Lower bed with striped dolomitic marble and phyllite (> 350m).
 - Middle part of thick magnesite ore bed with interbedded dolomitic marble (> 2000m).

- Upper magnesite ore bed with interbedded siliceous dolomite and some phyllite containing fossils of algae (> 400m).
- Thinly bedded dolomitic marble and sericite phyllite.

The Proterozoic development of Mg-rich carbonates controls the thickness and scale of the magnesite deposits. The thickness of the magnesite deposits are dependent from the thickness of the third section of the Dashiqiao Formation- the thicker the third section, the thicker the Mg-rich carbonates and magnesite deposits. It shall be deemed as a rough guide. According to the regional survey data the Dashiqiao Formation can vary greatly in thickness. For example the average strata thickness of the north flank of the Yingluo-Caohekou-Taipingsao synclinorium is 1700m and the maximum is 3570m. In the area of Shengshuishi, Qingshanhuai, Huaziyu and Xiafangshen the strata thickness achieve the local maximum. In this thickest layer is the highest density of giant magnesite deposits.

The typical ore minerals of these deposits include magnesite. The crystalline magnesite varies in colour from white, white-pink, white-yellow, white-grey and grey. The mineral grain size also shows a variation from fine grained (<0,5cm), medium grained (0,5-1,0cm), to coarse grained (1,0-5,0cm). In special parts of the deposits the grain size reach up to 10-15cm, but these are exceptions. Associated mineral phases are talc, tremolite, diopside, scapolite, pyrite, graphite, etc. In many magnesite deposits lamprophyre dyke swarms intruded into the magnesite ore beds, but show no influence on the quality of the magnesite ore. Geochemical analyses indicate that these lamprophyre dykes were intruded in late Jurassic (155 +/- 4 Ma) and show some geochemical characteristic of potassic magmas (Jiang et al., 2005). In the Aihai magnesite deposit there exists around 4 lamprophyre dikes, which are all NEE-trending with individual dike being 0,3-1,5m wide (Figure 15). In the Huaziyu magnesite deposit are existing more than 30 lamprophyre dikes.

In the last two decades the meta-sedimentary textures in the magnesite layers were well-investigated. The occurring textures such as palimpsest stratification, oblique bedding, landslip, ripple marks and hail marks were described by Feng et al. (1995).

In addition Chen et al. (2003) discovered during field work a 40-50cm thick lens-shaped gypsum bed. The bed is interlaying in grey yellow-green mudstone in the Daling magnesite mine near Dashiqiao. There are 2-5cm wide white fibrous gypsum ores contained in gypsum rocks. The chemical signature from the sulphur of the gypsum is indicating a marine facies sedimentary evaporate origin.

The two main controlling factors for the magnesite mineralisation are the lithology and the palaeo-geographic position. Palaeomagnetism investigation established the theory that the Dashiqiao Formation was located in a dry tropical or subtropical environment (17-28, north latitude) (Dong et al., 1996).

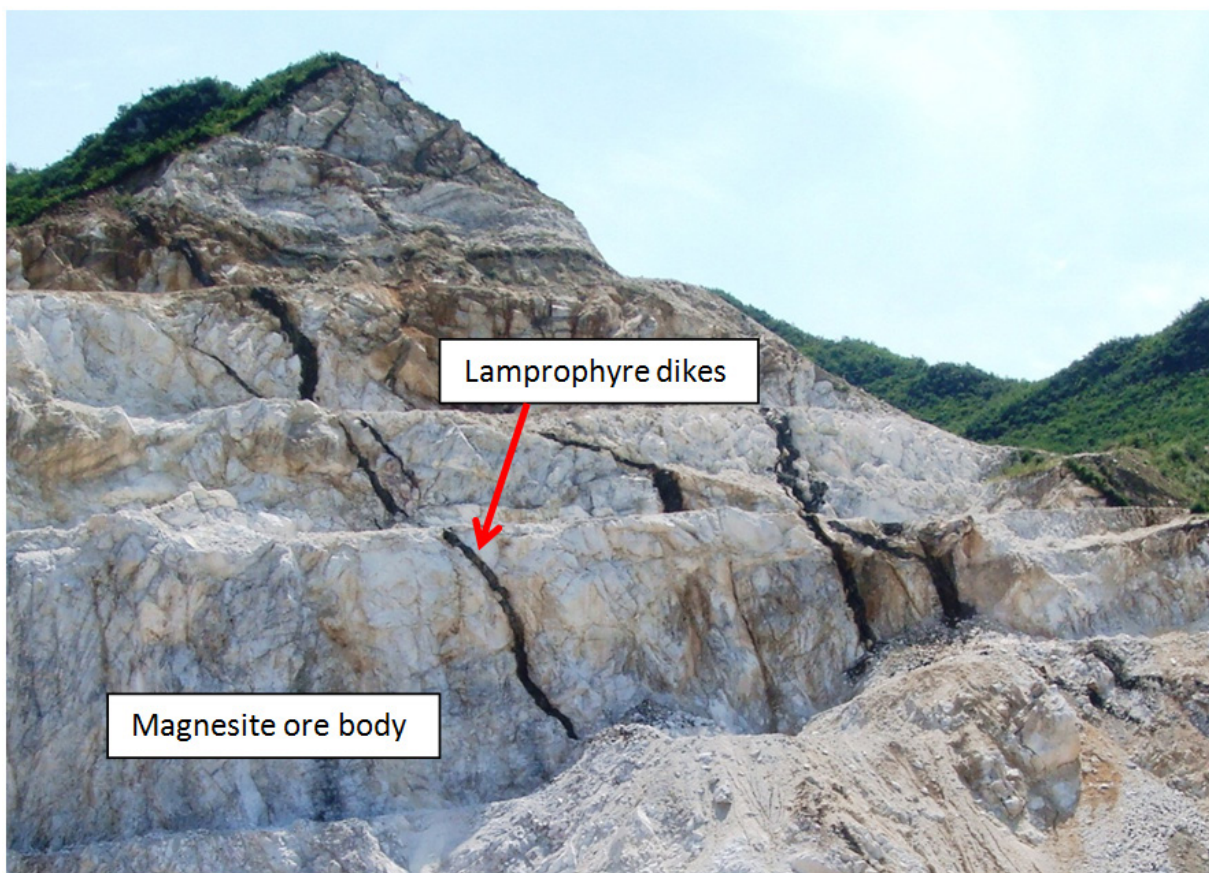


Figure 15: Lamprophyre dikes in the Aihai magnesite open pit.

Dong et al. (1996) describe the sedimentary facies change in the Dashiqiao ore bearing formation from north to south; littoral clastic facies → restricted platform facies → coastal beach bar facies → semi-restricted platform facies → open platform facies. The restricted platform facies was below the low-tide level and formed a sedimentary environment which may represent lagoons on continental margins

(Figure 16). Through the low palaeo latitude of the lagoons the prevailing climate was dry and hot. The evaporation rate from the seawater was high in the lagoons and the salinity increased gradually. In the Early Proterozoic the CO_2 ($> \text{CO}_3^{2-}$) content was rather high in the air and the lagoon waters presented a high $\text{Mg}^{2+}/\text{Ca}^{2+}$ ratio (Tu, 1996). In view of the evaporate cycle dolomite was deposited first in the lagoons, due to the first evaporation step the $\text{Mg}^{2+}/\text{Ca}^{2+}$ ratio increased rapidly. When the Mg^{2+} content is abundant enough in the lagoon water and there is enough CO_3^{2-} in the lagoons, magnesite is precipitated. The presence of large amount of stromatolites in the Dashiqiao Formation magnesite beds suggests that organisms participated in magnesite deposition (Zhang, 1988). It is debatable if this biogenic precipitation/sedimentary process alone is responsible for the formation of the super large magnesite deposits.

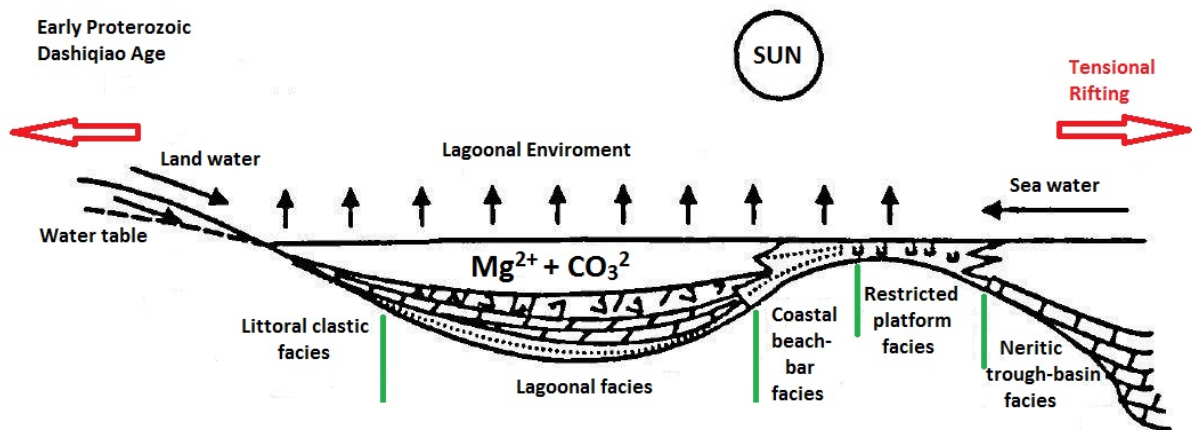


Figure 16: Model of the sedimentary environment from the Haicheng-Dashiqiao ore district (modified after Chen & Cai, 2000).

During the biogenic precipitation/sedimentary process some minerals recrystallized and hydrous minerals dehydrated in the dolomite and magnesite layers. Through the thickening of the overlying layers also the geothermal gradient increased.

In contrast to the above mentioned precipitation theory, the increase of the geothermal gradient suggests a hydrothermal metasomatic process for the formation of the huge magnesite deposits. The responsible fluids came from synsedimentary or diagenetic brines, which migrated from a brine pool down into the seafloor. The Mg-rich fluids transformed the carbonate host rocks by hydrothermal replacement into

magnesite ore bodies. This theory expounded the limited distribution of the magnesite bodies in the third section of the Dashiqiao Formation, because the second section, composed of mica schists, functioned as a geochemical barrier to avoid brine waters penetrate through it.

The tensional Liaoning rifting ended with the Lüliang (Lüliang orogeny) movement. The eastern Liaoning rift closed and the Liaohe Group was folded and metamorphosed (Figure 17).The ore-bearing formation underwent reworking of regional greenschist-facies to amphibolite-facies metamorphism (Peng & Xu, 1994; Peng & Palmer, 1995).

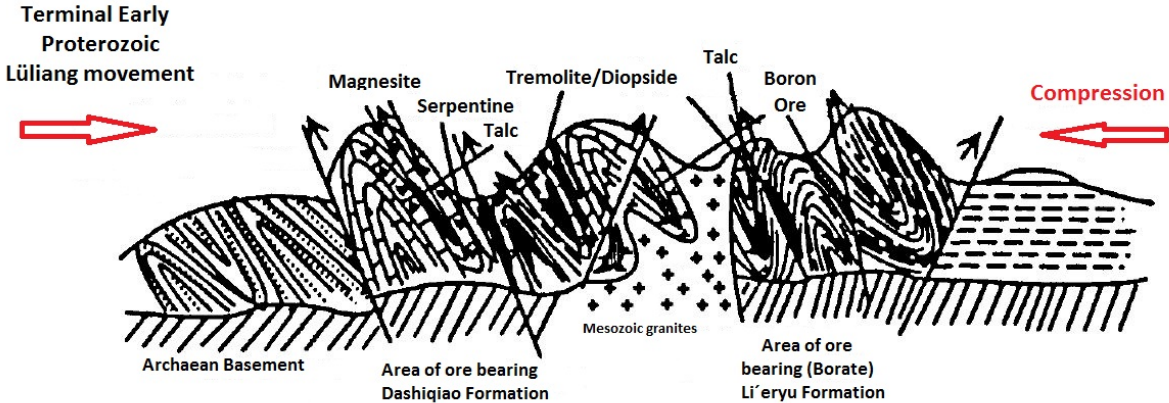


Figure 17: Model of the compression of the Liaohe Group, caused by the Lüliang movement (modified after Chen & Cai, 2000).

The eastern Liaoning palaeorift can be divided in three tectonic facies, what several tectonic and geochemical studies show. According to their rock assemblages and mineral deposits associations the three tectonic facies are: north slope zone, inner depression zone and south shallow zone. The magnesite and talc minerogenic area (Haicheng-Dashiqiao district) lies in the north slope zone (Chen & Wang, 1994; Liu et al., 1997; Chen & Cai, 1998; Chen, 2000) (Figure 18).

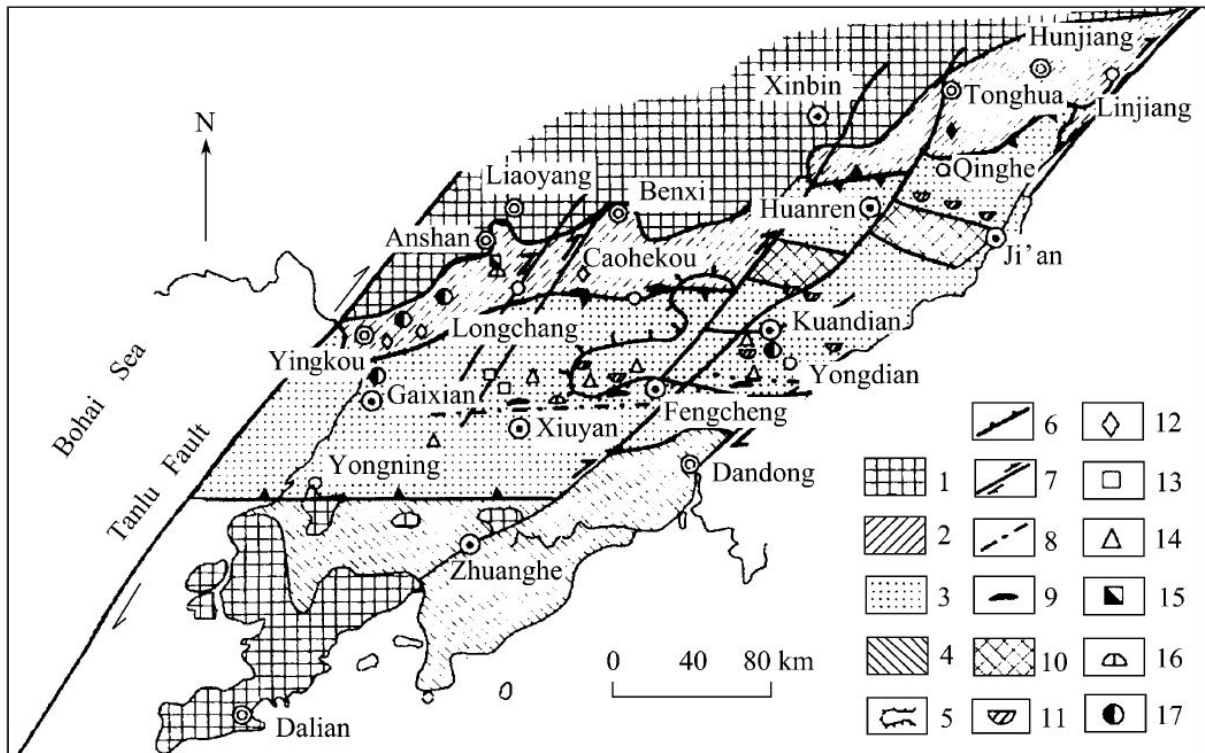


Figure 18: Geological map showing the tectonic subdivision for the early Proterozoic rift system and magnesite/talc deposits (modified from Chen & Wang, 1994). 1: Archean craton; rift areas (2-4); 2: north slope zone; 3: inner depression zone; 4: shallow zone; 5: mantle uplift; 6: boundary (deep fault) of tectonic zones; 7: shear fault; 8: extension fault; 9: basic rock; 10: interred uplift; mineral deposits (11-17); 11: boron; 12: talc; 13: serpenite (Xiuyan jade); 14: brucite; 15: diopside and tremolite; 16: clinoclhorite; 17: fibrous sepiolite

The sedimentary magnesite and dolomite experienced a second enrichment once more during regional metamorphism. The dolomite and the magnesite were transformed into dolomitic marble and coarse grained magnesite. In the metamorphic epoch late in the early Proterozoic also minerogenic fluids were mobilized, which came from buried seawater and brines. The minerogenic fluids metasomatized the Mg-rich carbonates to form some new pure magnesite bodies and veins were formed during this stage (Chen et al., 2002). The metasomatic process also increased the SiO₂ content of the fluid, because the SiO₂ was taken up from the surrounding rocks. In special tectonic positions the SiO₂-rich metamorphic fluids metasomatized the Mg-rich carbonates to form the world famous talc deposits of the Haicheng-Dashiqiao ore belt.

Although the metamorphic epoch is not the main stage for magnesite mineralization, it is the main stage of the talc mineralization.

Figure 19 gives an overview of the different mineralization stages in the Dashiqiao Formation of the Liaohe Group. The non-metallic deposits (magnesite, talc, boron etc.) were the result of combination and superimposition of sedimentary/diagenetic mineralization and metamorphic mineralization in the Early Proterozoic and later the non-metallic deposits were affected by magmatic intrusions (Chen & Cai, 2000; Tang et al., 2009).

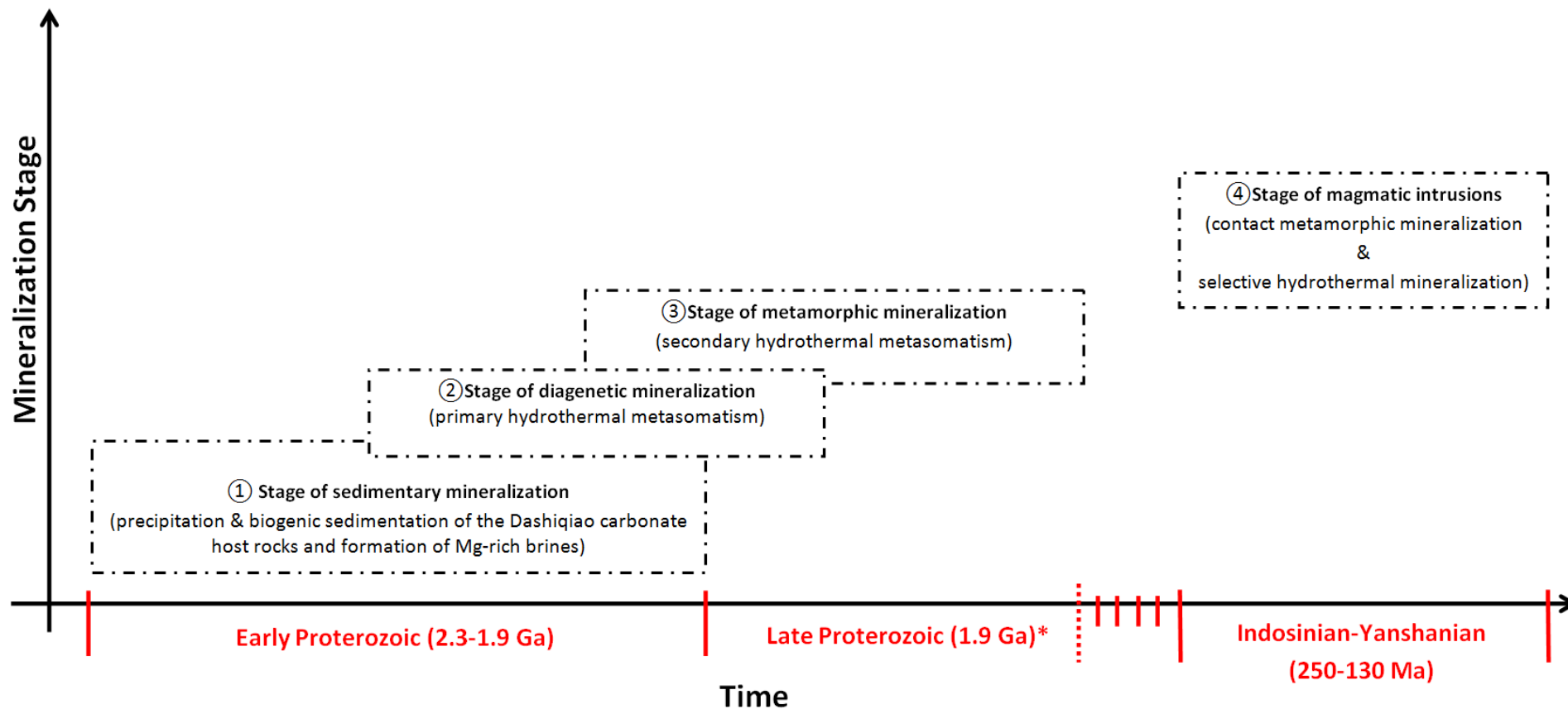


Figure 19: Minerogenic system of the magnesite deposits in the Dashiqiao Formation. * The peak of the metamorphic event is 1.9 Ga. Associated mineral phases from the different stages: 1) calcite, dolomite, magnesite; 2) magnesite, dolomite; 3) talc (genesis of the talc deposits), magnesite, dolomite, serpentine, diopside, tremolite, clinoclhorite; 4) fibrous sepiolite.

Petrography and texture of host rocks, magnesite ore and late mineralizations

In field observations, petrographical and geochemical investigations the following succession of rock/mineral formations were recognized (Figure 20):

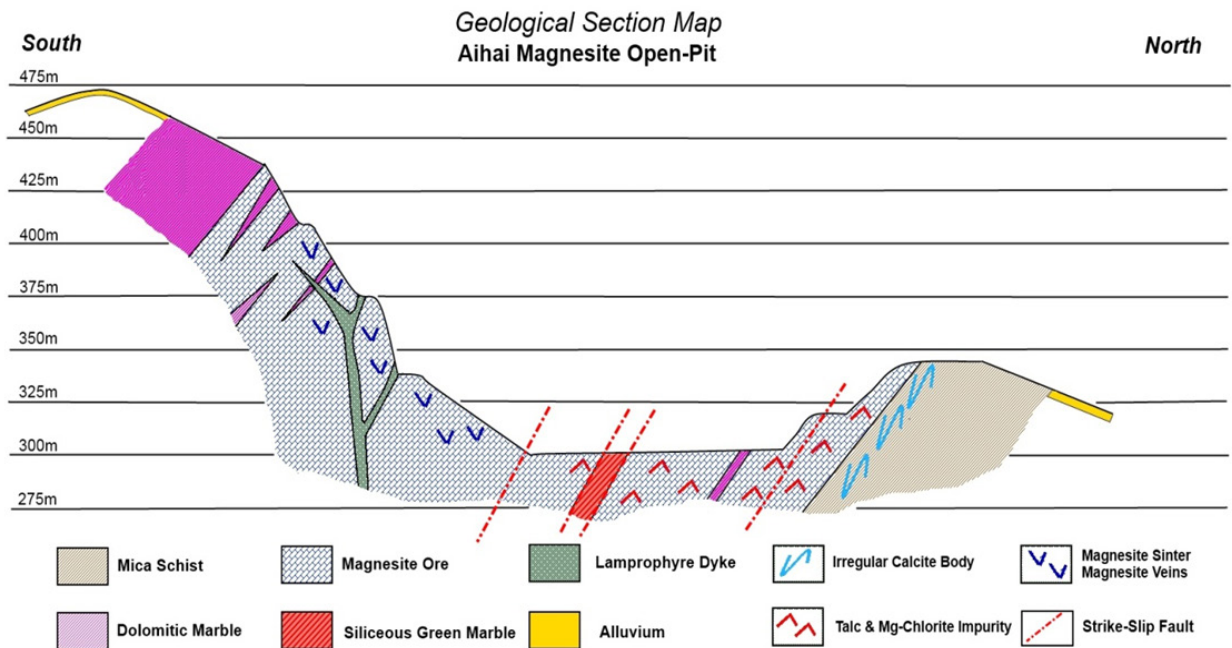


Figure 20: Geological cross section of the Aihai Magnesite open pit.

Host rocks (ascending order)

- fine grained, brown micaschist (foot wall)
- thinly banded dolomitic marble (hanging wall)
- siliceous green banded calcite marble
- high-Mg potassic lamprophyre dikes

Magnesite ore body

- white fine-grained magnesite
- grey fine-grained magnesite
- dark medium-grained magnesite, containing talc and Mg-chlorite
- dark grey/white mottled magnesite

- magnesite sinter veins

Late non-carbonate mineralization

- talc bound to tectonized zones
- fibrous sepiolite on slickenside surfaces

1.4 Micaschist

The brown micaschist represents the footwall of the magnesite deposit. The contact between the magnesite and the mica schist is sharply developed. The foliation of the mica is concordant to the layer boundary. The layer boundary between magnesite and micaschist is of sedimentary origin. After magnesite formation this boundary was overprinted by tectonic movements (Figure 21).

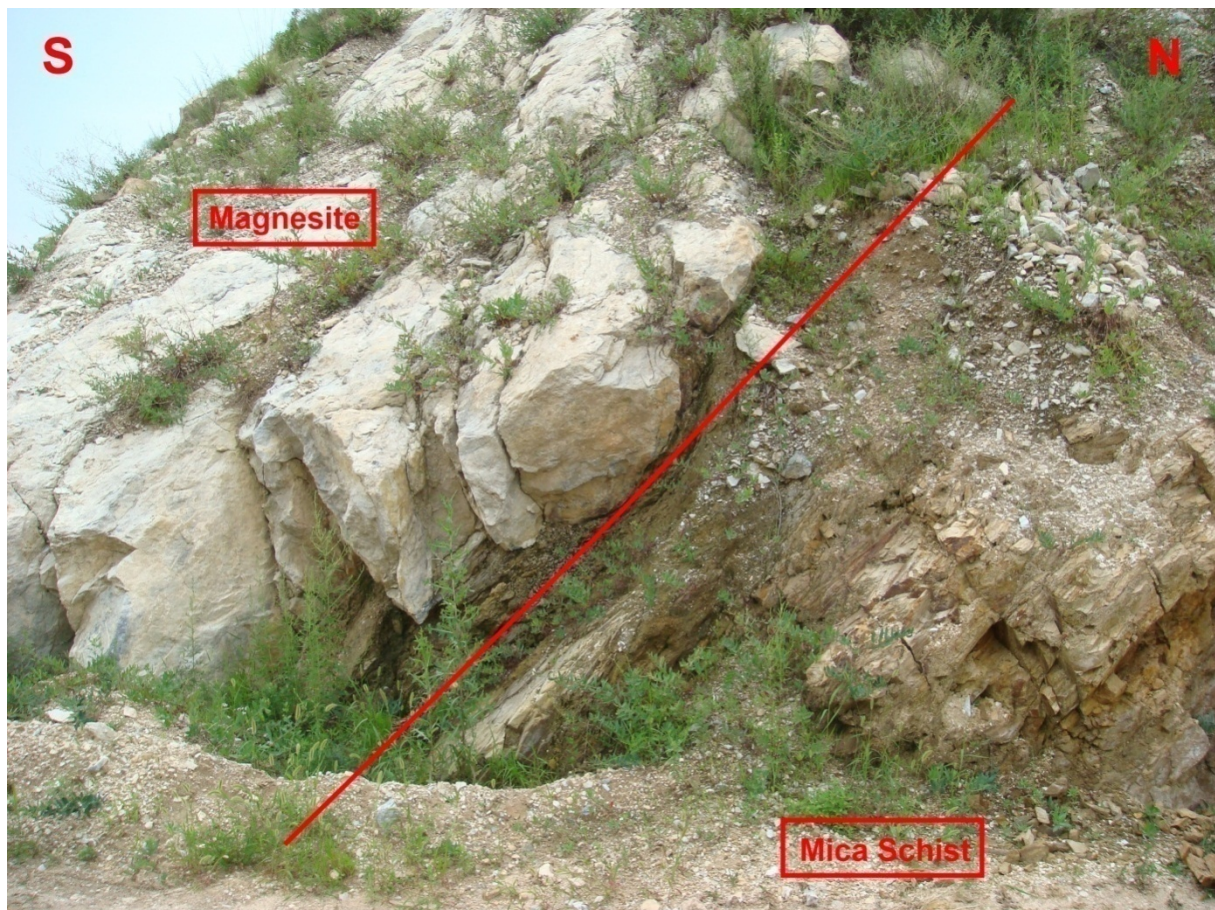


Figure 21: Tectonized border between micaschist and magnesite ore layers.

The outcrops of micaschist are generally heavily weathered and show a dark brown characteristic color. Near to the contact zone the micaschist shows an irregular

network of calcite veins. In areas with high calcite vein density also small calcite bodies are terminated (Figure 22). The shape and the dimension of the bodies are irregular; the bodies' diameter is 30 cm at maximum. In contrast to the micaschist the calcite veins show sharp contours and edges.



Figure 22: Calcite veins and small bodies in the micaschist.

The polished specimen (Figure 23a) shows a typical rusty brown color and slightly folded schistosity. The micaschist has a high porosity due to weathering process. The second polished specimen (Figure 23b) illustrates the different generations of calcite veins in the micaschist. The older calcite vein generation is grey and mainly parallel to the schistosity. The younger calcite generation crosscutting the schistosity is white.

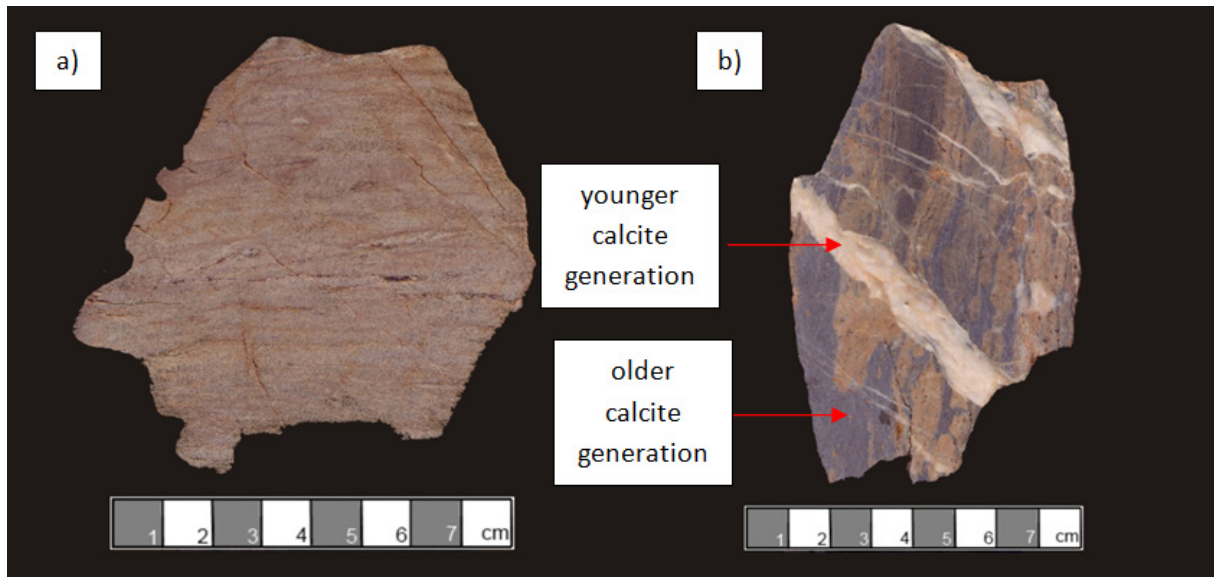


Figure 23: (a) typical rusty brown micaschist; (b) micaschist with calcite veins.

Under the microscope the micaschist displays thin alternating bands composed of muscovite, biotite and quartz. The mica scales have their cleavages and their flat sides parallel; the quartz occurs in rounded, elliptical or irregularly shaped grains. A minimal amount of limonite causes the rusty brown color (Figure 24).

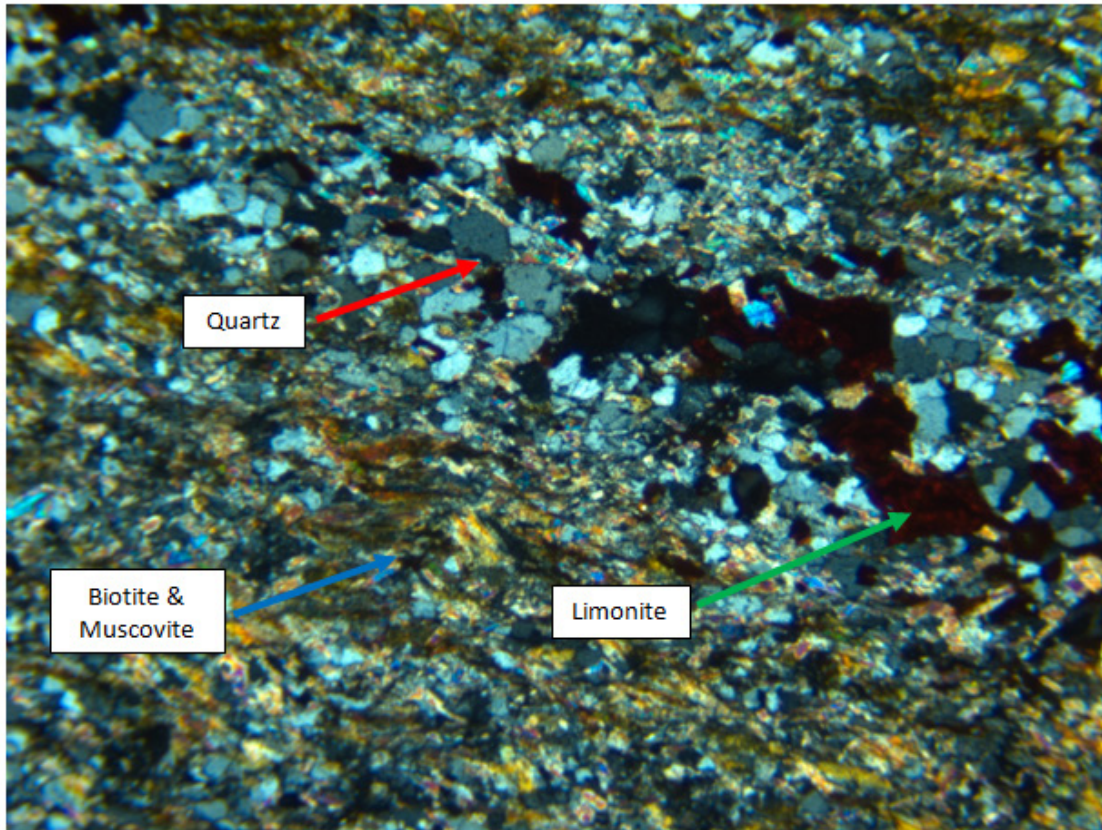


Figure 24: Microscope image of the micaschist (image length 2,85 mm).

The photomicrograph from the micaschist with calcite veins shows the same similar mineral assemblage like the ordinary micaschist (Figure 25). The only distinction is the presence of calcite and leucoxene. The younger calcite generation is characterized by rhombahedral twinning and coarse crystals. The older calcite generation is the intercrystalline matrix between quartz and mica.

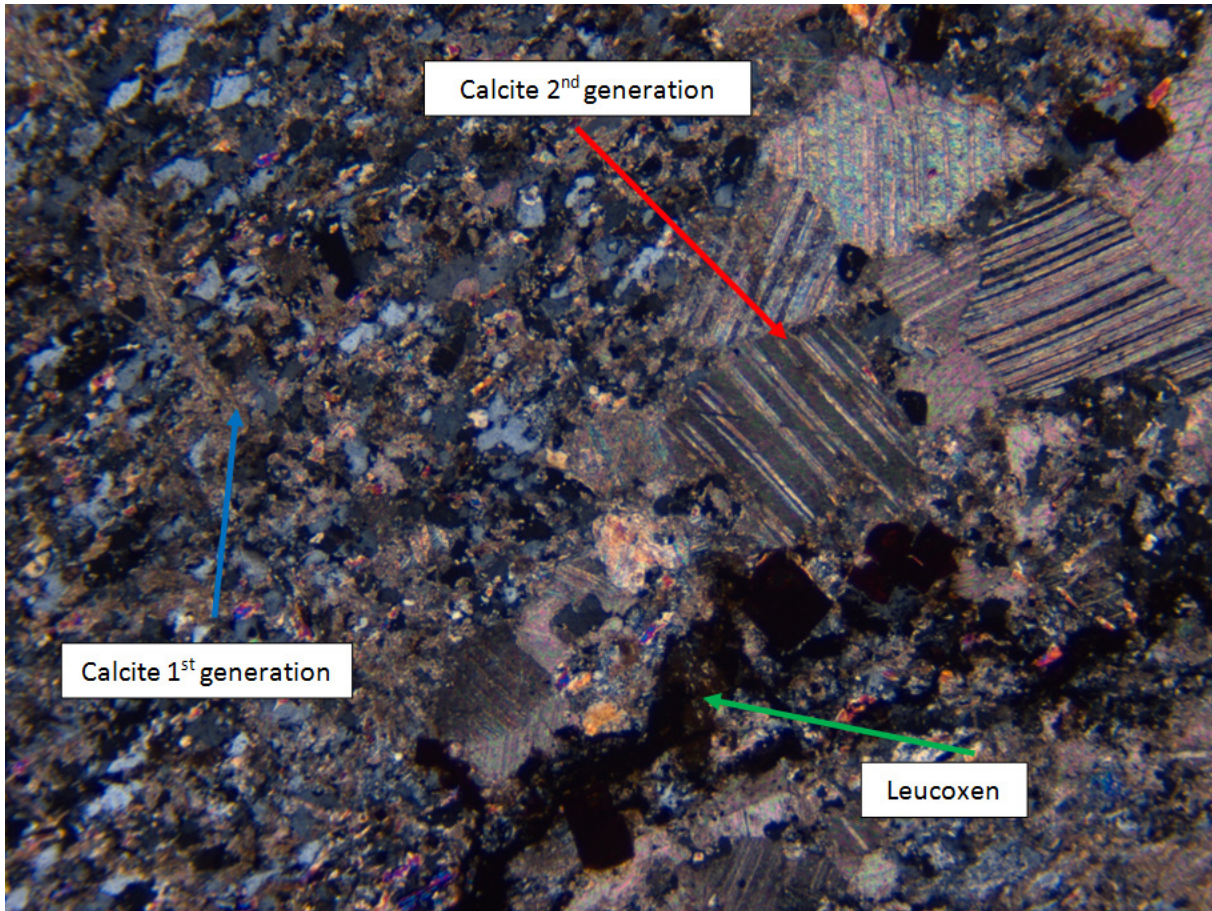


Figure 25: Micaschist with calcite veins (image length 2,85 mm).

1.5 Thinly banded dolomite marble

The magnesite ore body is concordantly alternating with thinly bedded dolomite marble host rocks. The thickness of the dolomite marbles varies between 0,5m – 2,0m (Figure 26). The dolomite marbles display a metasomatic transition zone to the magnesite ore. In certain cases the transition zone is slightly tectonized parallel to dolomite layers. The banding is caused by light and dark layers alternating in centimeter-rhythms. The banding is wavy and shows sometimes clayey intercalations (Figure 27).



Figure 26: Folded banded dolomite marble outcrop.

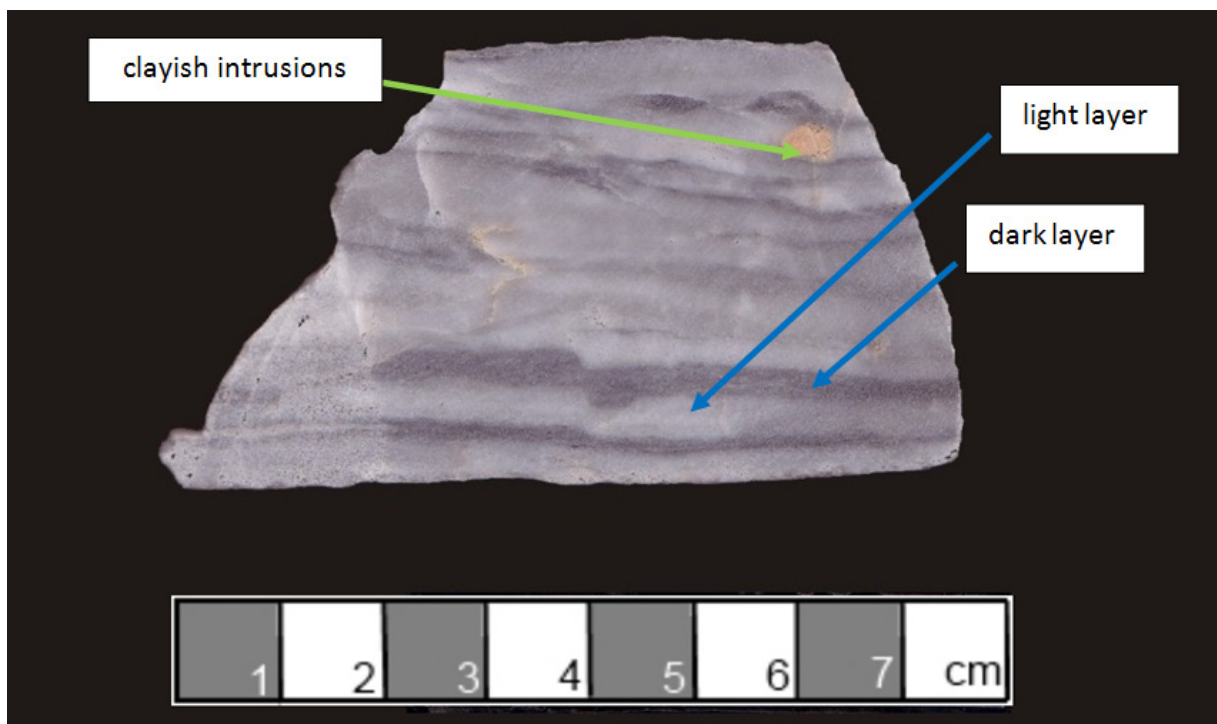


Figure 27: Thinly banded dolomite marble, with clayey intercalations.

The thin-section photomicrograph of the thinly banded dolomite shows two generations of coarse- and medium-sized dolomite crystals with a xenotopic texture (Figure 28). Xenotopic texture is defined here as a mosaic of anhedral crystals with irregular or curved intercrystalline boundaries and, usually undulatory extinction. The dark and light layers of the banded dolomite are marked by difference in crystal size, occurrence of mica and the dark coloration is caused by a graphite matrix. Some of the grains are charged with micro inclusions that give the crystals a dusty look.

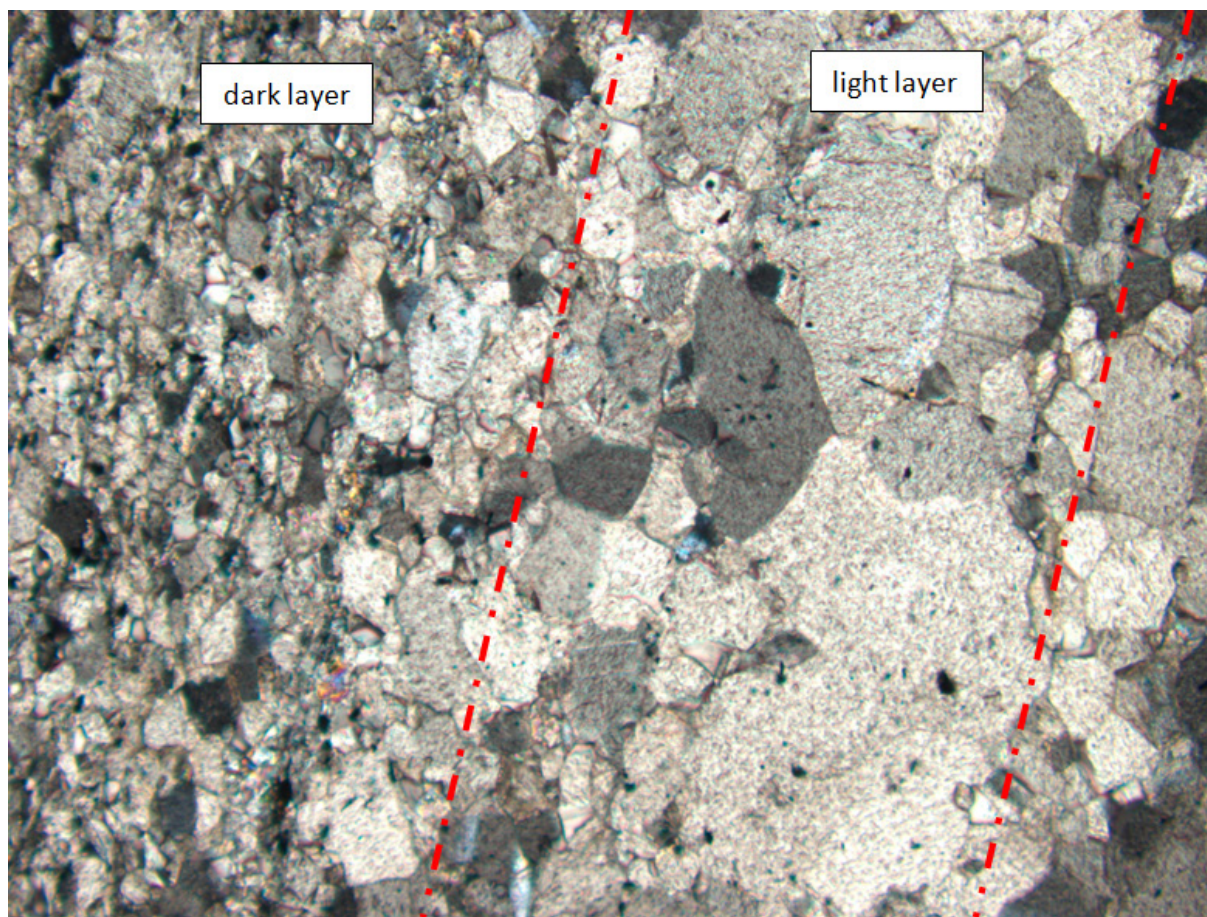


Figure 28: Photomicrograph of banded dolomite (image length 1,77 mm).

1.6 Siliceous green banded calcite marble

In the middle part of the open pit, the magnesite ore body is interbedded with siliceous green banded marble. The thickness of the siliceous green marble varies between 7 to 10 m and is concordant to the magnesite layers. The layer boundary between magnesite and siliceous green marble is of sedimentary origin. The banding is characterized by the variation of mint green, light and gray layers. The thickness of

the different layers diversifies from centimeter to decimeter ranges. Between the layers several pyrite accumulations were observed. In the transition zone to the magnesite ore, the banded marble shows a streaky-wavy structure (Figure 29).



Figure 29: Siliceous green banded marble, with streaky-wavy structure in the lower part of the image.

The polished specimen of the banded marble underlines the alternating mint green (tremolite), light and gray layers, which reflects a concentration of quartz and finely disseminated pyrite (Figure 30).



Figure 30: Banded marble with alternating light and gray layers.

The thin-section image show calcite that forms a compact seriate texture, its crystal size can reach about 0,5-1 mm. The irregularly shaped grains are strongly interlocking along their boundaries. Accessory minerals include tremolite. Twinning and well developed cleavage are very common features of the calcite crystals (Figure 31). Figure 32 displays the transition between the light and gray layers. The gray layer is characterized by a fine matrix, which consists of quartz, calcite and pyrite.

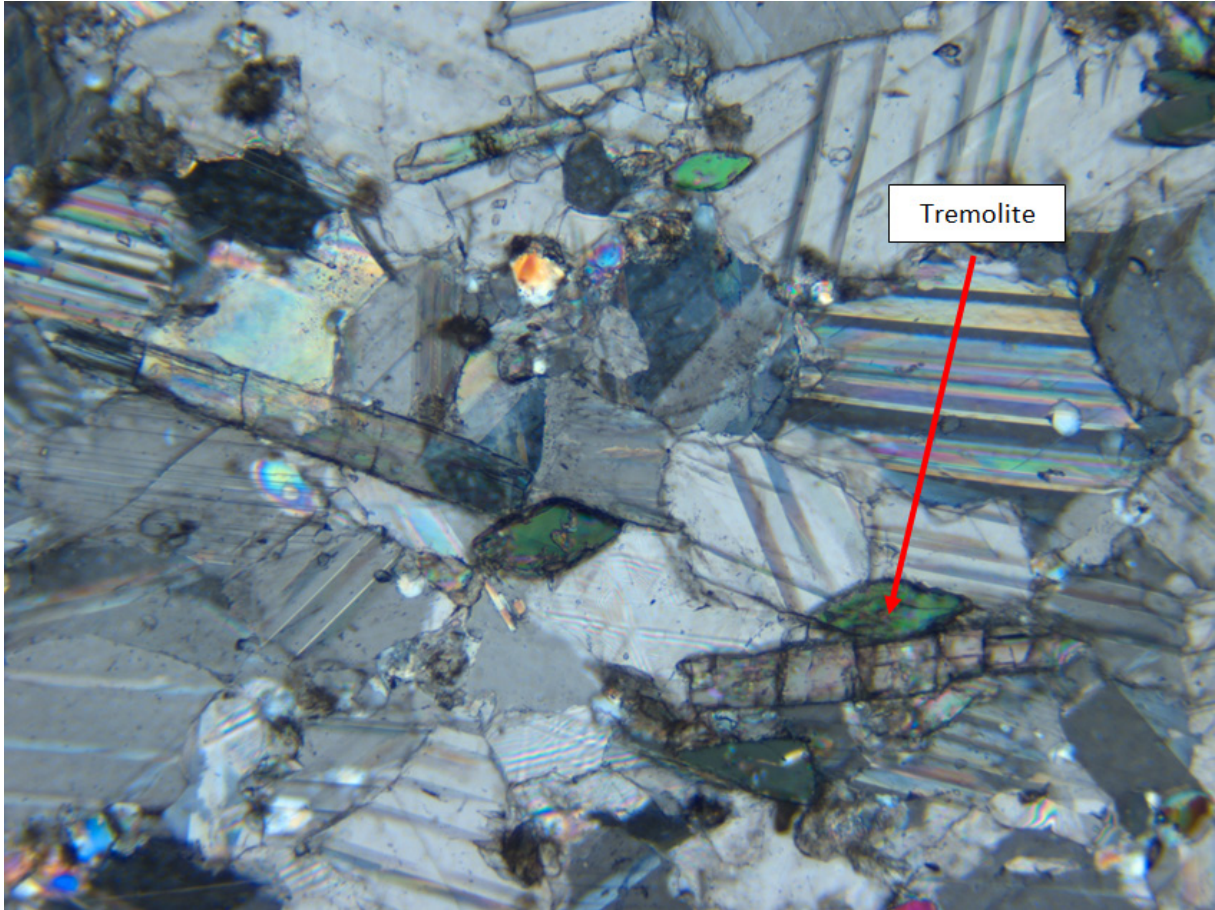


Figure 31: Calcite with accessory tremolite (image length 2,85 mm).

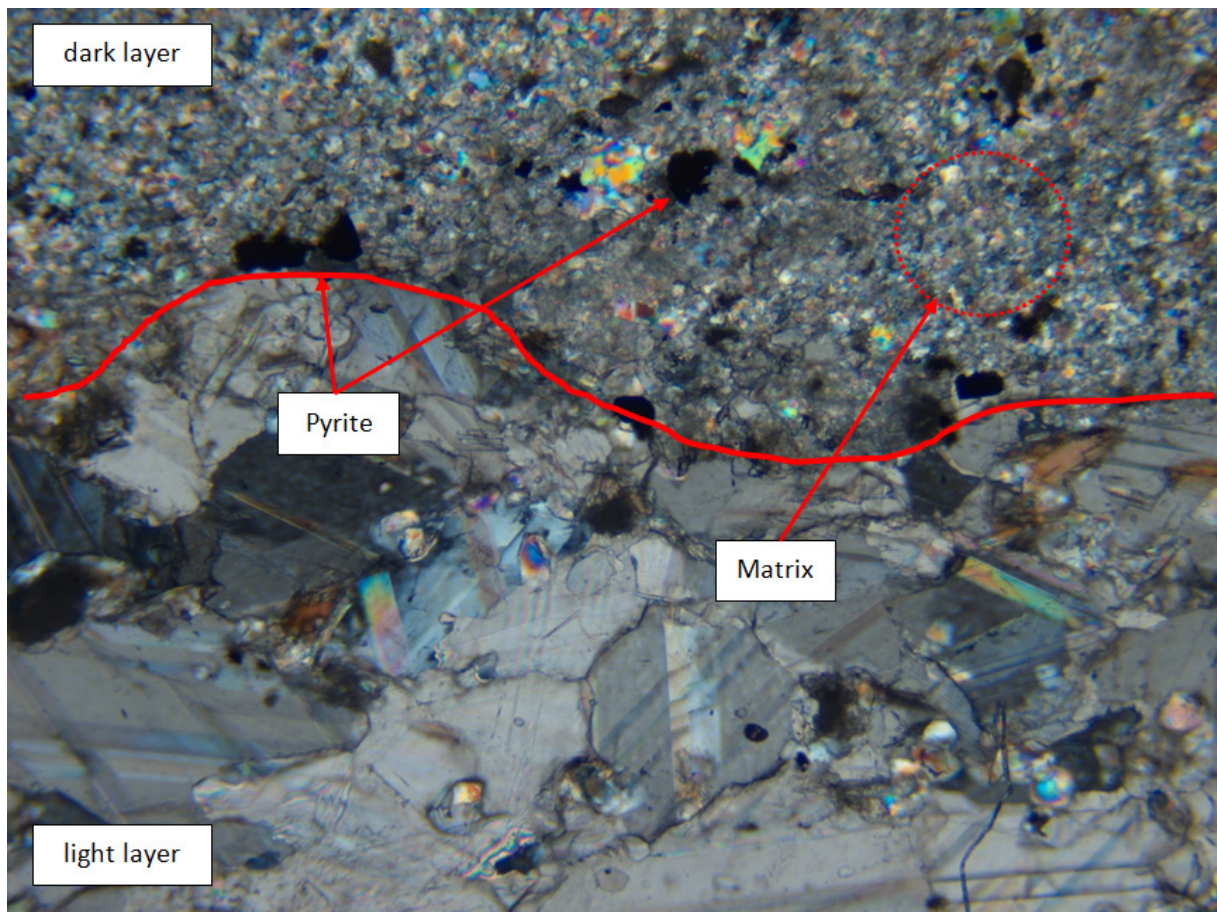


Figure 32: Transition between gray and light layers (image length 2,85 mm).

1.7 High-Mg potassic lamprophyre dykes

In the late Jurassic lamprophyre dyke swarms intruded the magnesite deposit. More than 4 lamprophyre dykes occur in the Aihai open pit, all NNE-trending and each being 1–3 m thick (Figure 33). The contact to the ore is sharp and displays a thin brown-fried border zone. The dykes show no concomitant alteration of the magnesite ore. The lamprophyres consist of a greenish black groundmass with phenocrysts (Figure 34). Under the microscope the lamprophyre dykes illustrates typical lamprophyric (panidiomorphic) texture. The dykes consist of epidote, augite, feldspar ledges and heavy altered olivine (Figure 35).

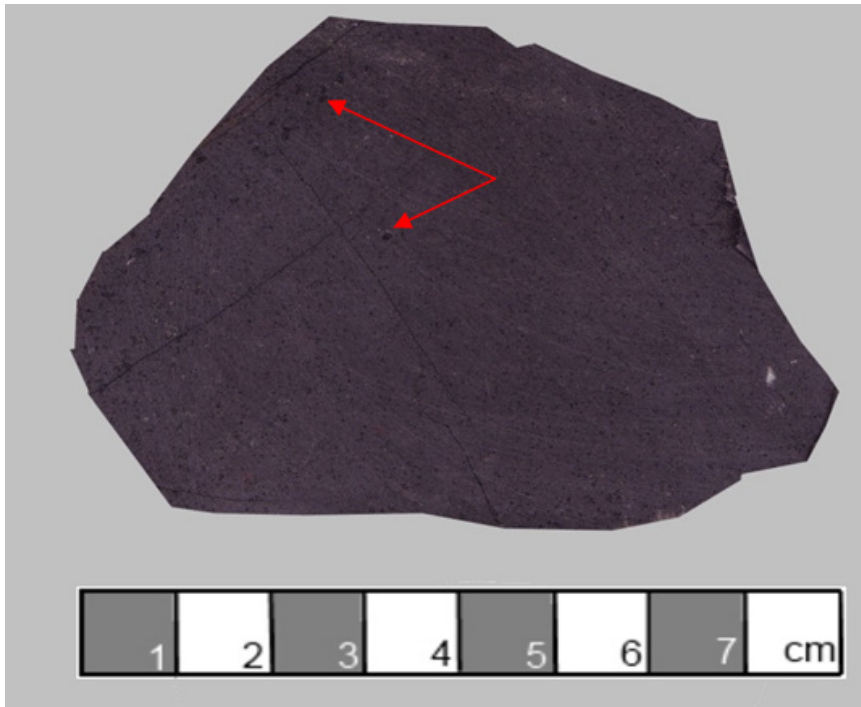


Figure 33: Greenish black groundmass with phenocrysts (black dots).



Figure 34: Discordant lamprophyre dyke (bench face). Dyke thickness 1,5m.

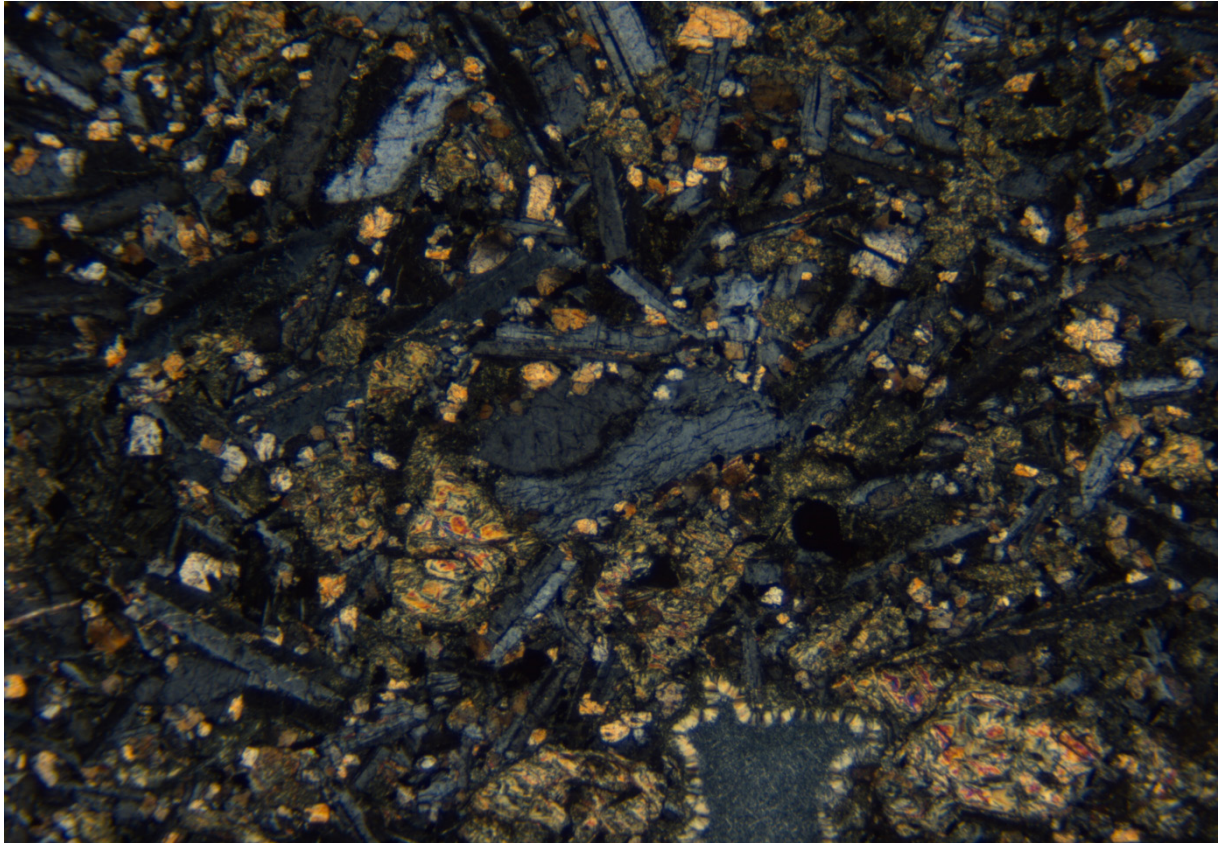


Figure 35: Typical lamprophyric (panidiomorphic) texture (image length 2,85 mm).

1.8 White fine-grained magnesite

The massive white fine-grained magnesite type shows a crystal-structure like sugar. The crystals are transparent to pale white and cloudy grey. This massive magnesite is often associated with magnesite sinter veins, which are accrued in open joints (Figure 36 and 37). It is not unusual, that the massive white magnesite changes sharply into a dark grey magnesite. The mineral composition of the white fine-grained magnesite ore is simple and contains 99.9% of magnesite. The grains are strongly interlocking along their boundaries. It is possible to distinguish three different structural types of magnesite crystals (Figure 38). They are characterized by their crystal size, small dark inclusions (organic matter?), dolomite relics within the magnesite crystals and undulating extinction.



Figure 36: White fine-grained magnesite outcrop, with magnesite sinter veins crosscutting dark grey magnesite.

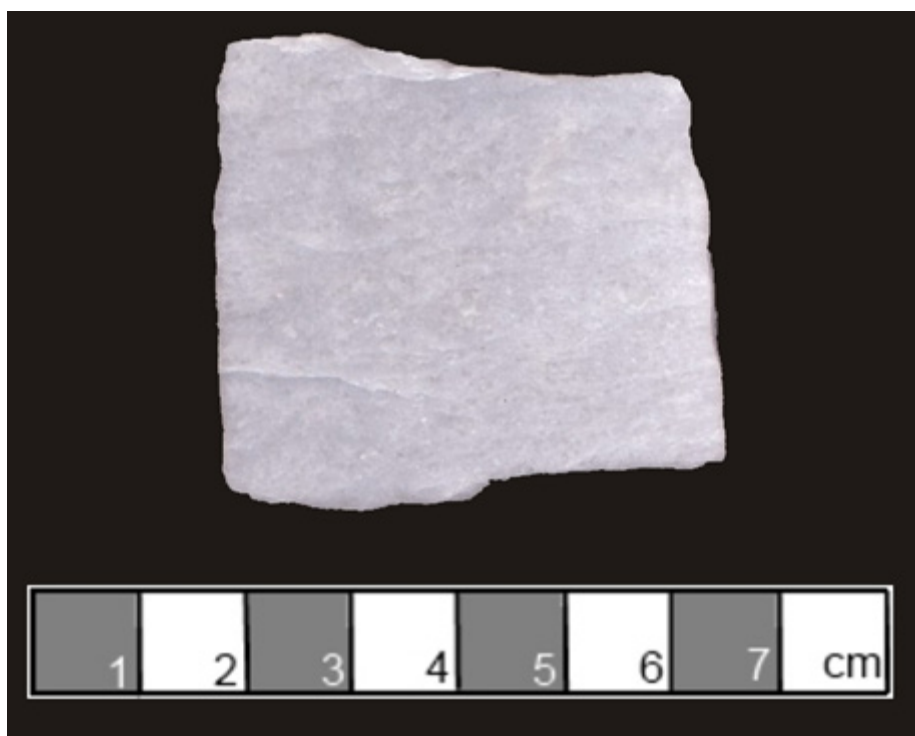


Figure 37: Polished specimen from the white fine-grained magnesite. Sugar like crystal-structure.

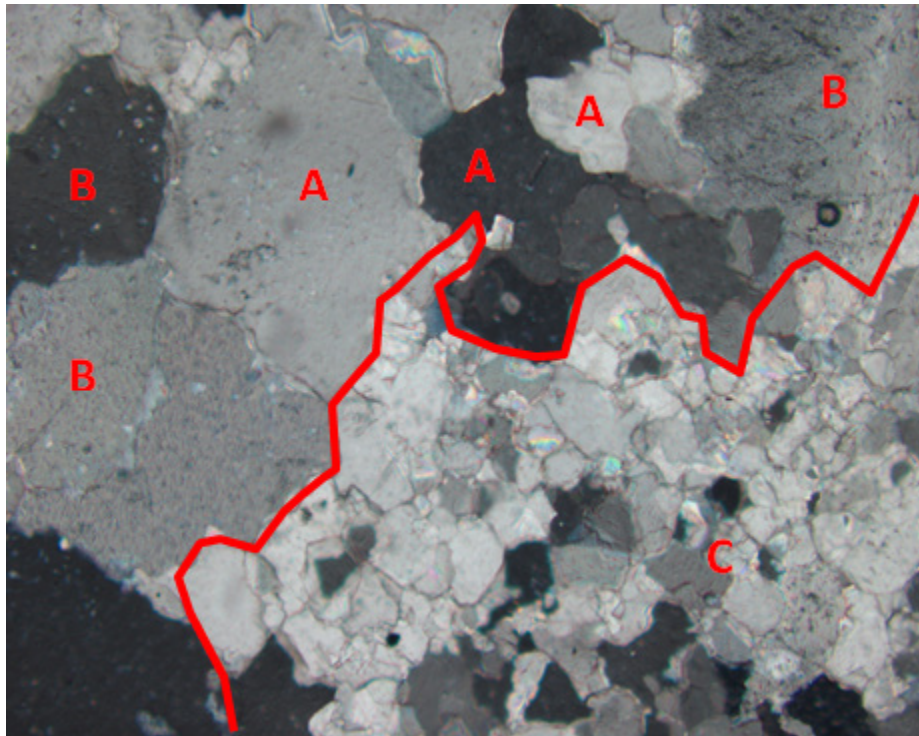


Figure 38: Photomicrograph of the white fine-grained magnesite. A points to relatively coarse crystals with no inclusions; B marks coarse crystals with inclusions of dolomitic relics; C indicates fine crystals of undulatory extinction (image length 2,85 mm).

1.9 Grey fine-grained magnesite

The grey fine-grained magnesite is similar to the white fine-grained magnesite. In contrast to the white magnesite the grey one is occurring in heavily tectonized areas. The fault planes show heavy distinct magnesite stylolites (Figure 39). The coloration of the tectonized magnesite changes its color from light to dark grey over decimeters. The color changes are fluent passages. The polished specimen shows slightly darker and lighter areas (Figure 40). The photomicrograph of the grey fine-grained magnesite displays pure magnesite. The fabric is analogical to the white fine-grained magnesite (Figure 41).



Figure 39: Grey fine-grained magnesite outcrop with stylolites.

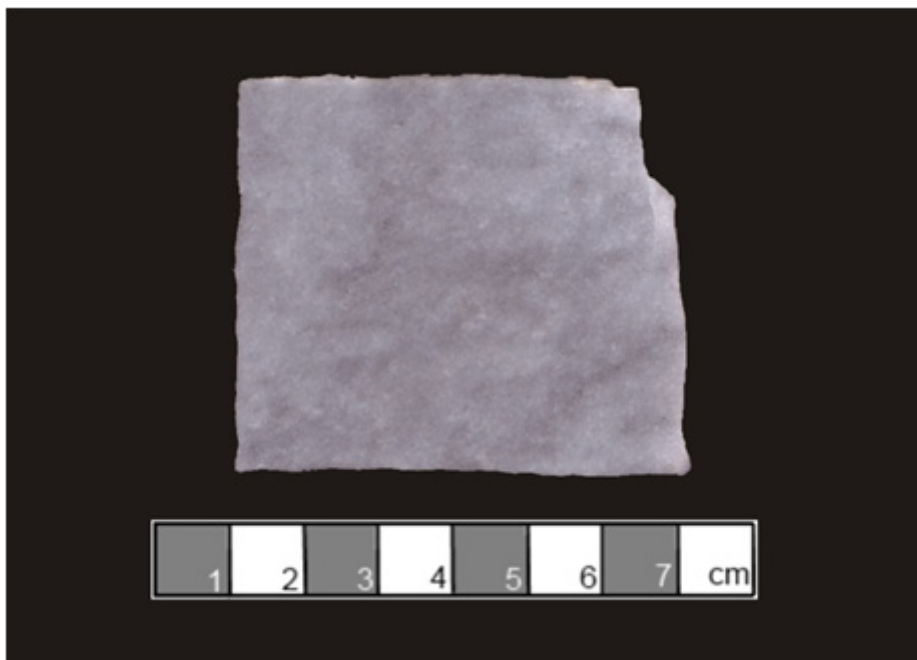


Figure 40: Polished specimen of pure magnesite with slightly lighter and darker areas.

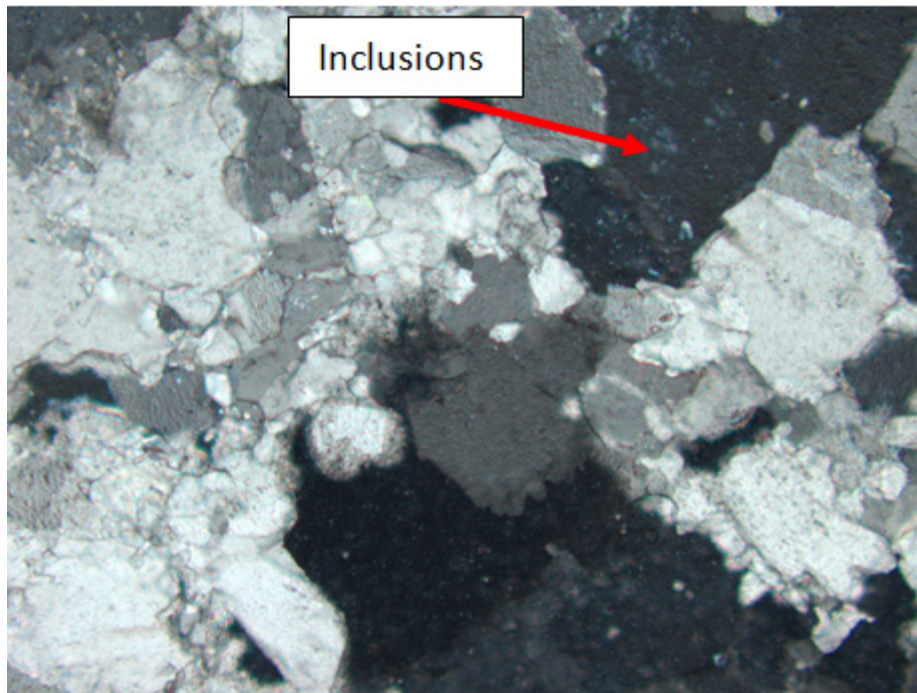


Figure 41: Photomicrograph of the grey fine-grained magnesite. Coarser crystals with dolomitic inclusions and finer crystals, which are interlocking along their boundaries (image length 2,85 mm).

1.10 Dark medium-grained magnesite, containing talc and Mg-chlorite

The dark medium-grained magnesite is mainly associated with tension gashes, which were filled with talc and Mg-chlorite during deformation (Figure 42). The filled tension gashes have a thickness between 0,5cm up to 2cm. The color of the vein material is pale white to yellow. The gashes occur at 20-30cm distances and are linked to the dark medium grained magnesite. The polished specimen contains a talc and chlorite bearing vein in magnesite host rock (Figure 43). The central parts of the vein show typically a pale white-yellow color. The rim is light brown.



Figure 42: Dark medium grained magnesite, with tension gashes, which are filled with talc and Mg-chlorite.

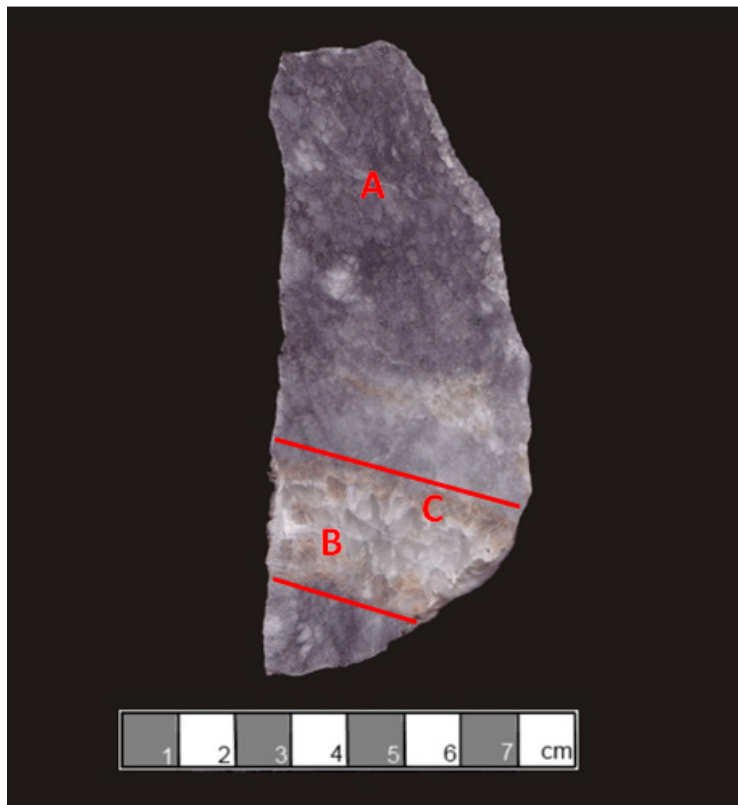


Figure 43: Polished hand specimen of dark medium grained magnesite with tension gash. A shows the dark intact magnesite rock. B displays the core of the refilled material, mainly talc. C represents the border zones of the vein, which consist of talc and Mg-chlorite.

The photomicrographs illustrate two different transition zones, one between magnesite and the vein filling and the other one between talc and Mg-chlorite. Figure 44 (a) shows intergrown talc and Mg-chlorite. The talc crystals displays high tectonic stress compared to the Mg-chlorite crystals. This indicates that the talc is older than the Mg-chlorite. The upper left part of the image shows heavily altered magnesite crystals. Figure 44 (b) illustrates the replacement structure between the talc and the magnesite. Talc starts to replace magnesite along the cleavage plane and at the crystal boundaries.

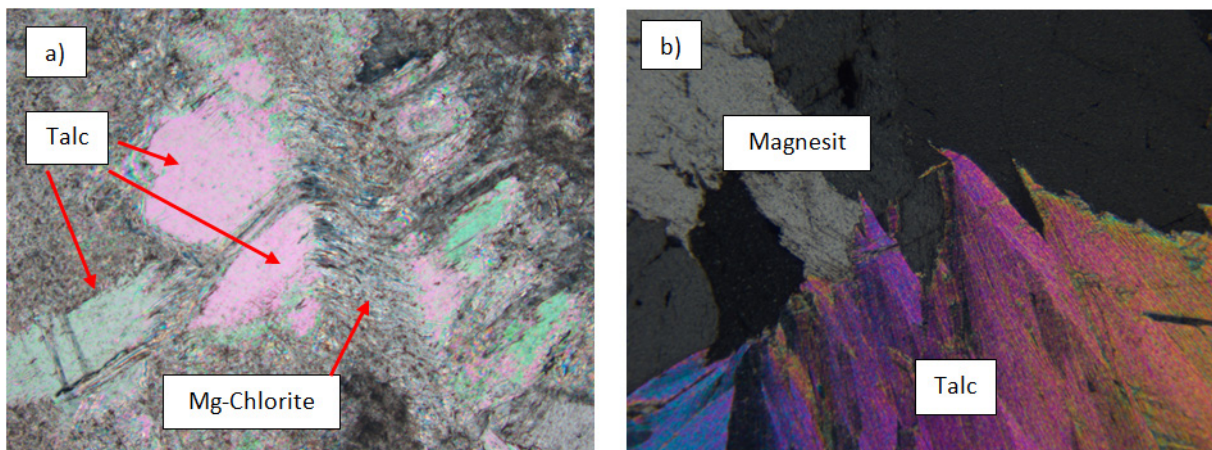


Figure 44: (a) Talc and Mg-chlorite intergrowth (1,77 mm). (b) Talc and magnesite intergrowth (2,85 mm).

1.11 Dark grey/white mottled magnesite

The dark grey/white mottled magnesite is bound to high tectonized areas. The mottled magnesite is mainly associated with the dark medium-grained magnesite and the talc filled tension gashes (Figure 45). The mottled feature is caused by dark veins and lamination. The veins and lamination are composed of insoluble materials such as graphite and show no regular orientation (Figure 46). Under the microscope the dark grey/white mottled magnesite displays coarse spotted magnesite crystals, mainly due to the presence of abundant tiny dolomitic inclusions. A dolomite precursor is assumed. The smaller subhedral magnesite crystals are non-planar, closely packed with undulatory extinction (Figure 47). Accessorily primary quartz and graphite are present, but the small amount of quartz has negligible influence on the ore quality.

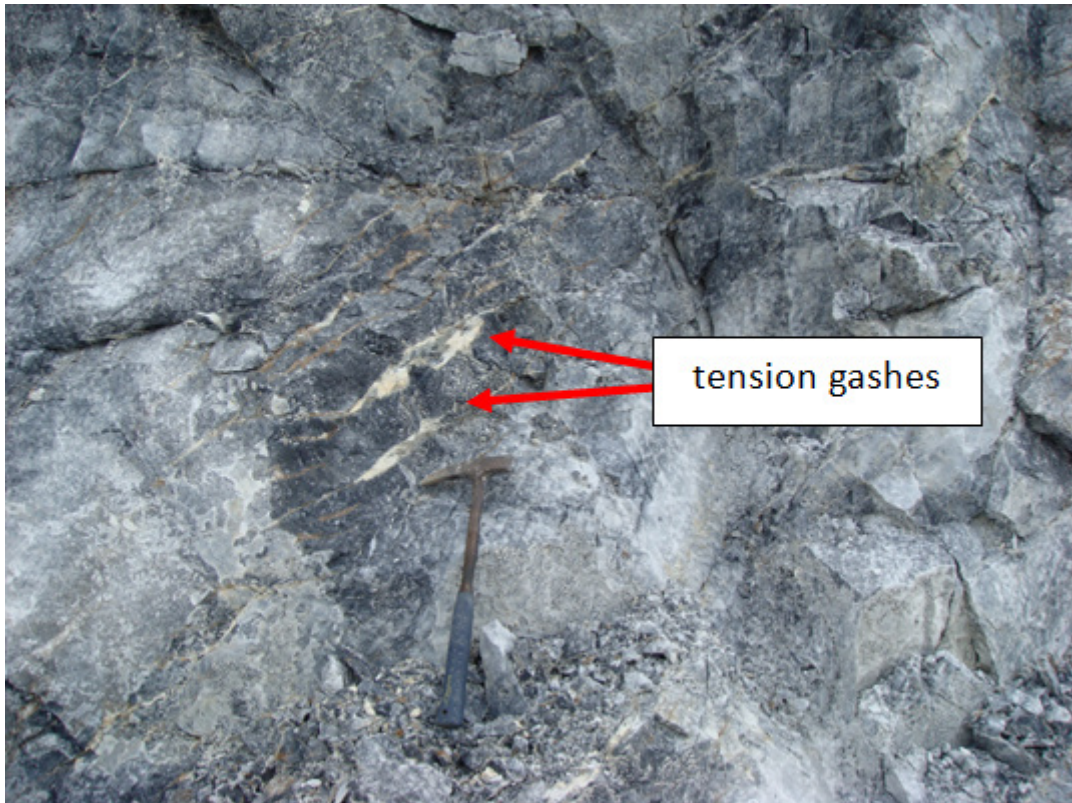


Figure 45: Outcrop of the dark grey/white mottled magnesite with talc filled tension gashes.

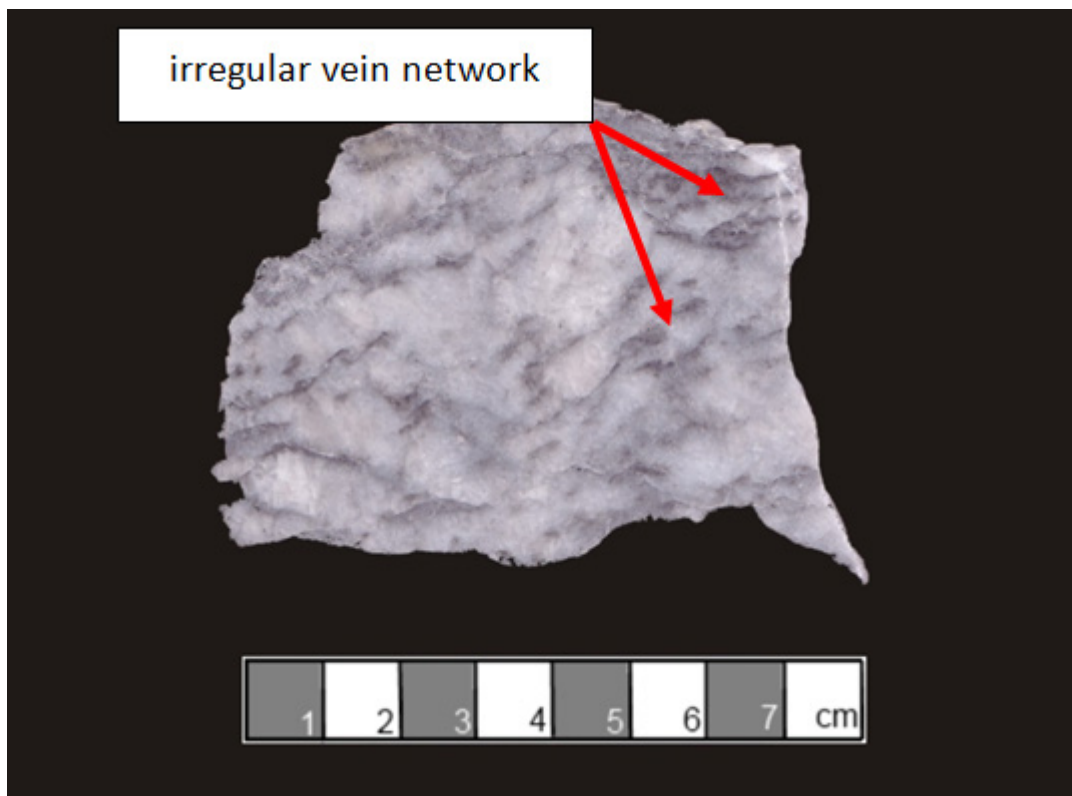


Figure 46: Polished specimen with irregular zebra replacement bands.

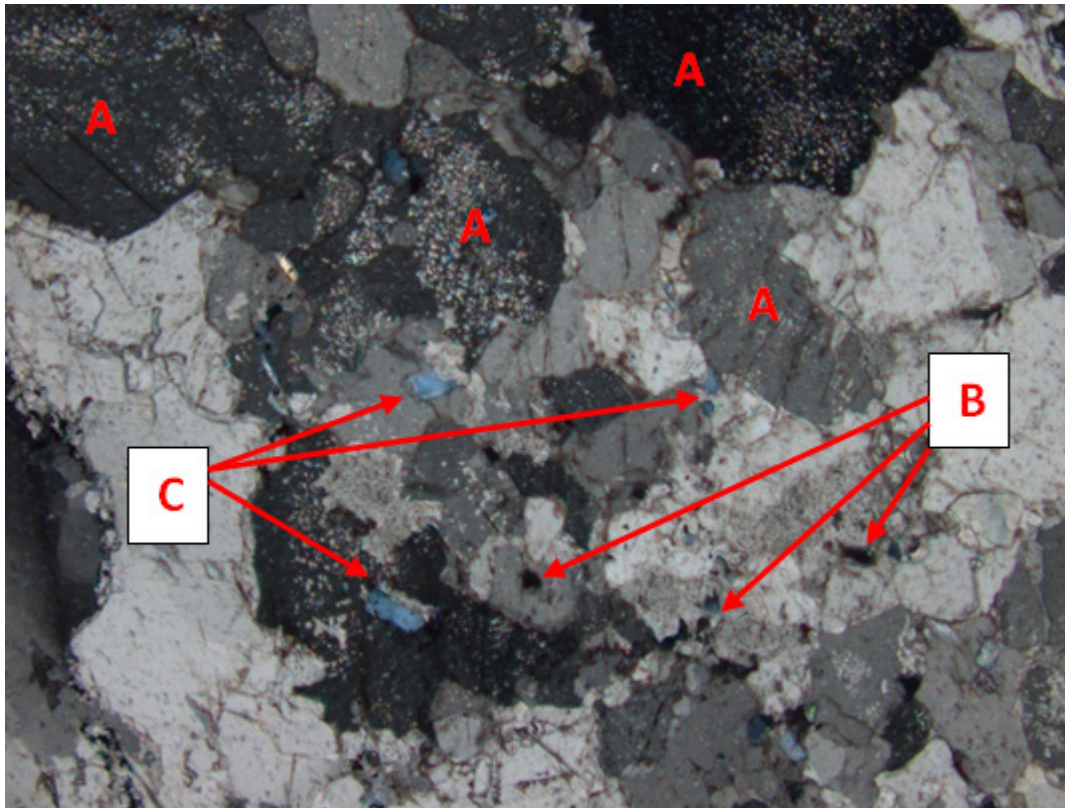


Figure 47: Photomicrograph of mottled magnesite. A) represents the coarse magnesite crystals with dolomitic inclusions. B) Graphite. C) Primary autogenous quartz (image length 1,77 mm).

1.12 Magnesite sinter veins

The majority of the magnesite sinter fills extension faults, which crosscut the whole deposit. The extension faults are vertical and strike predominantly N–S. Vein widths range from several millimeters to a maximum of 15cm (Figure 48). The spacing of the veins is variable. In extension veins, the magnesite is often bi-polarly grown contemporaneously from both walls into the interior of the fractures. The field observation reveals that many veins appear as composite veins, which have been formed during a series of individual ruptures. Polycrystalline breccias and several generations of healed fractures inside the veins are locally common (Figure 49). These features indicate that veining and the subsequent crystallization of vein minerals were a complex, multistage process rather than a single event (Figure 50).

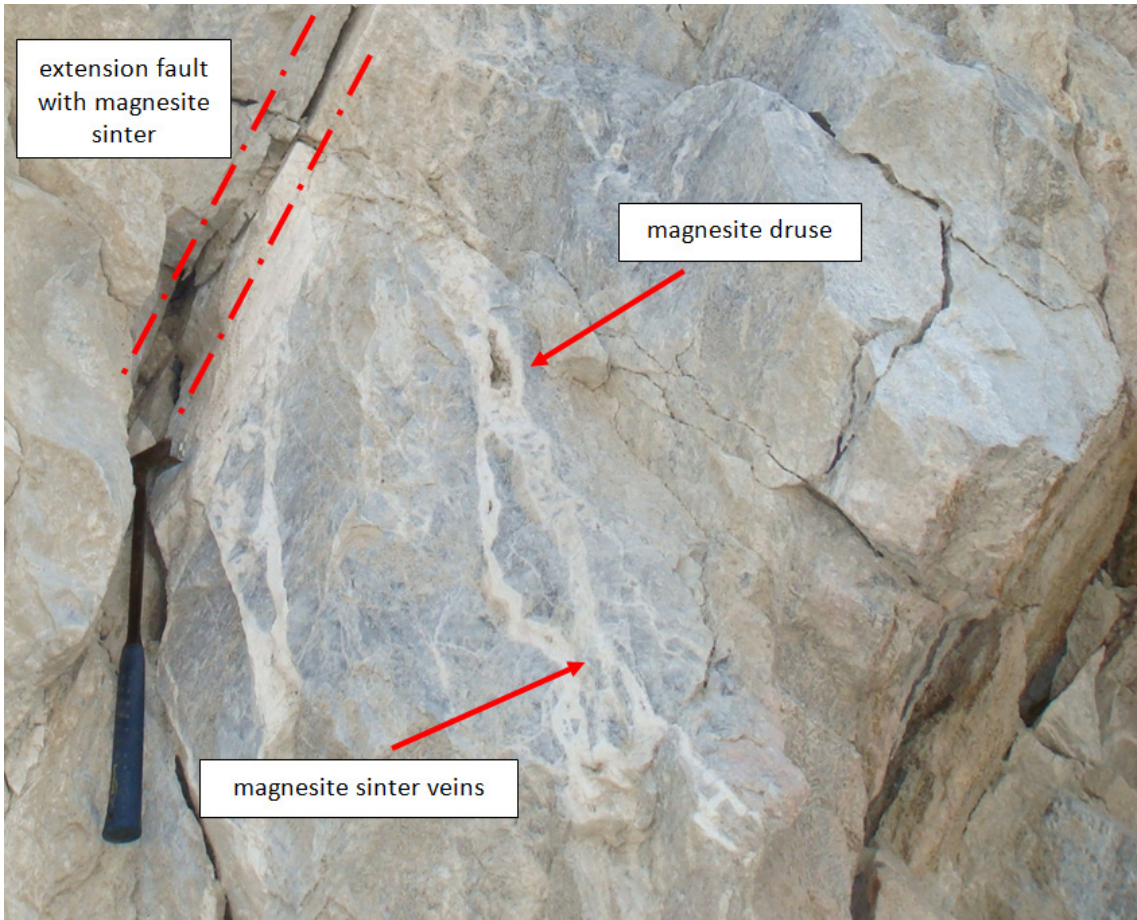


Figure 48: Outcrop of high quality ore with magnesite sinter veins.

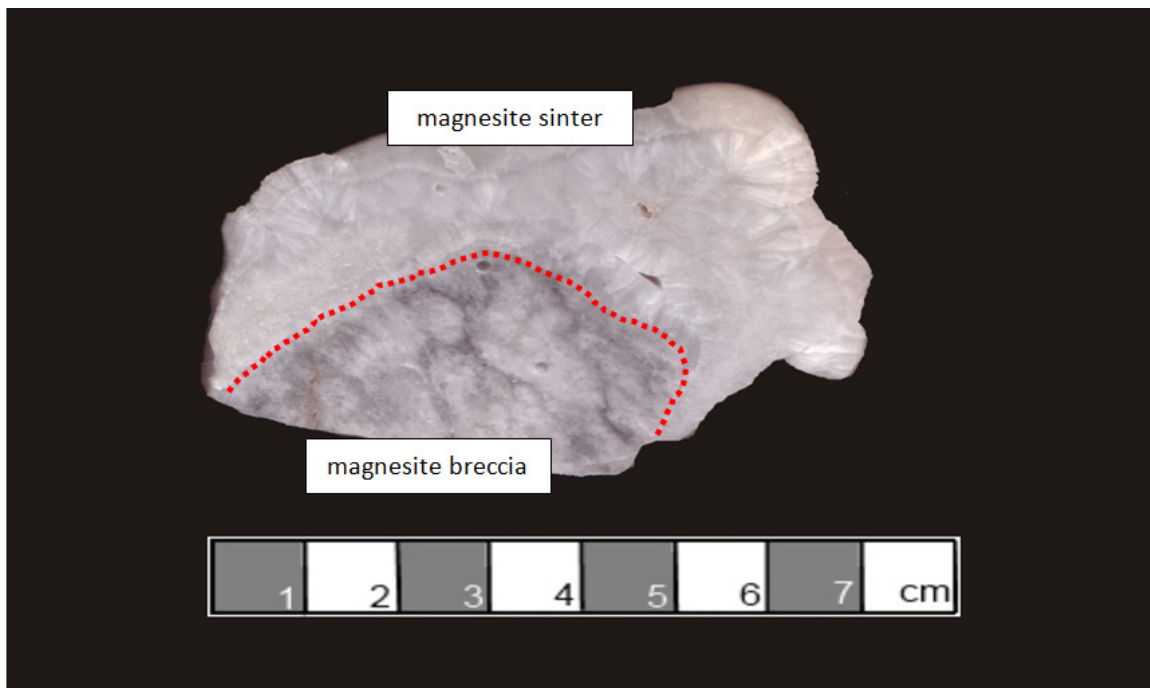


Figure 49: Polished specimen of a magnesite breccia. The magnesite clast is overgrown by magnesite sinter.

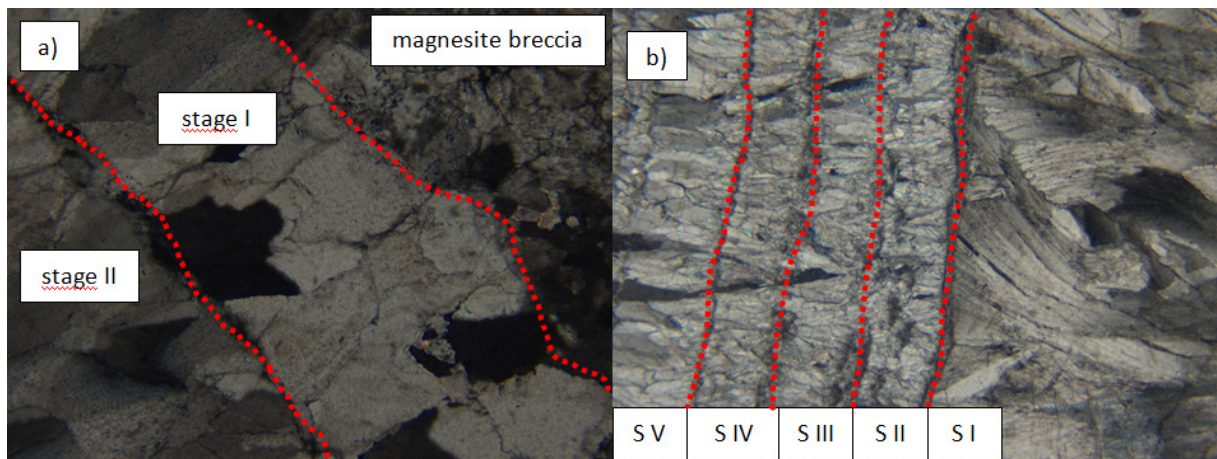


Figure 50: (a) & (b) Photomicrographs of magnesite sinters, illustrating the different crystallization stages (image length 2,85 mm).

1.13 Talc/Mg-chlorite bound to tectonized zones

In the northern part of the open pit several talc/Mg-chlorite hosting shear zones are occurring. The shear zones are parallel to the primary bedding of the magnesite ore and dip medium steep to the South. The thicknesses of the talc/Mg-chlorite zones vary from decimeter to one meter (Figure 51). The shear zone can be divided into a core zone and two rim zones. The core zone is characterized by brown weathered compact rock that consists mainly of talc, Mg-chlorite, pyrite and magnesite relics. The brown staining is caused by limonite. The competent core zone is broken into massive pieces. The rim zones are dominated by intense shearing, and compared to the core zone it is relatively soft. The coloration of the rim zones are light grey and contain no pyrite or magnesite inclusions. The adjacent magnesite layers hold small centimeter sized talc bodies. Tectonic stress did not affect the small talc bodies; therefore they have a massive habitus and show no signs of tectonic elongation or shear induced structures.

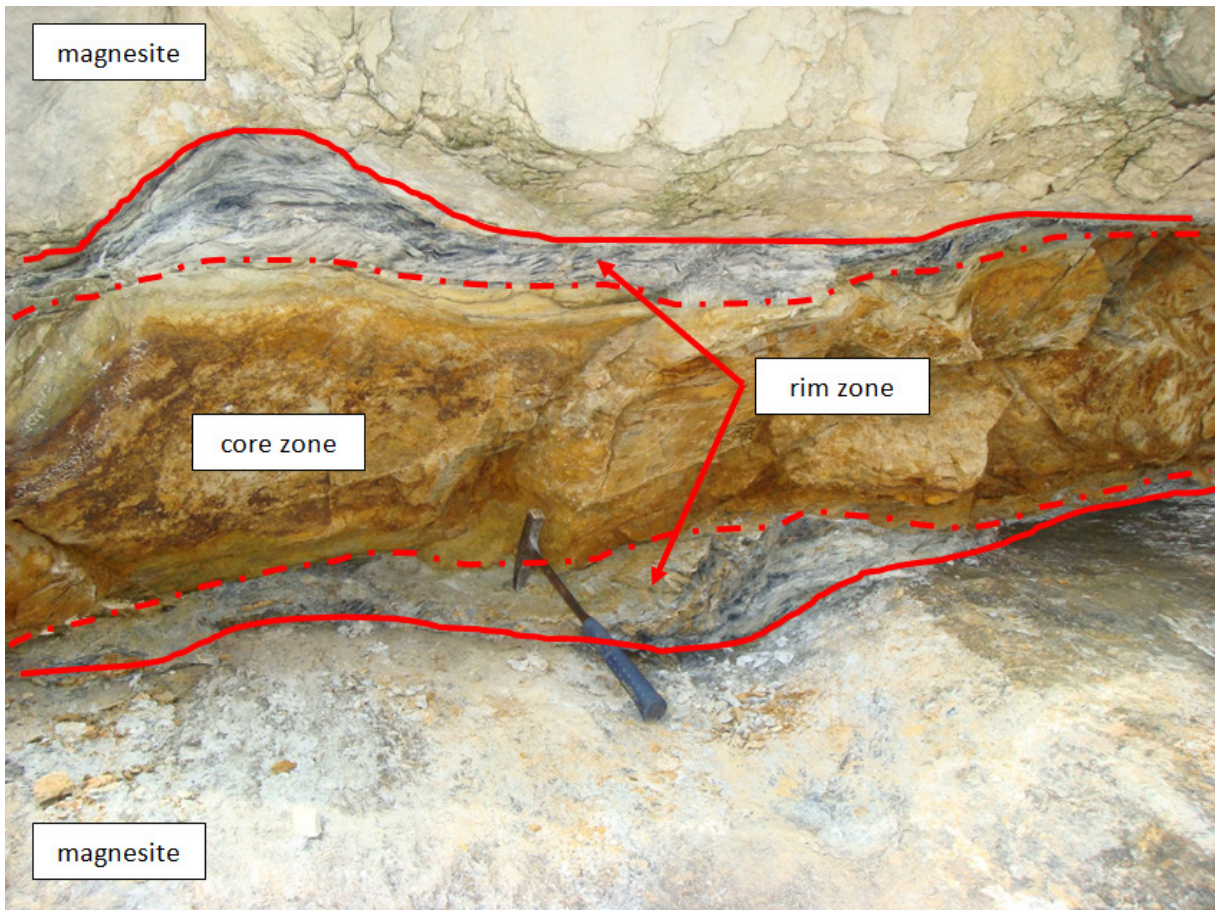


Figure 51: Talc/Mg-chlorite hosting shear zone.

1.14 Fibrous sepiolite on slickenside surfaces

Based on field data and textural relations detected in the sepiolite-magnesite veins, the sepiolite is assumed to have formed mainly by in situ replacement of magnesite (Figure 52). Magnesite was apparently replaced volume by volume. The pure sepiolite veins represent either completely replaced magnesite veins formed by precipitation of sepiolite directly from silicium and magnesium-rich solutions. This variety of sepiolite consists of bundles of white, 3-5cm long fibres. The fibres are oriented exactly parallel, are of a slight grey shade with parallel extinction under the microscope.



Figure 52: Fibrous sepiolite on a slickenside surface.

Geochemistry of the magnesite ore and the related rocks

1.15 Major Elements

In order to understand the geochemical characteristic of the magnesite ore body, the intercalated dolomitic marble with minor carbonaceous schist and the micaschist; 48 samples were chemically analyzed. Each sample weighing between 2 and 5 kilograms and cleaned of visible surface alteration. The samples are from the third section (sub-formation) of the Dashiqiao Formation from the Aihai magnesite open-pit. The samples are divided into five major categories: magnesite ore, dolomitic marble, carbonaceous schist, mica schist and associated rocks (lamprophyre dykes, talc, sepiolite etc.), which cause a reduction in quality of the magnesite ore.

These 48 rock samples in this study were analyzed in the Activation Laboratories Ltd. (Actlabs), in Ontario, Canada. SiO₂, Al₂O₃, total FeO, MnO, MgO, CaO, Na₂O, K₂O, TiO₂, P₂O₅ were determined by inductively coupled plasma optical emission spectrometry (ICP-OES) and the trace elements by inductively coupled plasma mass spectrometry (Perkin Elmer Sciex ELAN 9000 ICP/MS).

Among these samples, 31 are from magnesite ore of the center part of the ore body in the open pit; 4 samples are from the intercalated carbonaceous schist; 5 samples from the intercalated dolomitic marbles, 2 samples from the intruded lamprophyre dikes and 2 samples from the footwall, which composed of mica schist with randomly occurring calcite inclusions.

The results of the chemical whole rock analyses from the mayor elements are reported in Table 1.

Sample ID	Group	SiO ₂	Al ₂ O ₃	Fe ₂ O ₃ (T)	MnO	MgO	CaO	Na ₂ O	K ₂ O	TiO ₂	P ₂ O ₅	LOI	Total
MG-Z	<i>Magnesite</i>	0,81	0,04	0,22	0,011	47,59	0,61	< 0.01	0,01	0,002	0,02	51,59	100,9
MG-S	<i>Magnesite*</i>	0,06	0,02	0,07	0,005	48,43	0,47	< 0.01	< 0.01	0,001	< 0.01	51,87	100,9
1-1	<i>Magnesite</i>	0,28	0,02	0,7	0,041	47,4	0,34	< 0.01	0,01	< 0.001	0,01	51,9	100,7
2-1	<i>Magnesite**</i>	1,2	0,04	1,59	0,086	45,99	0,58	< 0.01	< 0.01	< 0.001	0,03	51,03	100,6
8-1	<i>Magnesite</i>	0,63	0,09	1,09	0,058	46,73	0,58	0,02	0,01	0,008	< 0.01	51,36	100,6

8-4	Magnesite	0,27	0,03	0,17	0,008	48,56	0,33	< 0.01	< 0.01	0,002	0,03	51,59	101
8-8	Magnesite**	0,74	0,12	0,17	0,008	47,35	1,11	< 0.01	< 0.01	0,004	0,35	50,57	100,4
8-9	Magnesite	0,47	0,02	0,84	0,049	47,74	0,4	< 0.01	< 0.01	< 0.001	0,07	51,32	100,9
8-10	Magnesite **	2,79	0,62	1,46	0,082	42,14	5,38	< 0.01	< 0.01	0,028	0,2	47,78	100,5
11-1	Magnesite	0,43	0,07	0,27	0,012	47,75	1,02	< 0.01	0,01	0,002	0,39	50,99	100,9
11-2	Magnesite	0,55	0,07	0,24	0,012	47,16	1,14	< 0.01	< 0.01	0,002	0,43	50,78	100,4
13-1	Magnesite**	1,27	0,69	0,35	0,015	46,5	0,84	< 0.01	< 0.01	0,028	0,02	50,28	100
13-2	Magnesite*	0,47	0,15	0,12	0,006	47,51	0,76	< 0.01	< 0.01	0,004	< 0.01	51,07	100,1
15-1	Magnesite	0,22	0,07	0,33	0,013	47,43	0,45	0,01	0,02	0,002	0,01	51,34	99,91
15-2	Magnesite	0,24	0,04	0,33	0,021	47,78	0,6	< 0.01	< 0.01	0,004	0,07	51,25	100,3
16-1	Magnesite	0,48	0,12	0,22	0,01	47,96	0,59	< 0.01	0,03	0,004	0,02	51,26	100,7
16-2	Magnesite	0,92	0,04	0,17	0,009	47,29	0,63	< 0.01	< 0.01	0,005	0,02	50,87	99,97
18-1	Magnesite	0,06	0,02	0,25	0,012	48,3	0,5	< 0.01	< 0.01	< 0.001	< 0.01	51,4	100,6
19-1	Magnesite	0,47	0,04	0,32	0,031	47,44	0,28	< 0.01	< 0.01	0,005	< 0.01	51,33	99,92
19-2	Magnesite	0,06	0,03	0,57	0,036	47,12	0,33	< 0.01	< 0.01	0,002	< 0.01	51,31	99,48
18-2	Magnesite*	0,12	0,05	0,14	0,008	46,78	1,07	< 0.01	< 0.01	0,001	< 0.01	51,11	99,31
23-1	Magnesite	0,64	0,09	0,23	0,01	46,11	1,75	0,03	0,01	0,003	0,01	50,55	99,44
24-1	Magnesite	5,59	0,52	0,29	0,013	44,02	1,59	0,02	0,13	0,024	0,04	48,2	100,4
24-2	Magnesite	5,1	1,32	0,32	0,015	44,16	1,05	0,02	0,3	0,06	0,04	48,04	100,4
3-1	Magnesite + Talc**	16,85	0,31	0,35	0,013	30,73	15,43	< 0.01	< 0.01	0,017	0,17	37	100,9
7-1	Magnesite + Talc	9,07	1,58	0,35	0,011	41,67	4,33	0,02	0,01	0,063	0,02	43,45	100,6
8-3	Magnesite+ Talc	9,11	1,38	0,18	0,007	43,14	0,87	0,02	0,04	0,049	0,05	45,66	100,5
16-3	Magnesite + Talc	7,05	0,25	0,19	0,009	45,76	0,71	0,02	< 0.01	0,018	0,02	46,81	100,9
21-2	Magnesite + Tremolite	9,86	0,02	0,18	0,009	43,43	4,17	< 0.01	< 0.01	0,001	0,03	42,21	99,92
22-3	Magnesite + Talc	6,82	0,09	0,33	0,024	43,34	0,93	0,01	< 0.01	0,002	< 0.01	47,92	99,49
23-2	Magnesite + Talc	10,86	0,04	0,14	0,008	37,54	9,02	0,02	< 0.01	< 0.001	0,01	42,17	99,82
5-1	Carbonaceous Schist	26,89	5,89	2,4	0,024	17,93	21,57	0,03	3,17	0,217	0,05	21,62	99,8
6-1	Carbonaceous Schist	45,05	10,92	3,93	0,017	10,83	15,69	0,14	5,04	0,43	0,09	8,35	100,5
6-3	Carbonaceous Schist	30,51	5,22	1,47	0,015	2,8	31,57	0,23	2,54	0,201	0,05	24,86	99,46
14-1	Carbonaceous Schist	18,81	3,8	0,68	0,013	25,29	18,81	< 0.01	< 0.01	0,15	0,05	31,98	99,59
10-1	Dolomitic Marble	1,39	0,36	0,19	0,022	21,63	29,36	< 0.01	< 0.01	0,014	0,3	45,46	98,74
20-1	Dolomitic Marble	10,25	0,01	0,03	0,003	20,68	29,19	< 0.01	< 0.01	< 0.001	0,02	38,33	98,52
21-3	Dolomitic Marble	6,76	0,04	0,17	0,009	33,43	14,99	0,01	< 0.01	< 0.001	0,03	44,1	99,55
22-4	Dolomitic Marble	10,88	0,02	0,04	0,004	21,08	28,26	< 0.01	< 0.01	< 0.001	< 0.01	37,97	98,26
24-3	Dolomitic Marble	4,68	0,54	0,36	0,007	20,96	28,49	0,03	0,07	0,016	0,02	43,49	98,67

22-1	<i>Dyke</i>	48,67	13,77	11,03	0,109	8,63	7,64	2,49	0,53	1,466	0,2	4,11	98,63
22-2	<i>Dyke</i>	48,87	14,18	11,33	0,119	7,45	8,45	2,55	0,51	1,565	0,2	3,49	98,7
9-1	<i>Mica-Schist</i>	61,37	18,14	5,45	0,018	3,3	0,13	0,12	5,77	0,72	0,06	4,86	99,95
9-2	<i>Mica-Schist + Calcite Inclusions</i>	29,36	6,71	3,57	0,051	5,87	23,84	0,04	2,12	0,385	0,1	27,35	99,39
8-2	<i>Talc</i>	39,21	0,03	0,14	0,005	37,86	0,24	< 0.01	< 0.01	0,001	< 0.01	23,01	100,5
8-7	<i>Talc + Chlorite</i>	33,19	19,44	1,98	0,003	33,56	0,12	< 0.01	0,09	0,726	0,09	11,75	100,9
14-2	<i>Talc + Chlorite**</i>	59,37	12,73	2,99	0,005	10,1	1,89	0,07	3,14	0,449	0,09	7,94	98,78
21-3+	<i>Talc</i>	51,58	0,02	0,08	0,003	30,16	5,57	< 0.01	< 0.01	0,002	< 0.01	11,85	99,28

Table 1: Major elements [%] analyses from the rock samples;*younger magnesite precipitation in fissures (magnesium sinter); rock samples adjunct to faults.**

1.15.1 Magnesite ore

The average geochemistry of the selective mined magnesite is MgO 46.89 wt. %, CaO 0.93 wt. %, SiO₂ 0.99 wt. %, Fe₂O₃ (Total) 0,44 wt. % and the LOI 50.78 wt. %. The chemical composition of selected magnesite samples from the open pit shows variations in the MgO, SiO₂ and the CaO value. The bulk composition of magnesite (Table 1) ranges from 37.54 to 48.56 wt. % of MgO, the lowest contents occur in the transition zones to the dolomitic marbles and in younger brittle shear zones. In turn, the CaO varies from 0.28 to 15.43 wt. %, with the highest values in the contacts with the dolomitic marbles. The variation of the CaO content is explainable by the features of late redolomitization and relics of dolomite inclusions. In the open pit the redolomitization is mainly caused by ascending surface water through young brittle shear zones. SiO₂ varies from 0.06 to 16.85 wt. %, the SiO₂ variations caused by talc/Mg-chlorite filled tension joints and sometimes quartz filled micro joints. The SiO₂ derive from metamorphic fluids. The Al₂O₃ content varies from 0.02 to 1.58 wt. % and the Fe₂O₃ values are lower than 1.5 wt. % (0.07 to 1.46). MnO varies from 0.005 to 0.086 wt. % with highest values found next to the shear zones. P₂O₅ presents low contents and usually around 0.03 wt. %, the TiO₂ value varies from 0.001 to 0.063 wt. %.

1.15.2 Carbonaceous schists (siliceous green marble)

The carbonaceous schists, which intercalate the ore body, exhibit MgO from 2.8 to 25.29 wt. %, the lowest values are found in calciferous light green layers. SiO₂ varies from 18.82 to 45.05 wt. %, the highest values found in heavy silicified dark green layers. Al₂O₃ ranges from 3.8 to 10.92 wt. % and the Fe₂O₃ from 0.68 to 3.93 wt. %. CaO varies from 18.81 to 31.57 wt. % and MnO from 0.013 to 0.024 wt. %. P₂O₅ is constant around 0.05 wt. %. TiO₂ varies from 0.15 to 0.43 wt. %, Na₂O from 0.03 to 0.23 wt. % and K₂O from 2.54 to 5.04 wt. %.

1.15.3 Dolomitic marbles

The dolomitic marbles mainly located in the transition zone to the hanging wall and one layer in the footwall of the ore body. The dolomitic marbles display CaO values from 14.99 to 29.36 wt. % and MgO from 20.68 to 33.43 wt. %. The SiO₂ varies from 1.39 to 10.88 wt. %, Fe₂O₃ from 0.04 to 0.36 wt. %, MnO from 0.003 to 0.022 wt. %, Al₂O₃ from 0.01-0.54 wt. %, TiO₂ from 0.014 to 0.016 wt. % and P₂O₅ from 0.02 to 0.3 wt. %.

1.15.4 Micaschists with calcite inclusions

In the footwall of the magnesite ore body mica schists, with calcite inclusions, are present. These schists form the upper part of the second section of the Dashiqiao Formation and represent a geological barrier. The SiO₂ varies from 29.36 to 61.37 wt. %, Al₂O₃ from 6.71-18.14 wt. % and the CaO from 0.13-32.84 wt. %.

1.15.5 Lamprophyre dikes

The lamprophyre dyke samples show a homogenous range of SiO₂ (48.67-48.87 wt. %) and MgO from 7.45 wt. % to 8.63 wt. %. The samples have moderate alkalis contents (K₂O + Na₂O = 3.04 wt. %) and have lower volatile contents, with LOI up to 4.11 wt. %, as lamprophyres from the Huaziju magnesite open pit (15 km South from Haicheng City).

The major elements in the meta-carbonates from the Aihai open-pit under consideration are plotted in the Fe₂O₃+SiO₂-CaO-MgO diagram. These rocks plot

preferentially in the magnesitic-dolomitic marble field and show an additional field from the carbonaceous slates (Figure 53).

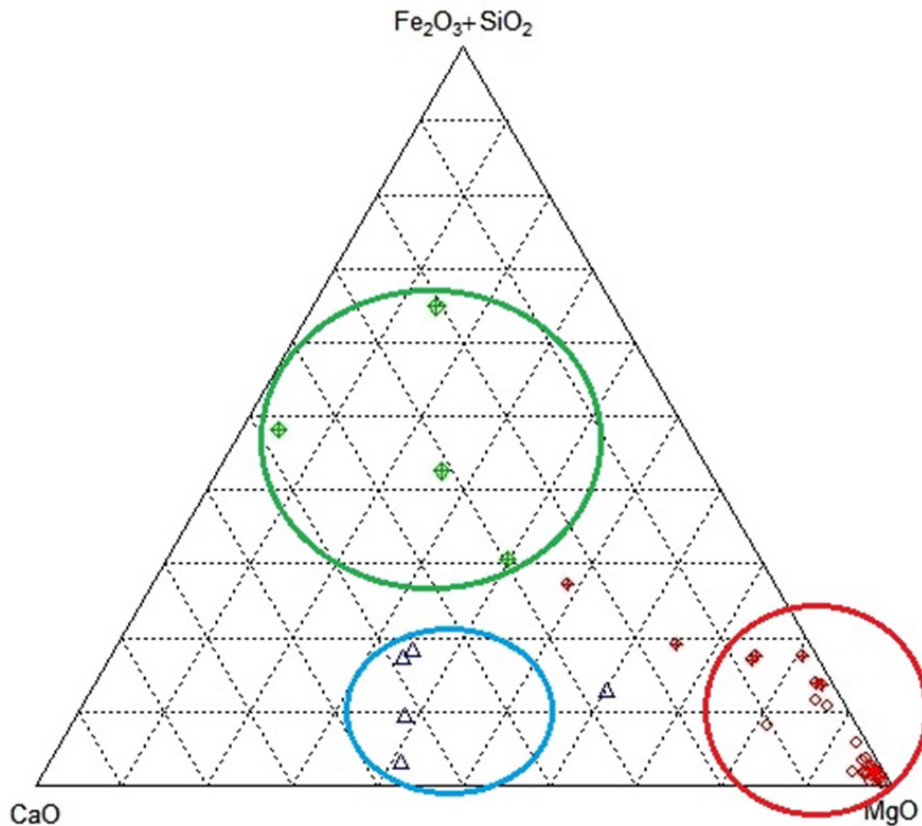


Figure 53: Total $\text{Fe}_2\text{O}_3+\text{SiO}_2$ -CaO-MgO ternary diagram for meta-carbonate rocks from the magnesite Aihai open pit (third section of the Dashiqiao Formation). Open red circles – magnesite ore, open red circle with cross – magnesitic marble with talc/Mg-chlorite, blue triangle – dolomitic marbles, green rectangle with cross – carbonaceous slates.

The binary diagram between MgO- Fe_2O_3 (Figure 54) of the bulk compositions of the magnesite ore samples and dolomitic marble samples (ICP-OES analyses) shows a negligible weak positive correlation ($r=0.19$). Maximum total iron content expressed as Fe_2O_3 is minimal lower in dolomitic marble host rocks than in magnesite ore (average difference is Fe_2O_3 0.2349 wt. %). Besides the Fe^{2+} ion preferably substituting for Mg^{2+} in the carbonates, other factors probably influence the Fe-distribution, including the availability of pyrite.

Magnesite can be divided into two sub domains with different Fe_2O_3 concentrations: low iron magnesite sub domain and high iron magnesite sub domain. The high iron magnesite sub domain is coincident with dark-grey halos in the magnesite ore body.

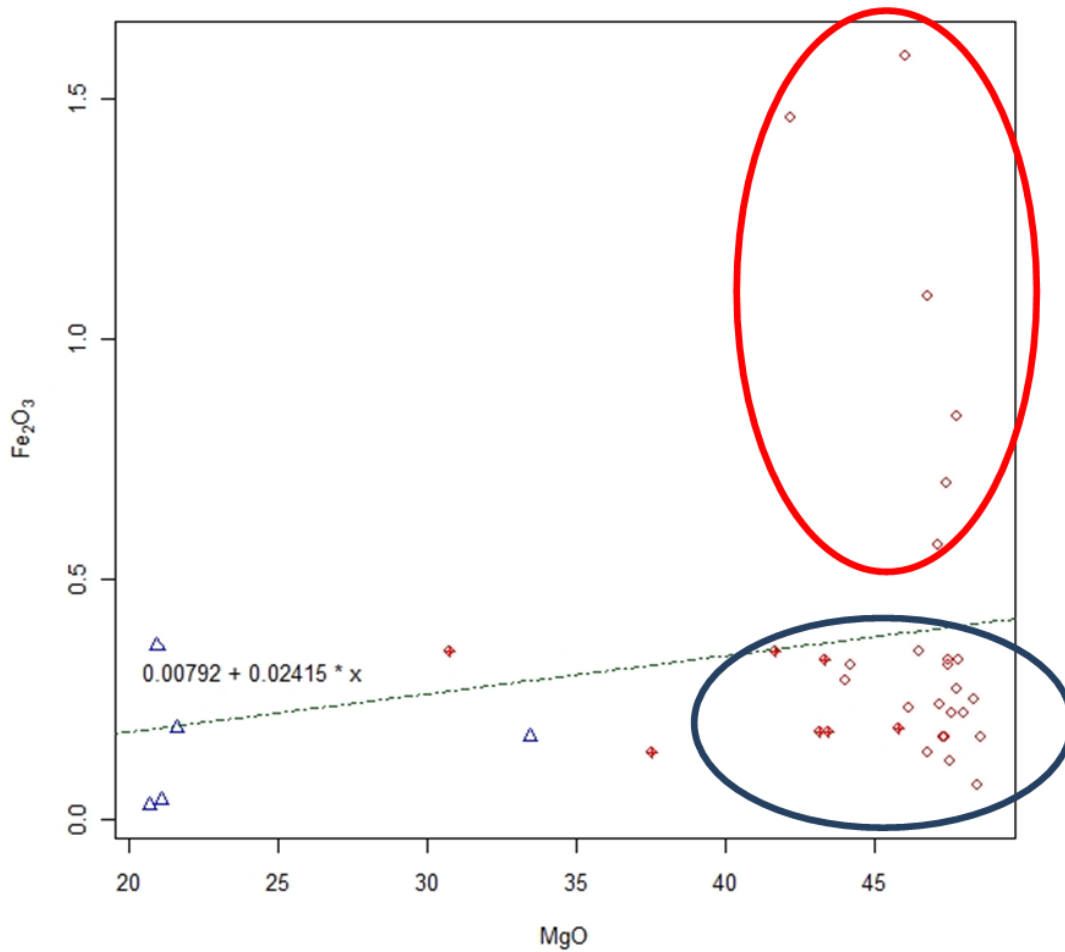


Figure 54: MgO-Fe₂O₃ variation diagram of dolomite host rocks and magnesite ore in the Aihai magnesite open pit. Open red circles – magnesite ore, open red circle with cross – magnesite marble with talc/Mg-chlorite, blue triangle – dolomite marbles. Red ellipsoid – high iron sub domain and blue ellipsoid – low iron sub domain.

Additional the ICP/OES whole rock analysis indicates a rather positive correlation ($r=0.97$) between Fe₂O₃ and MnO in the magnesite ore and the dolomitic marbles (Figure 55). Mn²⁺ with ionic radius of 0.81 Å can substitute for Mg²⁺ ($r=0.86$ Å) and/or Fe²⁺ ($r=0.92$ Å) in magnesite crystal.

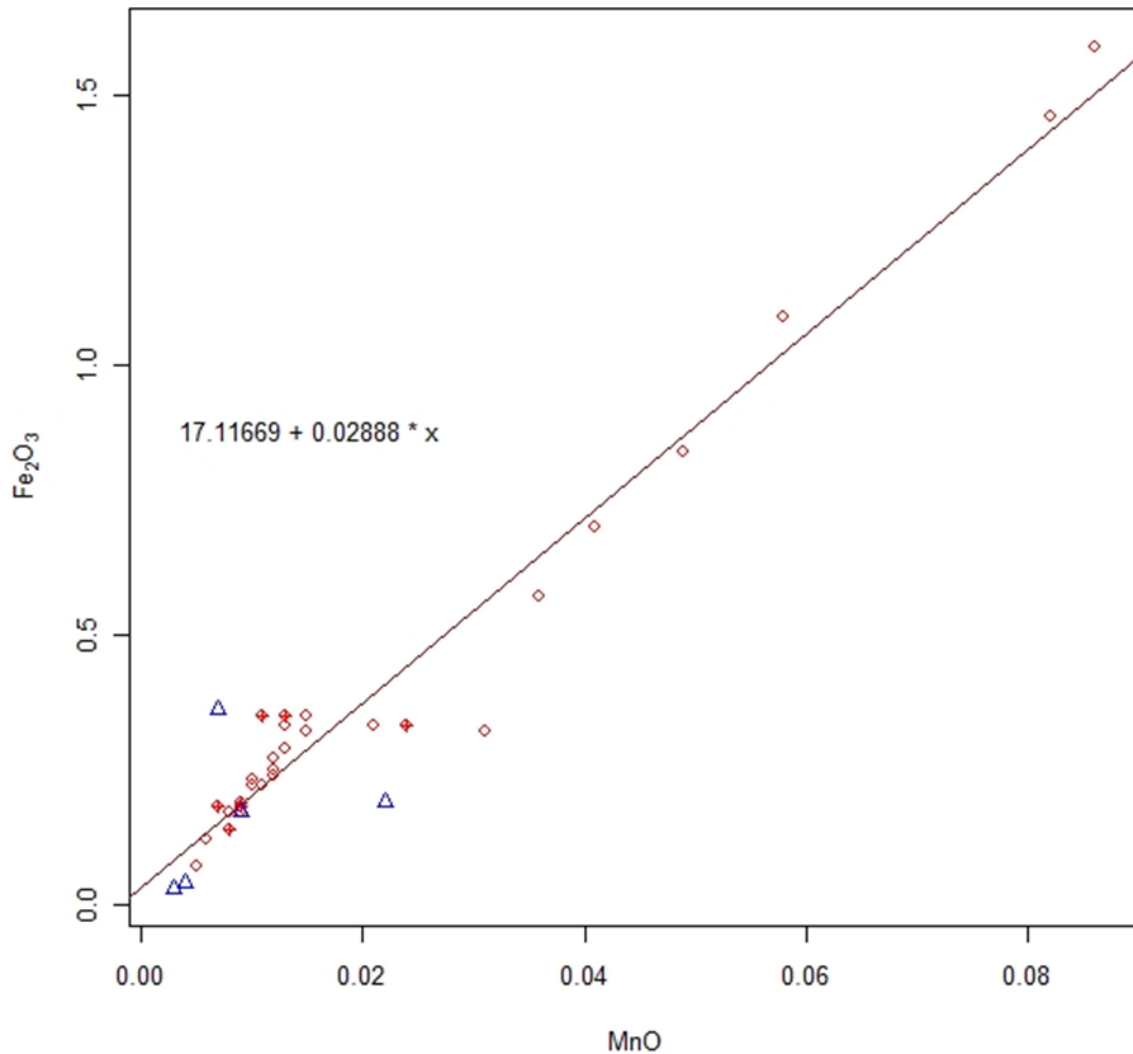


Figure 55: MnO-Fe₂O₃ variation diagram of dolomite host rocks and magnesite ore in the Aihai magnesite open pit. Open red circles – magnesite ore, open red circle with cross – magnesitic marble with talc/Mg-chlorite, blue triangle – dolomitic marbles.

According to bulk compositions of all magnesite and dolomite samples, the correlations between SiO₂, Al₂O₃, K₂O and TiO₂ are positive (Figure 56). Correlation coefficients are: $r=0.94$ for SiO₂-Al₂O₃, $r=0.30$ for SiO₂-K₂O, $r=0.91$ for SiO₂-TiO₂, $r=0.45$ for Al₂O₃-K₂O, $r=0.99$ for Al₂O₃-TiO₂ and $r=0.54$ for K₂O-TiO₂. The positive correlations reflect the detrital aluminosilicate fraction of the magnesite samples. SiO₂ as interstitial quartz grains or veinlet in magnesite is not always frequent, but magnesite samples show an average content of SiO₂ of about 3.0 %. A positive correlation between SiO₂ and Al₂O₃ indicates that most of the SiO₂ appears in talc and Mg-rich aluminosilicate (chlorite).

A positive correlation between $\text{SiO}_2\text{-TiO}_2$ and $\text{Al}_2\text{O}_3\text{-TiO}_2$ and petrographic composition indicate that rutile (TiO_2) is one of the main detrital heavy minerals which coexist with Mg-rich aluminosilicates (Mg-chlorite).

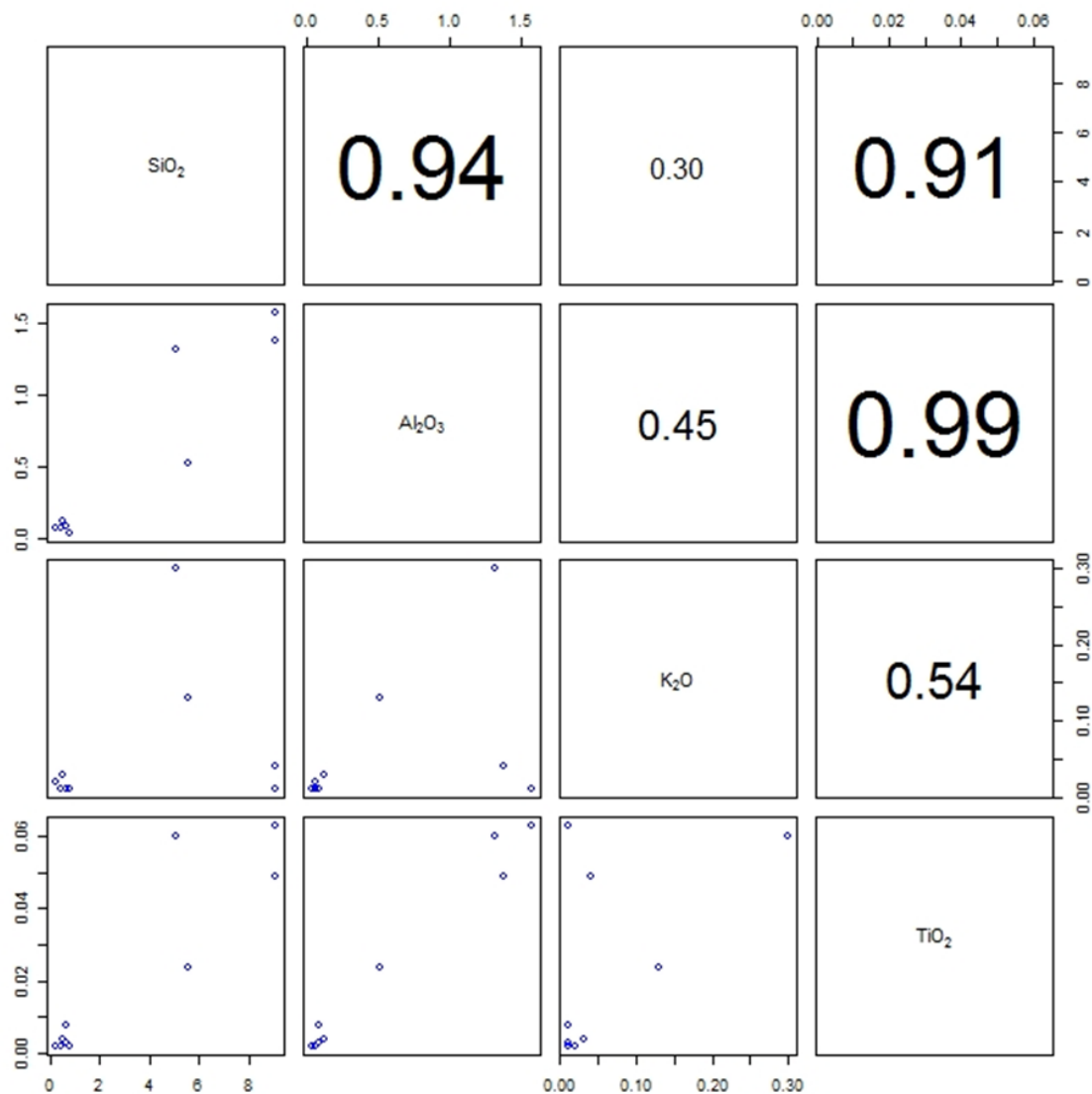


Figure 56: Variation diagrams and their correlation coefficients between SiO_2 , Al_2O_3 , K_2O and TiO_2 from all magnesite samples.

1.16 Trace Elements

The signatures of the trace elements of magnesite and related carbonate rocks have been considered. The signature of the trace elements provides an indication of the source from which Mg^{2+} ions have been derivated (Möller, 1989).

Ba occurs minimal in all magnesite samples (whole rock analyses) from 3 to 9ppm, except for sample 22-3 (Ba 17ppm). Half of the magnesite samples have Sr contents below the detection limit of 2 ppm. The Sr content in magnesite varies from 2 up to 59 ppm. MgO-Sr shows a positive correlation coefficient ($r=0.77$) and MgO-Ba has a negligible very weak positive correlation coefficient ($r=0.20$). The correlation coefficient from CaO-Sr is rather positive with $r=0.81$ and for CaO-Ba the correlation coefficient is nearly null. The dolomite samples (whole rock analyses) display Ba values from 4 to 11 ppm and the Sr value varies from 10 to 37 ppm. The Ba content in the magnesite and in the dolomite is similar. The average Sr concentration in dolomite is higher than in the magnesite samples, but do not reach the Sr peaks of the magnesite samples.

The positive correlation coefficients (MgO-Sr and MgO-Ba) from the magnesite samples are untypical, due to the fact that Sr and Ba ions will be constantly rejected during the magnesite crystallization and recrystallization, because they are too large and cannot enter the magnesite lattice (Ba 1.49 Å and Sr 1.32 Å), (Möller 1989). The ionic radii differences between large Sr and Ba ions and the smaller Mg and Fe ions cause the low Sr and Ba concentration. The relatively high Sr concentrations in some samples, with peaks up to 59 ppm, probably reflect dolomite inclusions and redolomitization of magnesite. The positive correlation coefficient (CaO-Sr) from the magnesite samples underpins the dolomite inclusion assumption.

Magnesite samples have an average zirconium content of 10.4 ppm, the highest zirconium peaks (43 ppm) occur in magnesite samples, which are associated with talc/Mg-chlorite. The average vanadium content is 7 ppm and 4.25 ppm of yttrium. Two thirds of the magnesite samples have vanadium and yttrium contents below the detection limit. Zr, Y, V, SiO₂ and Al₂O₃ display positive correlations. These elements can be associated with silicates (talc, Mg-chlorite, etc.).

The chromium and nickel content is below the detection limit of 20 ppm in all magnesite samples. The cobalt content varies from 1 ppm to 5 ppm in the magnesite samples.

1.17 Rare earth elements (REE)

Contents, fractionation and anomalies of rare earth elements (REE) in carbonates provide information about the composition of the fluids in the environment, where the minerals were formed, also about the chemical composition of the precursor of the magnesite and the way of crystallization. The REE patterns bears information on the physico-chemical environments a fluid experienced during mobilization, migration and mineralogenesis (Möller 1998, Bau & Möller 1992).

Precipitation of magnesite from hyper saline brine fluids is possible (Sayles & Fyfe, 1973). During evolution of such brines, almost all REE ions co-precipitate with the less soluble Ca-carbonate polymorphs, calcite being the first in the sequences of precipitates (Möller & Kubanek, 1976). During the later magnesite precipitation phase; the fluids are effectively void of lanthanides (first stage of sedimentary mineralization). If the second and third stage of mineralization (metasomatic transformation) is induced by hydrothermal fluids during diagenesis and metamorphism, REE may become considerably higher (Franz et al., 1979). In case of the magnesite samples from the Aihai magnesite open pit an enrichment of REE is not obvious. These phenomena maybe indicate that the attendant fluids, which caused different stages of mineralization, in the diagenesis event and the metamorphic event even not enriched in REE.

REE, however, analytically detected in magnesite because of small clayish detritus inclusions. The REE contents of host rocks of mica schists, dolomitic marbles, lamprophyre dykes, carbonaceous slates and the magnesite ore are listed in Table 2.

Sample ID	Group	La	Ce	Pr	Nd	Sm	Eu	Gd	Tb	Dy	Ho	Er	Tm	Yb	Lu
MG-Z	Magnesite	0,8	1,7	0,19	0,7	0,1	<	0,05	0,1	<	<	<	<	<	<
MG-S	Magnesite*	< 0,1	0,2	<	< 0,1	<	<	<	<	<	<	<	<	<	<
1-1	Magnesite	0,5	1,1	0,11	0,4	0,1	<	0,05	0,1	0,1	0,1	0,1	0,05	0,1	0,04
2-1	Magnesite**	0,5	1,3	0,15	0,6	0,1	<	0,05	0,1	0,1	0,1	0,1	0,05	0,1	0,04
3-1	Magnesite + Talc**	3,5	10,1	1,25	5	0,9	0,12	0,8	0,1	0,7	0,1	0,4	0,05	0,3	0,05
7-1	Magnesite +	1,8	4,5	0,49	1,9	0,4	<	0,4	<	0,5	0,1	0,4	0,06	0,4	0,06

	Talc						0,05		0,1							
8-1	Magnesite	0,9	2	0,22	0,8	0,1	<	0,05	0,2	0,1	0,2	0,1	0,2	0,05	0,1	0,04
8-3	Magnesite + Talc	2,6	6,6	0,76	3,2	0,6	<	0,08	0,6	0,1	0,6	0,1	0,4	0,06	0,4	0,05
8-8	Magnesite**	1,5	4,2	0,55	2,3	0,5	<	0,07	0,5	0,1	0,5	0,1	0,3	0,05	0,2	0,04
8-9	Magnesite	0,4	1,1	0,12	0,5	0,1	<	0,05	0,1	0,1	0,1	0,1	0,1	0,05	0,1	0,04
8-10	Magnesite **	1	2,6	0,32	1,3	0,3	<	0,07	0,3	0,1	0,3	0,1	0,2	0,05	0,2	0,04
11-1	Magnesite	0,8	1,9	0,23	0,9	0,1	<	0,05	0,1	0,1	0,1	0,1	0,1	0,05	0,1	0,04
11-2	Magnesite	0,9	2,4	0,28	1,1	0,2	<	0,05	0,2	0,1	0,2	0,1	0,1	0,05	0,1	0,04
13-1	Magnesite**	1,8	4,4	0,47	1,9	0,4	<	0,05	0,4	0,1	0,4	0,1	0,3	0,05	0,3	0,04
13-2	Magnesite*	0,2	0,5		0,2	0,1	<	0,05	0,1	0,1	0,1	0,1	0,1	0,05	0,1	0,04
15-1	Magnesite	0,8	1,7	0,18	0,6	0,1	<	0,05	0,1	0,1	0,1	0,1	0,1	0,05	0,1	0,04
15-2	Magnesite	0,7	2	0,22	0,8	0,2	<	0,05	0,2	0,1	0,1	0,1	0,1	0,05	0,1	0,04
16-1	Magnesite	0,4	0,8	0,1	0,4	0,1	<	0,05	0,1	0,1	0,1	0,1	0,1	0,05	0,1	0,04
16-2	Magnesite	0,3	0,7	0,08	0,3	0,1	<	0,05	0,1	0,1	0,1	0,1	0,1	0,05	0,1	0,04
16-3	Magnesite + Talc	0,7	1,6	0,17	0,7	0,1	<	0,05	0,1	0,1	0,1	0,1	0,1	0,05	0,1	0,04
18-1	Magnesite	0,5	1,1	0,1	0,4	0,1	<	0,05	0,1	0,1	0,1	0,1	0,1	0,05	0,1	0,04
19-1	Magnesite	< 0,1	0,2	0,05	< 0,1	0,1	<	0,05	0,1	0,1	0,1	0,1	0,1	0,05	0,1	0,04
19-2	Magnesite	< 0,1	0,2	0,05	< 0,1	0,1	<	0,05	0,1	0,1	0,1	0,1	0,1	0,05	0,1	0,04
18-2	Magnesite *	< 0,1	0,2	0,05	< 0,1	0,1	<	0,05	0,1	0,1	0,1	0,1	0,1	0,05	0,1	0,04
21-2	Magnesite + Tremolite	0,3	0,8	0,08	0,3	0,1	<	0,05	0,1	0,1	0,1	0,1	0,1	0,05	0,1	0,04
22-3	Magnesite + Talc	0,3	0,8	0,08	0,3	0,1	<	0,05	0,1	0,1	0,1	0,1	0,1	0,05	0,1	0,04
23-1	Magnesite	0,5	1,2	0,13	0,4	0,1	<	0,05	0,1	0,1	0,1	0,1	0,1	0,05	0,1	0,04
23-2	Magnesite + Talc	0,7	1,5	0,14	0,5	0,1	<	0,05	0,1	0,1	0,1	0,1	0,1	0,05	0,1	0,04
24-1	Magnesite	0,5	1,3	0,16	0,7	0,1	<	0,05	0,2	0,1	0,2	0,1	0,1	0,05	0,1	0,04
24-2	Magnesite	1	2,1	0,22	0,8	0,1	<	0,05	0,2	0,1	0,2	0,1	0,1	0,05	0,1	0,04
10-1	Dolomite	2,8	5,6	0,66	2,6	0,5	<	0,14	0,5	0,1	0,5	0,1	0,3	0,05	0,2	0,04
20-1	Dolomite	0,2	0,5	0,05	0,2	0,1	<	0,05	0,1	0,1	0,1	0,1	0,1	0,05	0,1	0,04
21-3	Dolomite	0,5	1,1	0,1	0,3	0,1	<	0,05	0,1	0,1	0,1	0,1	0,1	0,05	0,1	0,04
22-4	Dolomite	< 0,1	0,1	0,05	< 0,1	0,1	<	0,05	0,1	0,1	0,1	0,1	0,1	0,05	0,1	0,04
24-3	Dolomite	2,5	5,2	0,53	1,9	0,3	<	0,07	0,3	0,1	0,2	0,1	0,1	0,05	0,1	0,04

5-1	Carbonaceous Slate	21,1	42,1	4,51	16,5	3	0,44	2,6	0,4	2,1	0,4	1,2	0,19	1,3	0,22
6-1	Carbonaceous Slate	18,7	41,5	4,7	17,5	3,4	0,67	2,7	0,4	2,5	0,5	1,4	0,21	1,3	0,21
6-3	Carbonaceous Slate	11,1	23,3	2,55	9,3	1,8	0,4	1,6	0,2	1,4	0,3	0,8	0,12	0,8	0,13
14-1	Carbonaceous Slate	10,6	23,8	2,66	10,4	1,8	0,19	1,5	0,2	1,2	0,2	0,7	0,1	0,6	0,09
22-1	Dyke	10,9	23,6	2,83	13	3,5	1,29	3,8	0,6	3,4	0,6	1,6	0,22	1,4	0,21
22-2	Dyke	11,9	25,7	3,11	14,2	3,8	1,38	4	0,7	3,8	0,7	1,8	0,24	1,5	0,23
9-1	Mica-Schist	46,3	94	10,3	37,3	6,8	1,14	5	0,7	4	0,8	2,4	0,36	2,5	0,42
9-2	Mica-Schist + Calcite inclusions	21,1	41,1	4,81	19,4	3,9	0,97	3,7	0,6	3,5	0,7	2	0,27	1,6	0,24

Table 2: REE analyses (ppm) of host rocks and magnesite from the Aihai magnesite open pit; *younger magnesite precipitation in fissures (magnesium sinter); rock samples adjunct to faults.**

The REE distribution in magnesite and other carbonates is controlled by the grade of contamination of detrital material (aluminosilicates). This contamination is indicated by a positive correlation coefficient between Al_2O_3 and LREE (Parekh et al. 1977). Magnesite samples as well as dolomite samples display a positive correlation coefficient between Al_2O_3 and LREE (Figure 57).

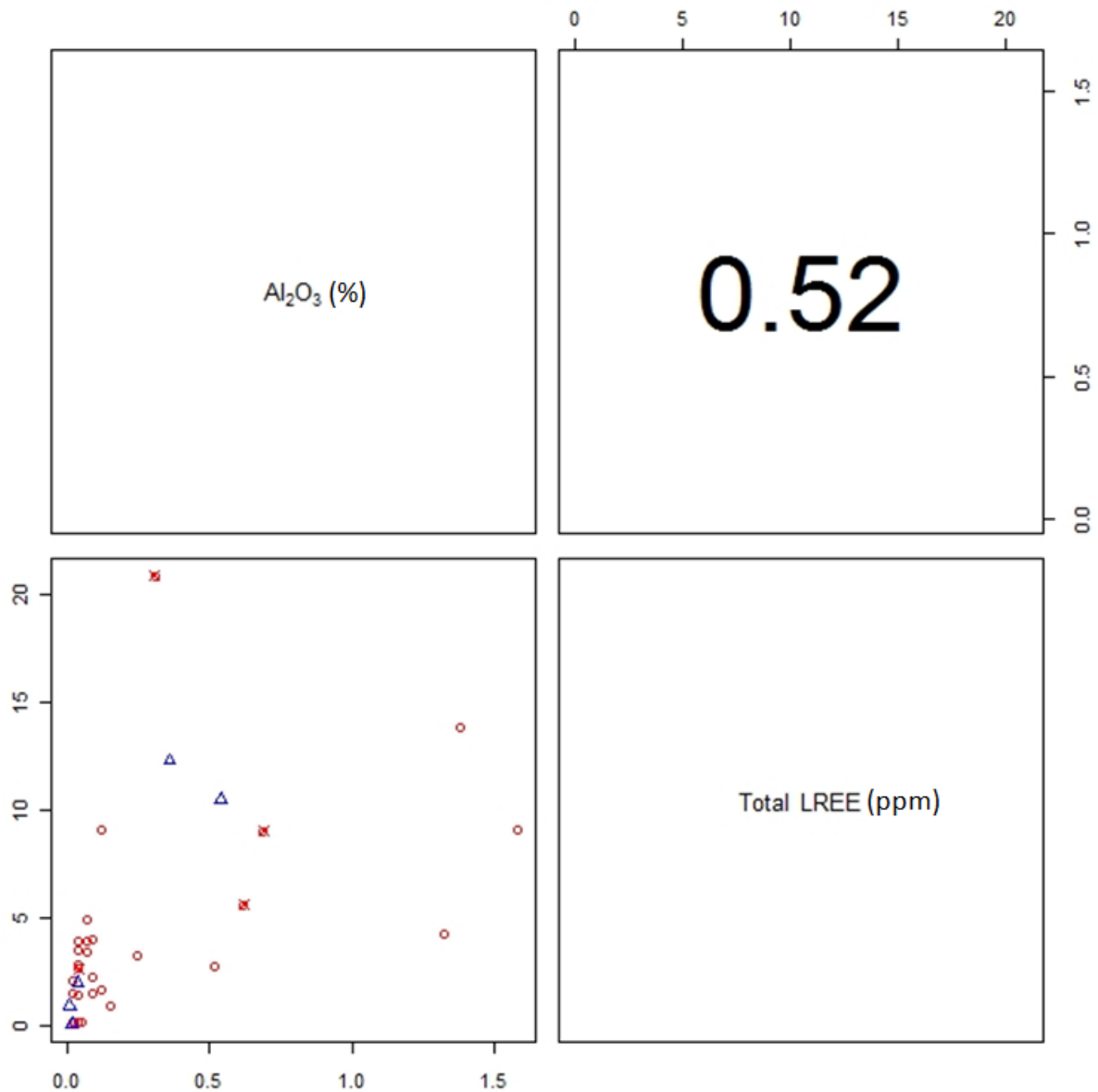
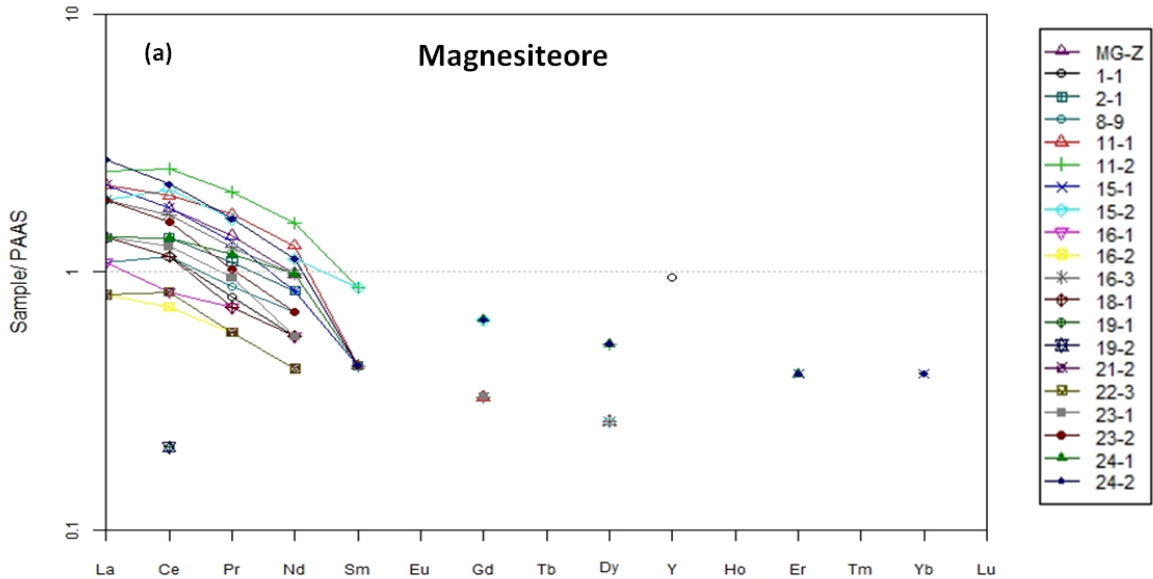


Figure 57: Positive correlation ($r = 0.52$) between the Al_2O_3 content and the total LREE content. Open red circles – magnesite ore, blue triangles – dolomitic marble.

The positive correlation is due basically to LREE, which are preferentially concentrated in clay minerals. Therefore, to avoid misleading interpretation, only magnesite samples without or with very low amounts of detrital aluminosilicates were considered in the interpretation of the REE geochemistry. The REE distribution patterns of the magnesite and dolomite samples are expected at or below the detection limits.

The magnesite samples show Σ REE from 0.2 to 5.28 ppm and the dolomitic marble samples from 0.1 to 2 ppm. The magnesite and dolomite samples display enrichment of LREE and depletion of HREE. Depletion of HREE in magnesite samples is reflected by high LREE/HREE ratios of magnesite and dolomite. The LREE/HREE ratios of magnesite samples are between 3 and 22.3 and the ratios of the dolomite samples between 7.68 and 15.

The REE + Y concentrations for all rock samples were normalized to the Post-Archean Australian Shale (PAAS) composite (Taylor & McLennan, 1985). The magnesite samples are divided into three groups: magnesite ore, magnesite ore adjunct to brittle faults and younger precipitations of magnesite in fissures. The PAAS-normalized REE+Y patterns are shown in Figures 58a, 58b and 58c. All magnesite samples show enrichment in LREE. Most of the magnesite ore samples, which are not affected by brittle faults, have HREE concentrations below the detection limit compared to the samples near brittle faults.



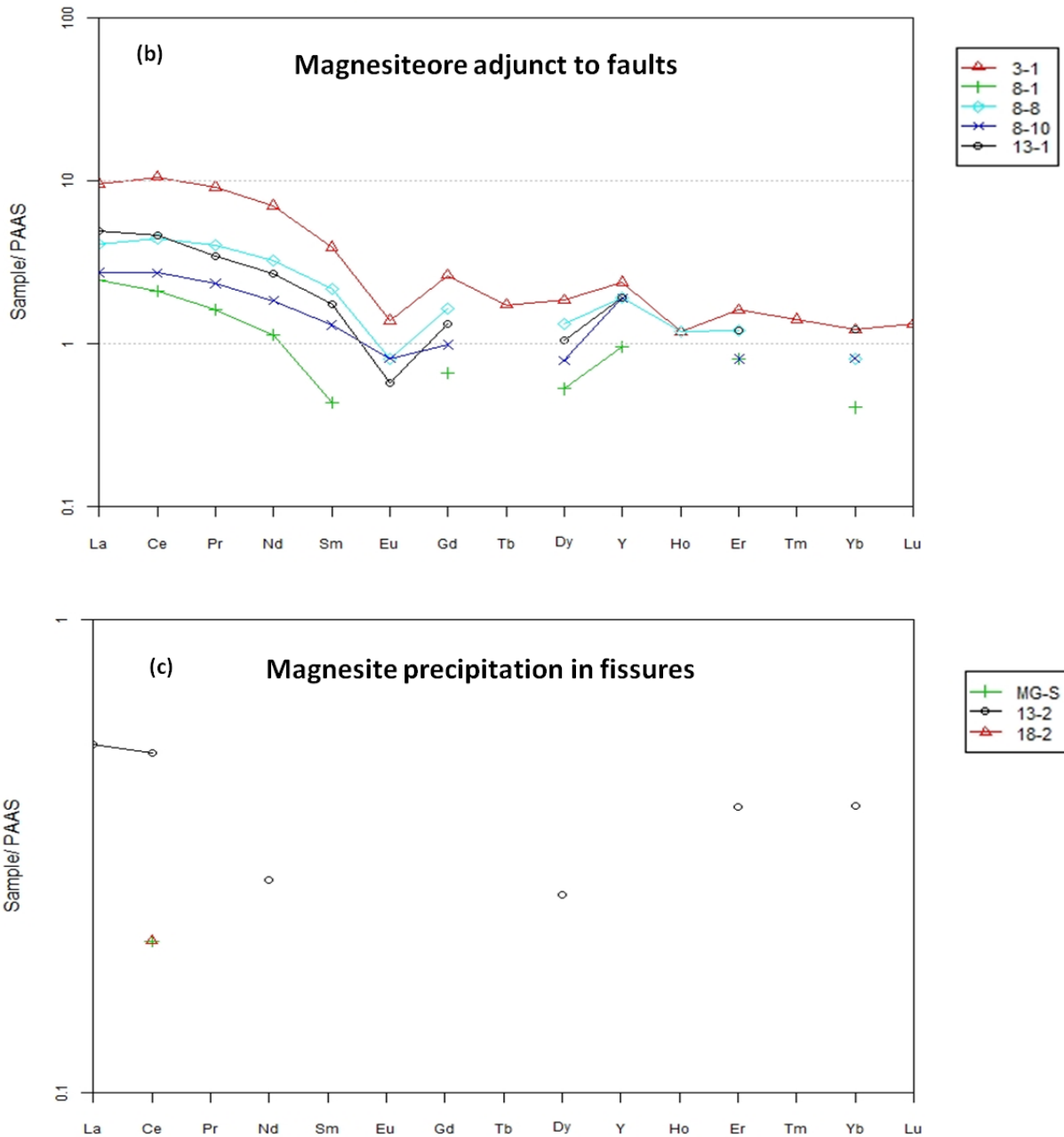


Figure 58: Shale normalized REE+Y patterns of the Dashiqiao Formation magnesite ore. (a) Almost uncontaminated magnesite ore. (b) Magnesite ore adjunct to brittle faults. (c) Magnesite ore precipitated in fissures.

The REE+Y distribution from the uncontaminated magnesite ore (Figure 58a) deviates, however, from PAAS by displaying a relative weak enrichment of LREE ($Nd_{SN}/Dy_{SN} = 1.07-4.82$) and have scattered Ce anomalies. It is impossible to make significant statements about the Eu anomalies, because all Eu contents are below the detection limit.

Five samples (Figure 58b) taken at the immediate contact to brittle faults show higher total REE contents and a distinct negative Eu anomaly compared to those samples taken from greater distance. These samples equally display a scatter Ce anomaly. A positive Y anomaly can be observed in all magnesite ore samples adjunct to brittle faults.

Magnesites (Figure 58c), which precipitated in open fissures, show no characteristic pattern. The total REE content is too low for qualitative interpretations.

The dolomitic rock samples PAAS normalized REE+Y contents display similar patterns as the magnesite ore (Figure 59). Sample 10-1 (located in the footwall of the deposit) and 24-3 (located in the hangingwall of the deposit) show enrichment in total REE. Both samples have a negative Eu anomaly and a positive Y anomaly.

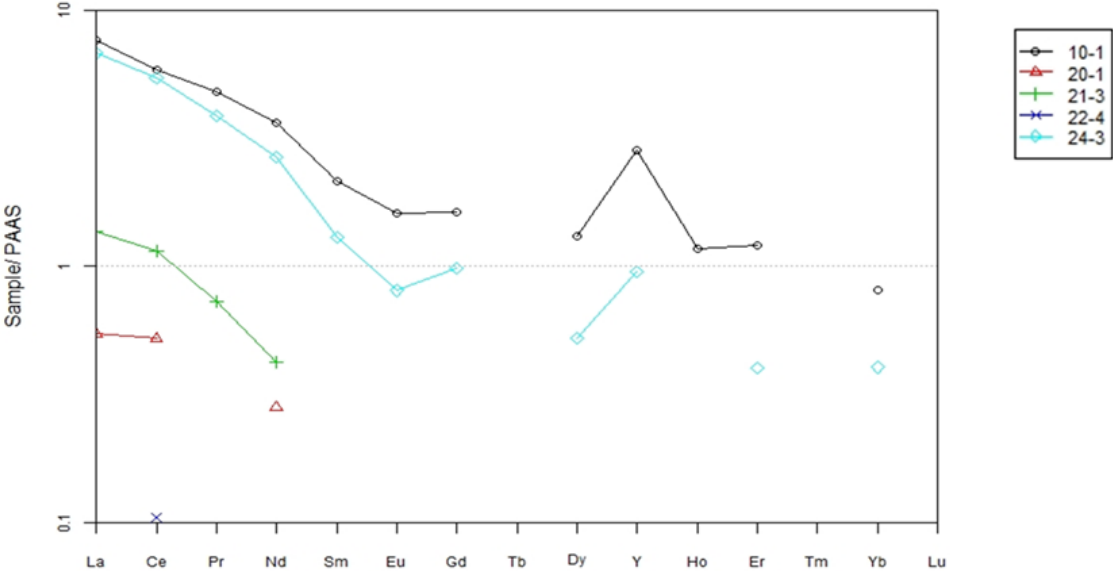


Figure 59: Shale normalized patterns of the dolomitic host rock.

The carbonaceous slates, which intercalate the ore body, have ΣREE from 53.8 to 96.09 ppm. All carbonaceous slates display enrichment in the LREE and depletion in HREE. The LREE/HREE ratios vary from 9.05 to 10.77. The characteristics of the patterns are dominated by a negative Eu anomaly and a weak positive Y anomaly (Figure 60).

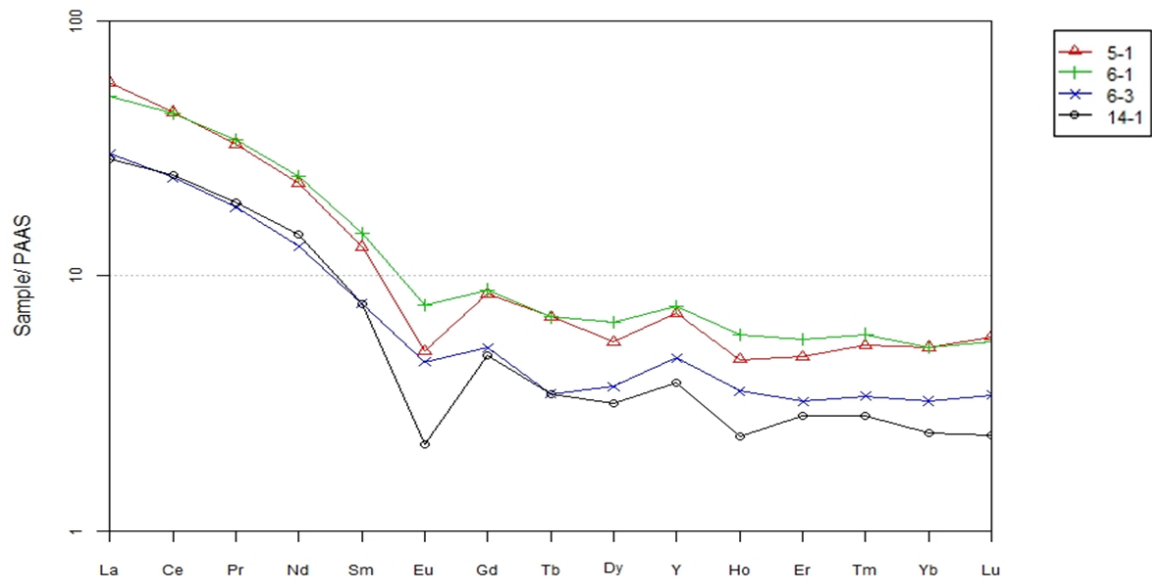


Figure 60: normalized patterns of the carbonaceous schists.

Micaschists with calcite inclusions in the footwall of the ore body show Σ REE from 103.89 to 212.02 ppm. The higher total REE value belongs to the pure mica schist without calcite inclusions. The micaschist host rock reveals higher Σ REE contents (Figure 61) than the carbonaceous slate, dolomitic marble and magnesite ore but all of them display relatively similar shale normalized patterns with negative Eu anomalies and positive Y anomalies.

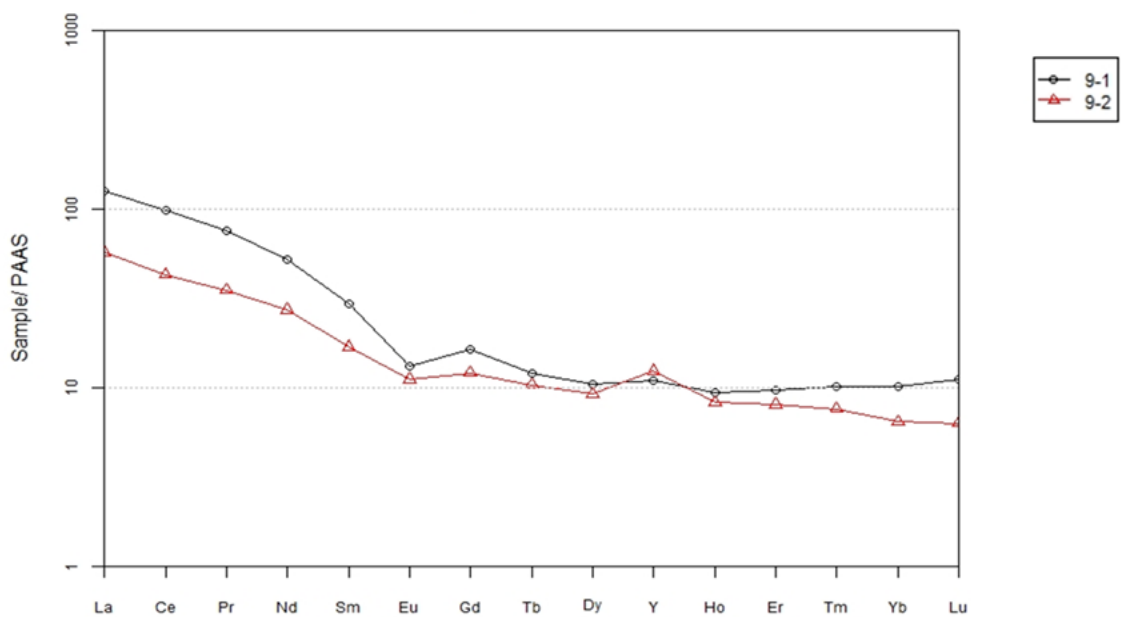


Figure 61: Shale normalized patterns of the micaschist (9-1) and the mica schist with calcite inclusions (9-2).

Most of the Dashiqiao meta-carbonates have atypical seawater-like REE+Y patterns. The atypical behavior of the patterns is characterized by depletion of HREE and abundance of LREE, and the incisive Ce anomalies. This atypical behavior can be explained by variable degrees of contamination during the precipitation from seawater. These contaminations would have suppressed the seawater signature. Variety of contaminants, such as *I*) shale contamination, which is one of the major input sources for marine LREE (Nothdurft et al., 2004), *II*) biogenic sedimentation from the overlying seawater (Murphy & Dymond, 1984), *III*) scavenging process related to depth, salinity and oxygen levels (Greaves et al. 1999), *IV*) authigenic removal of REE from the water column and early diagenesis (Sholkovitz, 1988).

Recently, Y is inserted between Ho and Dy in the REE pattern according to its identical charge and similar radius (REE+Y pattern; Bau, 1996). Thus similar geochemical behavior leads to the effect that Ho is removed from seawater twice fast as Y because of differences in the surface complexation behavior (Nozaki et al., 1997). This makes the Y/Ho ratio a particularly useful monitor for the differentiation between marine and non-marine deposits (Nothdurft et al., 2004). Seawater generally displays high Y/Ho ratios from 44 to 74, whereas terrigenous materials and volcanic ash have constant chondritic Y/Ho ratios of 28. The Y/Ho ratios are not constant, vary with depth and are strongly reliant on salinity (Lawrence et al., 2006). In the present study most of the Y and Ho contents of the meta-carbonates are below the detection limit. The few remaining meta-carbonate samples show an average Y/Ho ratio of around 56. The average Y/Ho ratio of the carbonaceous slates is 35.7, what indicate an influx of volcanic ash.

The meta-carbonates (magnesite, dolomite, carbonaceous slate) from the Aihai open-pit show no distinct negative or positive Ce anomaly. The Ce anomalies may be altered by diagenesis (Liu et al., 2006).

According to Komiya et al. (2008) the presence or absence of Ce anomalies in ancient marine authigenic sediments has the potential for establishing paleo-redox variations in ancient oceans. It is not surprising, that the negative Ce anomaly is absent in carbonates and banded iron formation (BIF) of Archean to earliest

Proterozoic age when seawater was not sufficiently oxidizing to form Ce^{IV} (Kamber & Webb, 2001).

The meta-carbonates of the Dashiqiao Formation display high MREE concentrations, which have a relatively distinct negative Eu anomaly. The negative anomaly of Eu is regarded as being characteristic of a reducing environment in which Eu^{3+} is reduced to Eu^{2+} although some authors have suggested that metamorphism or metasomatism could cause Eu reduction (e.g Fleet, 1984). Regarding Parente et al. 2004, a negative Eu anomaly and absence of a negative Ce anomaly may indicate that the studied magnesian carbonate sequence was developed in a paralic marine environment, platformal with euxinic influence.

1.18 Stable isotope geochemistry

The comparative study of the isotopic-geochemical properties of sparry magnesites and of carbonate-hosts can help to elucidate the genesis of sparry magnesite (Kralik et al. 1989). The source of magnesium, the time and mechanism of magnesite formation is still a matter of controversy of researchers. Stable isotopes of carbon (C) and oxygen (O) of carbonate rocks of the Aihai deposit were analyzed to gain fundamental information of the source of O and C in the mineralizing fluids, of the mixing of fluids, secondary processes, biogenic activity and of the temperature range of the mineralizing fluids (Schroll 2002). C isotopes are important markers for determining the source of C. O isotope data of the carbonates provide indications of the isotopic signature of the mineralizing water and the magnesite precipitation temperature.

The C isotope signature of magnesites provide indications on the C isotopic composition seawater and marine carbonate rocks, the thermal decomposition of carbonates (+/- organic matter), anaerobic decomposition of organic matter, evaporation, microbial fermentation processes, CO_2 produced by metamorphic and magmatic processes or hybrid of each above and other ore forming processes (Schroll 2002).

Although many stable isotope data of globally distributed Neoproterozoic carbonates are available relatively fewer data exist for Paleoproterozoic carbonates (Ray et al. 2003).

Stable C and O isotope data of the third section of the Dashiqiao Formation carbonates are available in the recent literatures (Chen et al. 2003; Jiang 1987; Jiang et al. 2004; Tang et al. 2009). There C and O isotopic compositions of host rock marbles and magnesites of different ore districts in eastern Liaoning are given. These C and O isotopes are compiled in Table 3 and Figure 62.

Sample ID	Lithology	$\delta_{13}\text{C}_{\text{PDB}}(\text{‰})$	$\delta_{18}\text{O}_{\text{SMOW}}(\text{‰})$	data source
DSQ2	marble	-0,6	17,3	Jiang et al., 2004
DSQ6-1	marble	1	18,5	Jiang et al., 2004
DSQ11	marble	0,1	12,6	Jiang et al., 2004
DSQ19-2a	marble	-1,9	16,3	Jiang et al., 2004
M-1	marble	-0,6	15,5	Jiang, 1987
L01015	marble	-1,8	22,8	Chen et al., 2003
L01025	marble	-4,5	19,6	Chen et al., 2003
L01017	marble	-0,5	20,2	Chen et al., 2003
L01020	marble	4,4	18,2	Chen et al., 2003
L01023	marble	-0,8	12,1	Chen et al., 2003
L01021	marble	0,8	11,2	Chen et al., 2003
DSQ14	magnesite	0,4	11,1	Jiang et al., 2004
DSQ15	magnesite	-0,4	13,8	Jiang et al., 2004
HYZ6-1	magnesite	1,2	9,6	Jiang et al., 2004
M-2	magnesite	-1,3	11,7	Jiang, 1987
M-3	magnesite	-0,6	11,1	Jiang, 1987
L01035	magnesite	-1,4	11,1	Chen et al., 2003
L01022	magnesite	1,2	12,6	Chen et al., 2003
DSQ19-1	magnesite vein	0,3	5,2	Jiang et al., 2004
DSQ19-2b	magnesite vein	0,2	8	Jiang et al., 2004
M-4	calcite vein	1,3	16,9	Jiang, 1987
LD001	dolomite	-2,6	14,1	Tang et al., 2009
LD006	magnesite	-2,7	16,2	Tang et al., 2009
LD002	magnesite	0,1	12,7	Tang et al., 2009
LD003	magnesite	0,6	12,5	Tang et al., 2009
LD004	magnesite marble	0,5	10,3	Tang et al., 2009
LD005	magnesite marble	0,3	9,2	Tang et al., 2009
LD007	magnesite marble	0,4	10,1	Tang et al., 2009
LD008	magnesite marble	0,2	10,4	Tang et al., 2009
LD009	dolomite	1,2	17,4	Tang et al., 2009

LD010	dolomite	1,4	18,7	Tang et al., 2009
LD011	dolomite	1,4	19,5	Tang et al., 2009
LD012	dolomite	1,4	19,1	Tang et al., 2009
LD013	dolomite	0,6	18	Tang et al., 2009
LD014	dolomite	1,2	16,4	Tang et al., 2009

Table 3: C and O isotope data of host rocks and magnesite ores of the eastern Liaoning province.

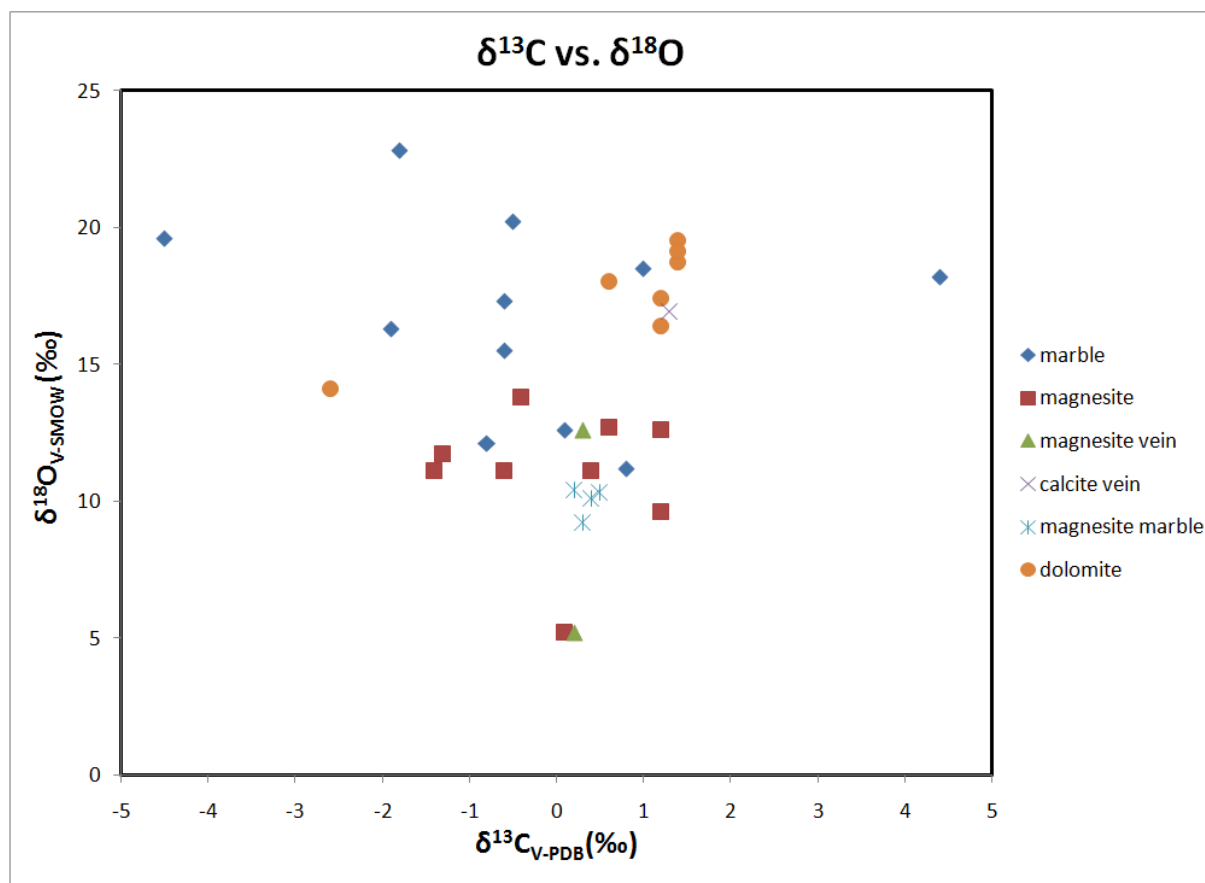


Figure 62: C and O isotope data of host rock marbles and magnesites from the magnesite deposits in eastern Liaoning province.

The published C and O isotopic data indicate a marine source of the magnesites and the marbles' protoliths (Keith et al. 1964). The $\delta^{13}\text{C}_{\text{PDB}}$ of marbles vary from -4.5‰ to $+4.4\text{‰}$ with an average value close to zero; the $\delta^{13}\text{C}_{\text{PDB}}$ of magnesite varies from -2.7‰ to $+1.2\text{‰}$ with average values close to zero too. The $\delta^{18}\text{O}_{\text{SMOW}}$ of marbles from the eastern Liaoning province vary from $+11.2\text{‰}$ to $+22.8\text{‰}$; whereas the $\delta^{18}\text{O}_{\text{SMOW}}$ of magnesites show generally lower $\delta^{18}\text{O}_{\text{SMOW}}$ values of $+9.6\text{‰}$ to $+16.2\text{‰}$. The

dolomite samples display $\delta^{13}\text{C}_{\text{PDB}}$ values between +0.6‰ and +1.4‰, and $\delta^{18}\text{O}_{\text{SMOW}}$ values from 16.4‰ to 19.5‰, respectively.

$\delta^{13}\text{C}$ and $\delta^{18}\text{O}$ isotope ratios of selected carbonates deriving from the Aihai magnesite open pit were determined at the Fritz Ebner Stable Isotope Laboratory at the University of Leoben. The isotopic measurements were conducted on a Thermo Fisher Delta V mass spectrometer with a Finnigan Gas Bench II following the operation guidelines of Spötl and Vennemann (2003). Carbon isotope data and oxygen isotopes are reported relative to Vienna Pee Dee Belemnite (VPDB) and Vienna Standard Mean Ocean Water (VSMOW). By using multiple measurements of an in-house calcite standard, a precision and accuracy of <0.07‰ of the isotope measurements were calculated.

In total 39 rock samples from the Aihai open pit were used for $\delta^{13}\text{C}$ and $\delta^{18}\text{O}$ isotope determination. The rock samples were split considering color (bright to dark), grain size differences, micro joints and relic-like fragments.

The sub-samples show different ^{13}C and ^{18}O isotope ratios indicating the presence of different magnesite generations. Overall 78 sub-samples were analyzed; the C and O isotopes are listed in Table 4 and illustrated in Figure 63.

Additionally the clustering method Mclust (Fraley & Raftery, 2007) was applied to the data for classification. An optimum cluster number for Mclust clustering is determined by the algorithm based on the highest BIC (Bayesian Information Criterion) value. Like many other multivariate statistical methods, cluster analysis helps to obtain an overview of data sets of many observations and variables. It can be used for both, structuring the variables and grouping the observations (Fraley & Raftery, 2007).

Sample ID	Lithology	$\delta^{13}\text{C}$ VPDB (‰)	$\delta^{18}\text{O}$ VSMOW (‰)	Group ID
MG-Z-a	magnesite	0,5	10,4	1
MG-Z-b	magnesite	0,4	10,1	1
MG-Z-c	magnesite	0,4	10,2	1
MG-S-a	magnesite sinter	0,1	10,6	1
MG-S-b	magnesite sinter	0,3	10,3	1
MG-S-c	magnesite sinter	-3,2	11,2	2

1-1-a	magnesite	-0,4	13,0	3
1-1-b	magnesite	-0,8	13,6	3
1-1-c	magnesite	-3,3	14,0	2
2-1-a	magnesite	-2,0	15,3	2
2-1-b	magnesite	-2,1	15,2	2
3-1-a	magnesite + talc	-0,5	12,8	3
3-1-b	magnesite + talc	-0,5	12,5	3
3-1-c	magnesite + talc	-0,3	10,6	3
5-1-a	carbonaceous schist	-1,4	16,6	2
5-1-b	carbonaceous schist	-1,2	14,1	2
7-1-a	magnesite + talc	0,8	11,2	1
7-1-b	magnesite + talc	0,6	11,0	1
7-1-c	magnesite + talc	0,7	11,0	1
8-1-a	magnesite	0,6	11,0	1
8-1-b	magnesite	-2,4	13,5	2
8-3-a	magnesite + talc	0,5	9,9	1
8-3-b	magnesite + talc	0,4	10,5	1
8-3-c	magnesite + talc	0,1	11,0	1
8-4-a	magnesite	0,0	9,7	1
8-4-b	magnesite	0,3	9,5	1
8-8-a	magnesite	0,8	10,1	1
8-8-b	magnesite	0,8	9,9	1
8-8-c	Magnesite	0,7	10,3	1
8-9-a	magnesite + talc	-0,4	13,0	3
8-10-a	magnesite	-3,7	13,6	2
8-10-b	magnesite	-3,6	14,0	2
10-1-a	dolomite	1,0	11,7	3
10-1-b	dolomite	1,0	11,8	3
11-1-a	magnesite	0,9	10,6	1
11-1-b	magnesite	1,0	10,5	1
11-2-a	magnesite	0,9	10,7	1
11-2-b	magnesite	0,1	11,2	1
13-1-a	magnesite	0,5	11,5	3
13-1-b	magnesite	0,5	11,5	1
13-1-c	magnesite	0,6	11,6	3
13-2a	magnesite vein	-2,9	13,0	2
13-2b	magnesite vein	-2,5	11,8	2
15-1-a	magnesite	0,5	10,5	1
15-1-b	magnesite	0,5	10,6	1
15-2-a	magnesite	0,5	10,9	1
16-1-a	magnesite	0,9	10,1	1
16-2-a	magnesite	0,7	10,6	1
16-2-b	magnesite	1,0	10,0	1
16-3-a	magnesite + talc	0,5	9,9	1
16-3-b	magnesite + talc	0,7	10,1	1

18-1-a	magnesite	0,5	10,5	1
19-1-a	magnesite	-0,4	12,6	3
19-2-a	magnesite	0,0	12,4	3
19-2-b	magnesite	0,1	12,7	3
18-2-a	magnesite sinter	-3,7	12,3	2
18-2-b	magnesite sinter	-2,1	11,5	2
18-2-c	magnesite sinter	-2,3	10,9	2
20-1-a	dolomite	1,7	19,9	4
20-1-b	dolomite	1,4	18,4	4
21-2-a	magnesite + tremolite	1,3	15,2	3
21-2-b	magnesite + tremolite	1,4	13,0	3
21-3-a	dolomite	1,6	13,5	3
21-3-b	dolomite	1,6	12,9	3
22-3-a	magnesite + talc	1,3	11,2	3
22-3-b	magnesite + talc	1,6	10,5	3
22-4-a	dolomite	1,6	13,7	3
22-4-b	dolomite	1,0	13,9	3
23-2-a	magnesite + talc	1,6	12,1	3
23-2-b	magnesite + talc	0,4	13,5	3
24-1-a	magnesite	-0,7	13,7	3
24-1-b	magnesite	0,9	11,2	1
24-2	magnesite	0,1	12,6	3
24-3-a	dolomite	-0,6	11,6	3
24-3-b	dolomite	1,3	20,6	4
24-3-c	dolomite	1,2	20,5	4
23-1-a	magnesite	1,9	10,7	3
Calc. Incl.	Calcite vein	-3,9	12,0	2

Table 4: C and O isotope data of selected carbonates from the Aihai magnesite open pit. The group ID represents the Mclust cluster.

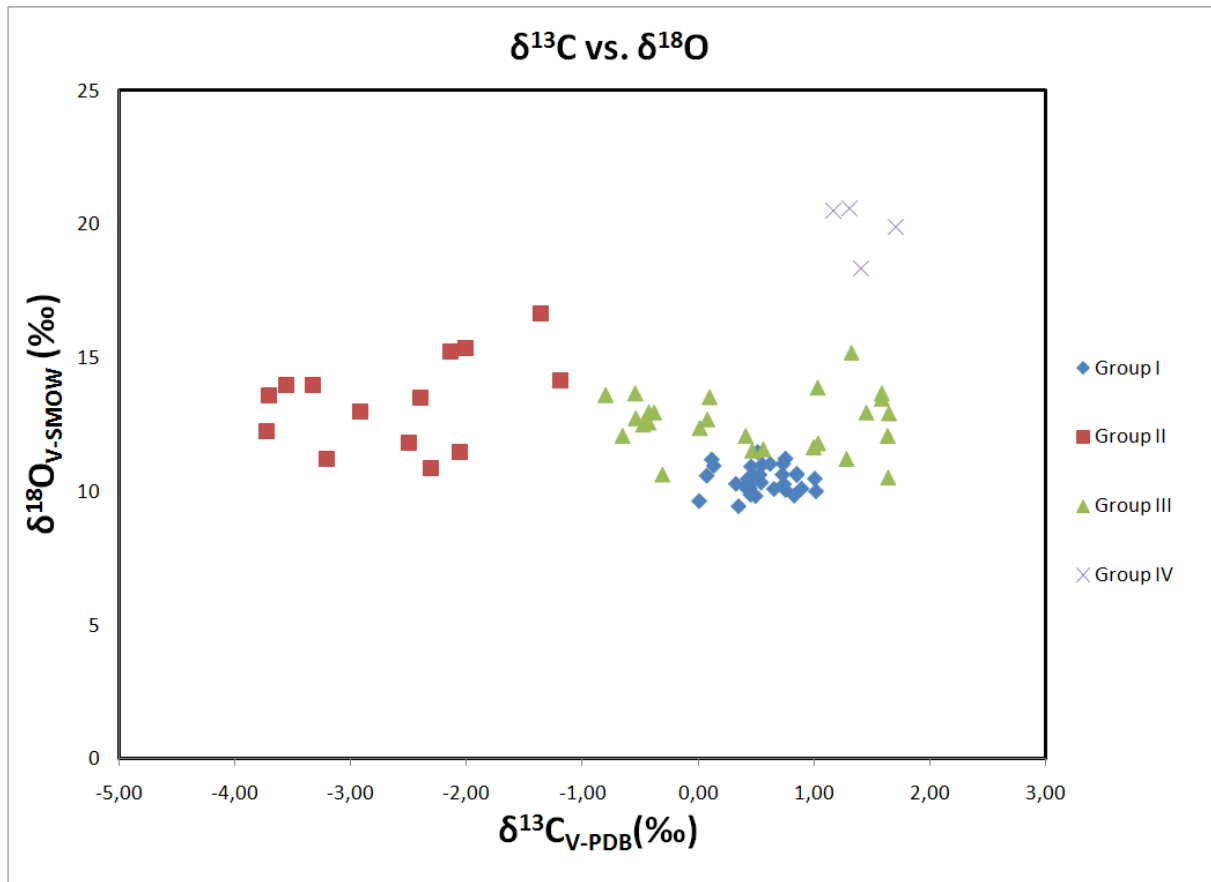


Figure 63: C and O isotope variations of selected carbonates from the Aihai magnesite open pit. The groups represent the Mclust cluster.

The Mclust result shows four different groups which are congruent with the field observations. The supposed variety features like color and grain size show subordinate influence on the stable isotope variation, contrary to micro joints and relic-like fragments. Group I is composed of massive magnesite with dark grey halos and small scale talc bearing shear zones. Group II represents the material in young brittle shear zones, i.e. mostly magnesite sinter and magnesite veins. Group III displays the upper part of the magnesite ore. This part is interbedded with dolomite layers and related to a big shear zone. Group IV comprises thinly banded dolomite of the hanging wall of the deposit. In summary, the hanging wall dolomites have $\delta^{13}\text{C}_{\text{PDB}}$ ratios ranging from +1.16‰ to +1.71‰ and $\delta^{18}\text{O}_{\text{SMOW}}$ values between +18.37‰ and +20.59‰. The magnesite sinter and veins yield $\delta^{13}\text{C}_{\text{PDB}}$ and $\delta^{18}\text{O}_{\text{SMOW}}$ compositions of -3.93‰ up to -1.37‰. The dolomitic interbedded magnesite ore displays $\delta^{13}\text{C}_{\text{PDB}}$ values from -0.81‰ to 1.88‰ and $\delta^{18}\text{O}_{\text{SMOW}}$ values from 10.53‰ to 15.21‰. The

massive magnesite ore part is marked by $\delta^{13}\text{C}_{\text{PDB}}$ values from 0.01‰ to 1.02‰. $\delta^{18}\text{O}_{\text{SMOW}}$ is ranging from 9.47‰ to 11.24‰.

Hudson (1977) ascertained that O isotopes can be a sensitive indicator of diagenetic alteration. The progress of diagenesis generally decreases $\delta^{18}\text{O}$, and the consequence of diagenesis can be revealed on a $\delta^{13}\text{C}$ and $\delta^{18}\text{O}$ cross-plot. O isotopes are normally affected by exchangeable oxygen originated from either meteoric water or interstitial fluids at elevated temperature (Fairchild et al., 1997), whereas $\delta^{13}\text{C}$ may be cushioned by the pre-existing carbonate. Generally speaking, decrease of O and C isotope values may be remarkable during late diagenesis as well as the consequence of low grade metamorphism and additional deformation (Guerrera et al., 1997).

Although the cross plot in Figure 63 shows no hint for a correlation, the range in $\delta^{18}\text{O}$ is obvious and maybe reflects the reset of O isotopes during later recrystallization. The smaller range of $\delta^{13}\text{C}$ values suggests that C isotopes might have been buffered by pre-existing carbonate.

Processes leading enhanced Mg/Ca ratios in fluid, and elevated temperatures, should leave characteristic fingerprints on the isotopic composition of magnesites. Data summarized in the cross-plot (Figure 64) suggest that, in conjunction, $\delta^{18}\text{O}$ and $\delta^{13}\text{C}$ could offer an important tool for distinguishing between different genetic types of magnesites. Thus fine grained magnesites, deposited in modern sabkha and playa environments, exhibit highly positive $\delta^{18}\text{O}$ values as evaporation leads to marked ^{18}O enrichments (Lloyd, 1966). Cryptocrystalline magnesites associated with ultramafic rocks and serpentinites show marked ^{13}C depletions, reflecting the isotopic composition of CO_2 derived from metamorphic reactions at depth (O'Neil & Barnes, 1971). Massive spar magnesite deposits are conspicuously depleted in ^{18}O compared to other magnesite types (Figure 64), but are indistinguishable from recent magnesites on $\delta^{13}\text{C}$ grounds. The isotopic composition of the Aihai open pit magnesites coincide with the modal isotopic values of major spar magnesite deposits like Rum Jungle (Australia), Eugui (Spain) and Radenthein (Austria).

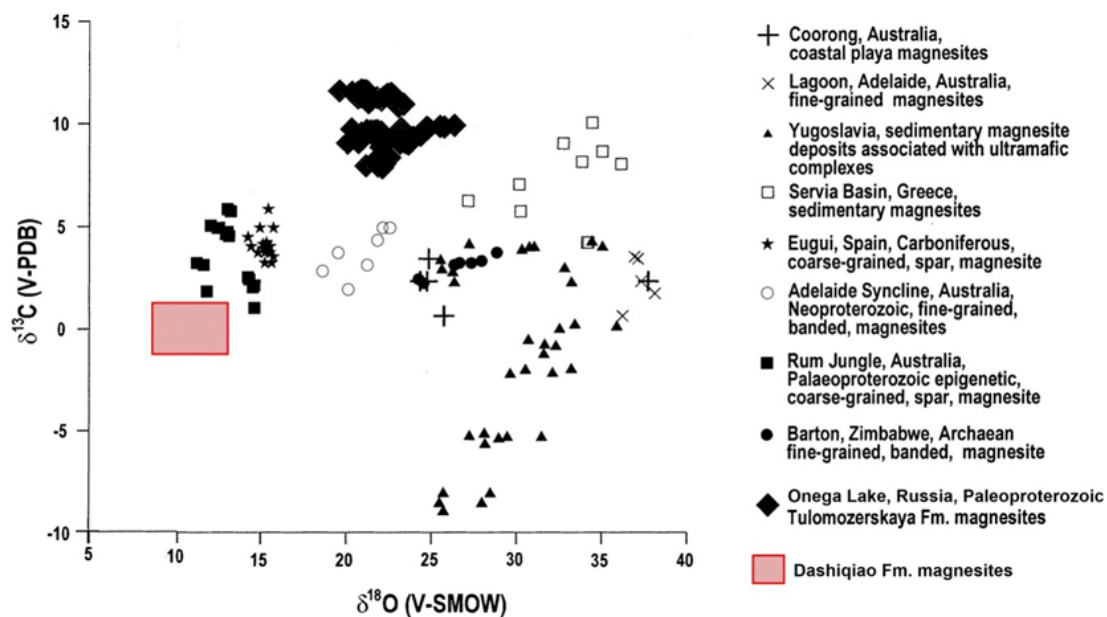


Figure 64: Plot of $\delta^{13}\text{C}$ vs. $\delta^{18}\text{O}$ comparing the Dashiqiao Formation results with magnesites from other deposits. Data are from: Coorong Lagoon, South Australia (Zachmann, 1989); Lagoon, Adelaide, South Australia (Botz & von der Borch, 1984); magnesite deposits of Yugoslavia (Fallick et al., 1991); Serbia sedimentary magnesites (Kralik et al., 1989); Eugui, Spain, Carboniferous, coarse-grained, spar magnesite (Kralik & Hoefs, 1978); Adelaide Syncline, Copper Claim, Australia, Neoproterozoic, fine-grained, banded magnesite (Lambert et al., 1984); Rum Jungle, Northern Territory, Australia, Paleoproterozoic, coarse-grained, spar magnesite (Aharon, 1988); Barton, Zimbabwe, Archaean, fine-grained, banded magnesite (Perry & Tan, 1972).

Magnetite 3D deposit model

Information technology has changed the way of mining and the geological data visualization. Application of information technology in mining is represented in the processing and data management, using software packages for 3D design, modeling and integration of spatial databases with application of the results. In contemporary practice the application of mining computer program is significantly expanded and it can be concluded that the computer aided design has become a common way of developing mining projects. Mining software enables faster and more creative work. Mining software applications allowed development of new methods for open pit designing, which is significantly different from traditional methods (Miladinovic et al., 2011). The main differences between traditional and modern methods of design are given in Table 5.

Traditional methods	Modern methods
<ul style="list-style-type: none"> - manual processing of data, - long time for data processing, - starting point is geological determined ore body or deposit, - application of geometrical analysis, - analysis of the stripping ratio, - high costs of project, - small investments, - obtain approximate results of processing, - allow only 2D. 	<ul style="list-style-type: none"> - computer-supported data processing, - significantly shorter period of time for data processing, - starts with the development of computer models of the ore body (dividing it in to the blocks), - blocks analysis based on the optimal mining sequence, - low cost of project, but require greater investments in computer equipment and computer programs, - obtaining accurate data processing, - enable 2D and 3D display of all objects.

Table 5: Comparative review of methods of design and modeling in mining and geology (Miladinovic et al., 2011).

Generally, current methods have far greater advantages over the traditional, and in the future they will be more and more applied.

1.19 Gemcom Surpac

The software package Gemcom is designed for geological interpretation and modeling of unstratified deposits and the design of surface and underground mining of metal and nonmetals.

Surpac is a computer program widely used in the global mining practice. It is used for the design solutions of surface and underground exploitation, with the presentation of exploration works. To work in the program it is necessary to create a database and update it during the unfolding of the process of exploitation. Input data from the database are used to generate computational models in 2D or 3D (Figure 65). Surpac contains tools for data management, geostatistics, modeling, analyzing computer model, defining the quantity and quality of deposits, planning of the ore body exploitation by using different types of computer models, production control and automation of certain processes of exploitation (<http://www.gemcomsoftware.com>).

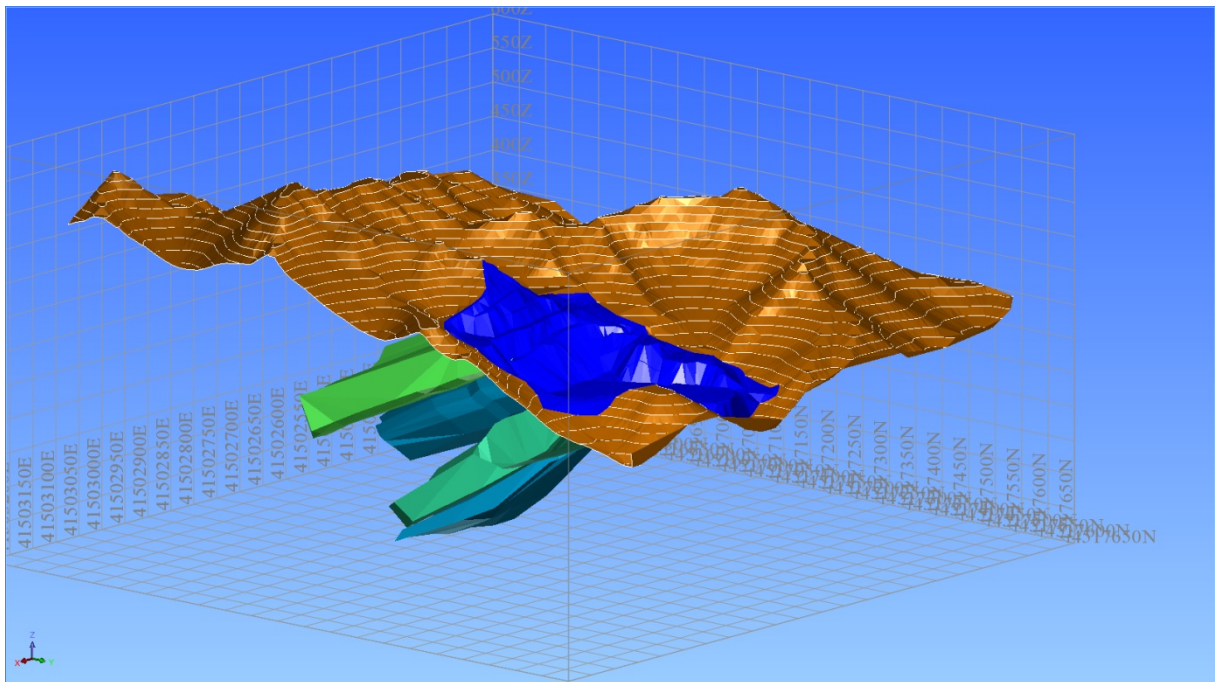


Figure 65: 3D computer model of the Aihai magnesite deposit. View to the SW.

1.20 Modeling of the magnesite deposit

Based on the limited borehole information available from the No. 4 Exploration team of Liaoning Geological Survey Bureau, a geological database based on borehole location has been created to model the magnesite deposit. Figure 66 shows all boreholes present in the area based on their collar and survey file information. Different in assay value, i.e., magnesite grades present in the borehole sections are displayed in different colors.

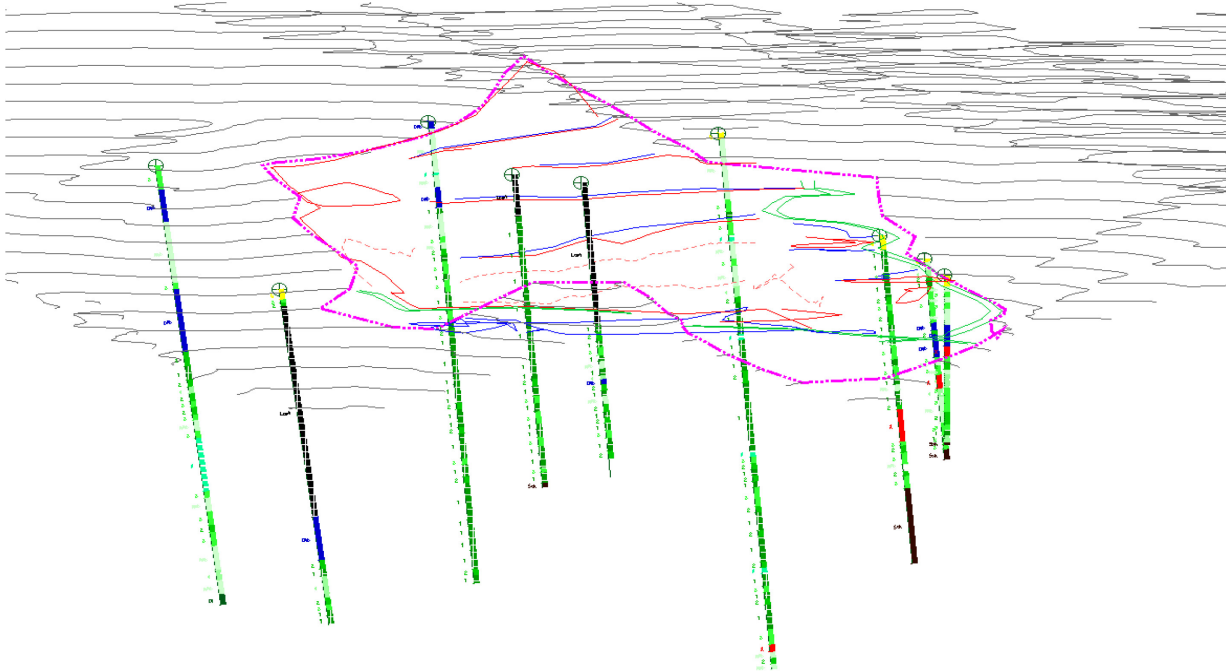


Figure 66: Boreholes with different ore grades from the open pit area. View to SSW. Green → ore zones, Blue → dolomite, Black → drillcore “lost”.

The boreholes are vertically in NNW-SSE direction at 200m interval and are digitized to form ore sections which are further concatenated to cover the partition of the magnesite deposit. It must be mentioned that the entire extensions (lateral & vertical) of the ore body cannot be determined on the basis of the available data. Based on the borehole information, it can only be assumed that the deposit continues further at depth, to the West and to the East. The ore sections and the ore body footwall plane (foot wall rock → micaschist) are shown in Figure 67.

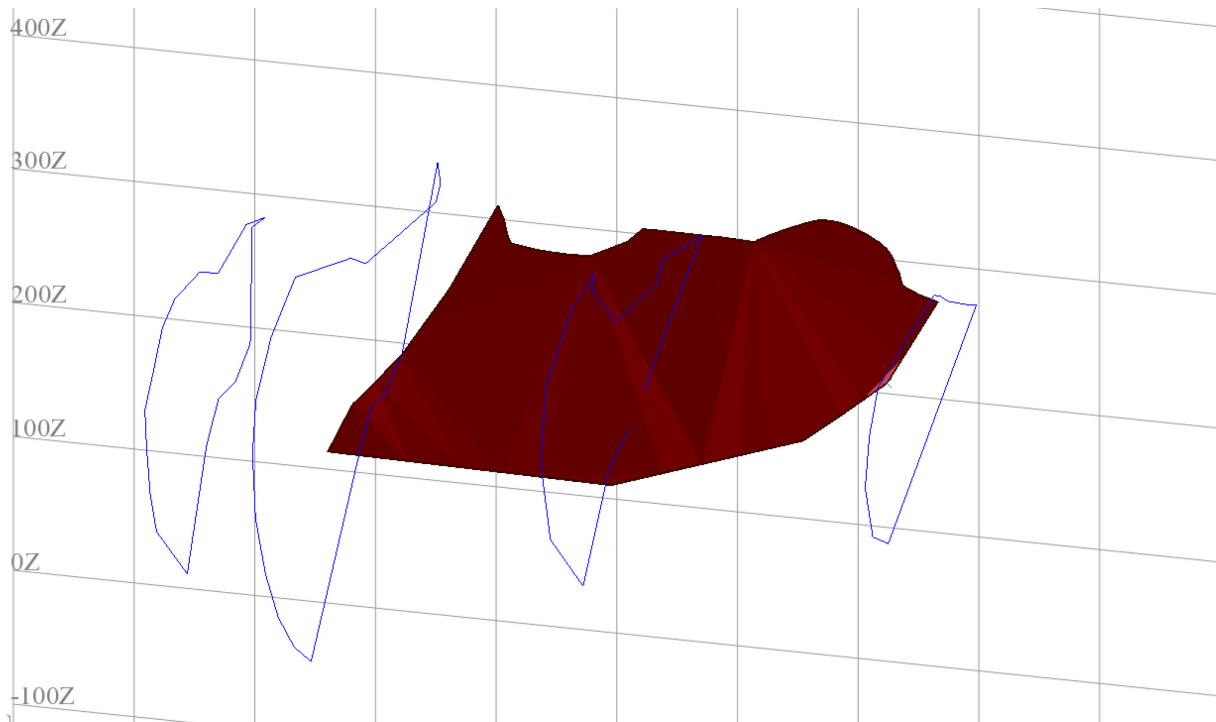


Figure 67: Ore strings showing the partition of the magnesite deposit. The brown plane adumbrates the magnesite footwall. View to the NNW.

The ore strings are oriented in clockwise direction and are then triangulated to form solid model of the Aihai magnesite deposit. The object after triangulation is validated for presence of edges, triangles, etc. Once validation is done the objects are set to solid. The solid is shown in Figure 68.

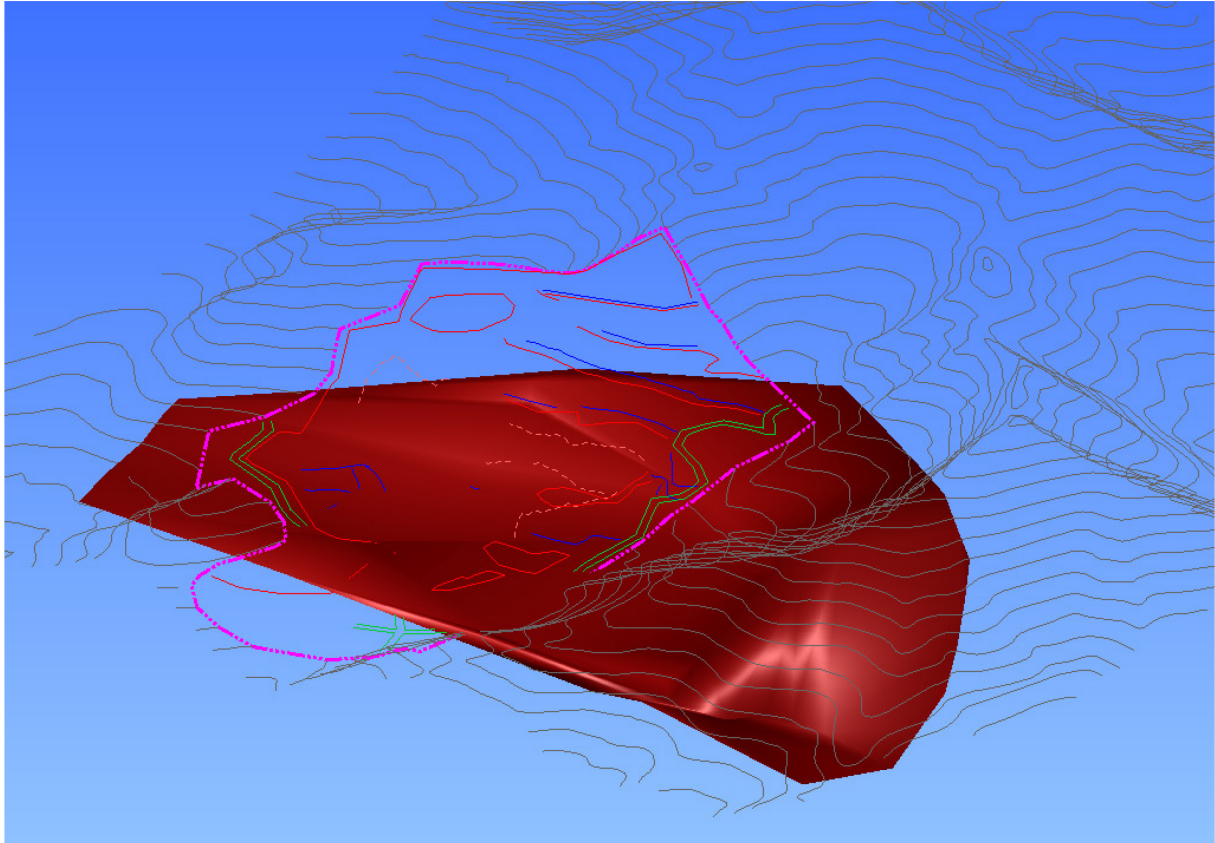


Figure 68: Solid model of the Aihai magnesite deposit. View to the SE.

Basic to application of computer techniques for grade and tonnage estimation is the visualization of the deposit as a collection of blocks. The solid model is implemented in the block model of regular 10m x 10m x 10m sized blocks to form the constraint block model. By incorporating the solid model into the overall block model the excess blocks outside of the ore deposit are removed for geostatistical estimation of the deposit. The data generated are then used for pit sequencing. The constraint block model is shown in Figure 69.

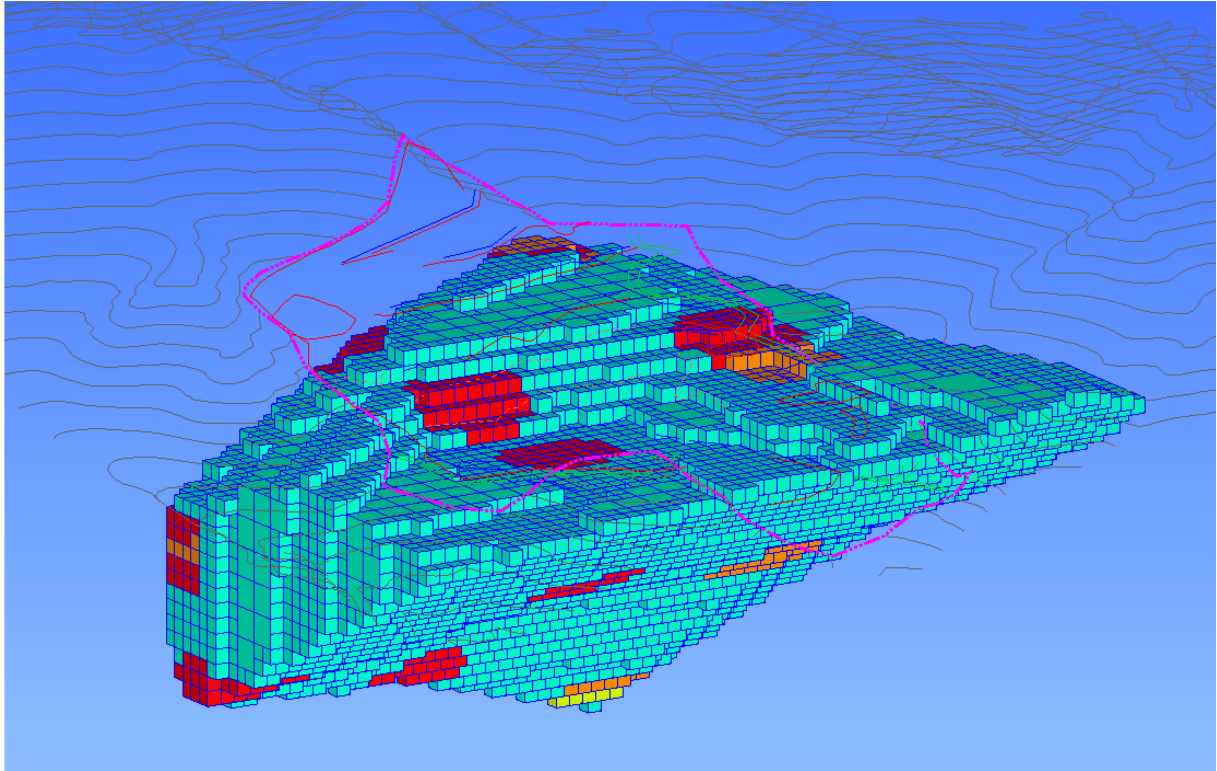


Figure 69: Constraint block model of the Aihai magnesite deposit. View to SW.

Finally the topographical surface of the open pit area was modeled. Surface modeling uses triangulation algorithms to create 3D models known as Digital Terrain Models (DTMs). A DTM is created from line and point data by forming a set of non-overlapping, adjacent triangles between points. The data bases for the surface model are survey points and contour lines. A distinction is made between areas affected by mining operations and the natural landscape (Figure 70).

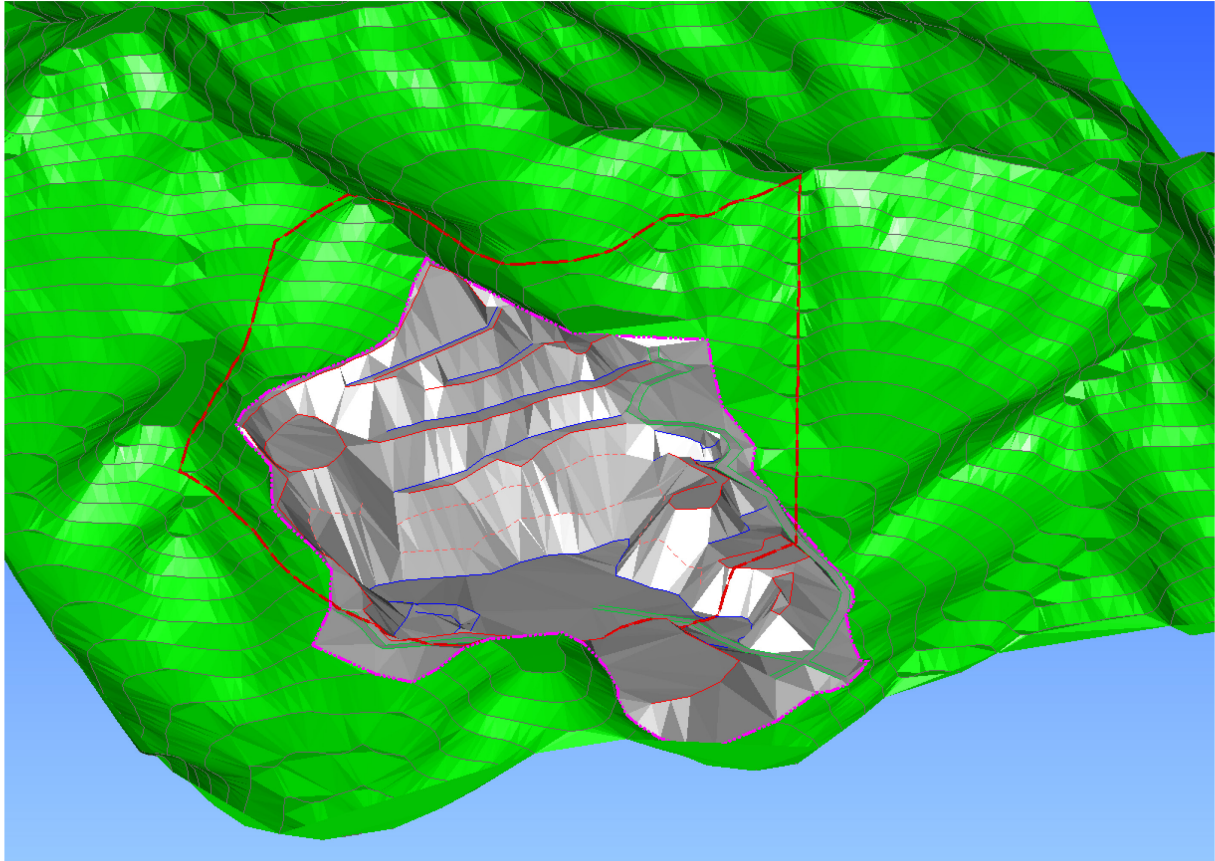
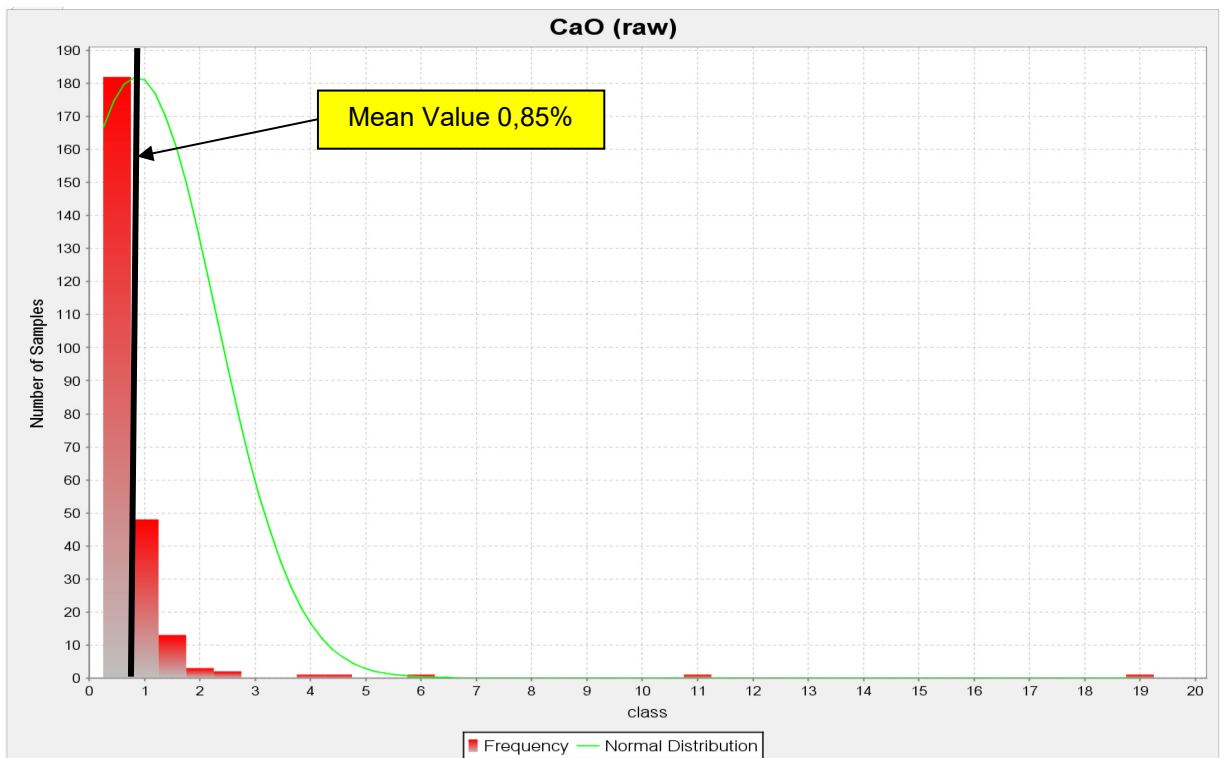
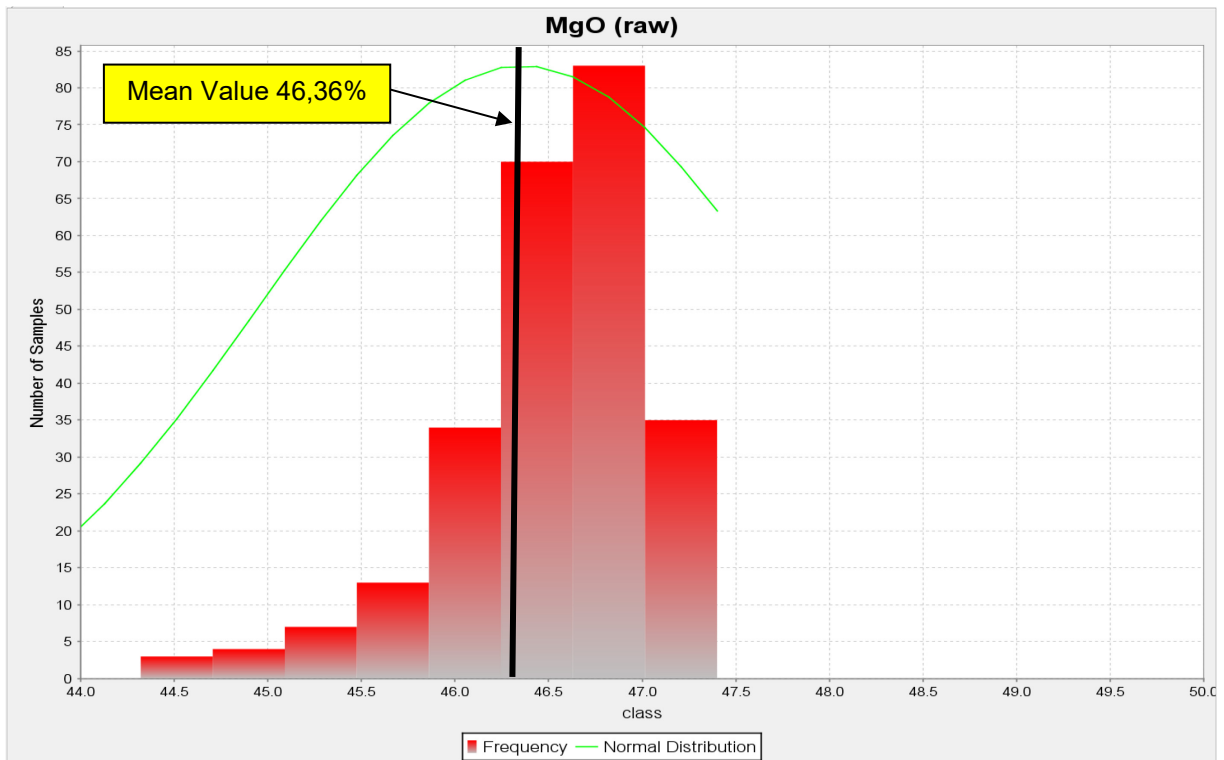


Figure 70: Digital terrain model (DTM) of the surface with 10m contour lines (grey). Green: natural landscape; grey: mining area; red dashed line: outline of the concession area; blue: bench toes; red: bench crests; light green: hauling roads, orange dashed lines: auxiliary lines. View to the SW.

1.21 Geostatistics: Inverse Distance vs. Ordinary Kriging

Different techniques can be used to assign grades to the blocks of the block model. The tonnage of each block is calculated by multiplying the block volume (the same for all blocks) by the density (which may vary). Two techniques will be discussed in this chapter. They are based upon the application of the sphere influence concept where grades are assigned to blocks by weighting the grades of nearby blocks. For simplification of these calculations the blocks are considered as point values rather than as volumes.

First the frequency distribution of the quality controlling parameters (MgO, SiO₂, CaO) is figured out. Then histograms of the drill-hole data are computed by using chemical data of the drilling campaign (Figure 71).



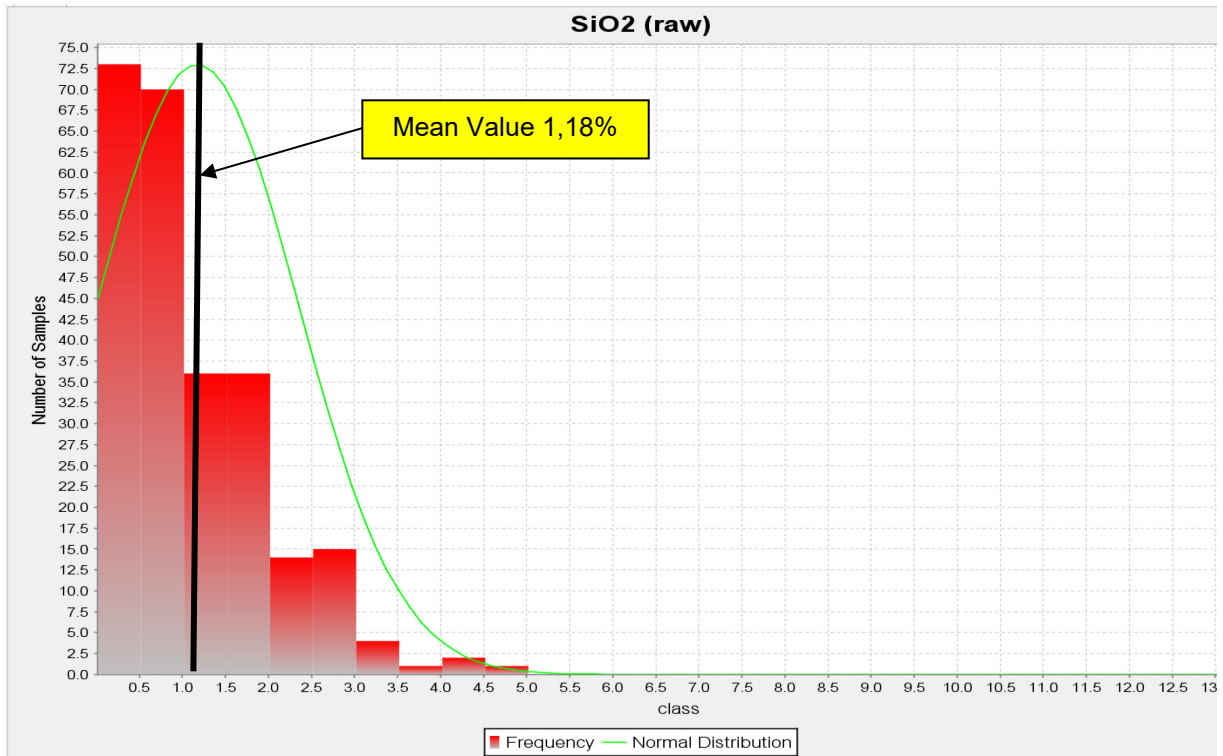


Figure 71: Histograms representation of all available chemical data of the ore drill cores. Data outside the ore body are neglected and handled as waste material.

If the grade distributions (MgO, CaO, and SiO₂) had been truly normal then a bell shaped curve would be expected. For MgO a normal distribution was found, but not for CaO and SiO₂.

Skewness (s) is an indication of the departure of tails of a distribution from symmetry about the mean. Positively skewed distributions have an excess of values extending as a tail toward higher values; negatively skewed distributions have a tail extending toward low values. Kurtosis is a measure of peakedness (i.e., the relative height of a distribution in a tight range about the mean (m)). Quantitative measures of skewness and kurtosis, available in most statistics texts, are not used in mineral inventory studies. Skewness as a general characteristic, however, is of considerable interest as an indication of whether a distribution is better described as normal or lognormal.

In practice, the coefficient of variation (CV) is commonly used for this purpose: $CV = s$ (skewness)/ m (mean). Values of CV less than 0.5 are likely to approach a normal

distribution, whereas values greater than 0.5 are skewed and may be described better by a lognormal distribution or a combination of distributions.

- a) MgO: Skewness = -9.38; Mean= 46.36 CV= 0.2 → *normal distr.*
- b) CaO: Skewness = 9.75; Mean= 0.85 CV= 11.47 → *lognormal distr.*
- c) SiO₂: Skewness = 4.90; Mean= 1.17 CV= 4.19 → *lognormal distr.*

The next step is to create variograms. The variogram is the key function in geostatistics as it is used to fit a model of the spatial correlation of the data. A variogram was generated for the MgO distribution with the following parameters (Figure 72), which represents a geometric characteristic of the deposit.

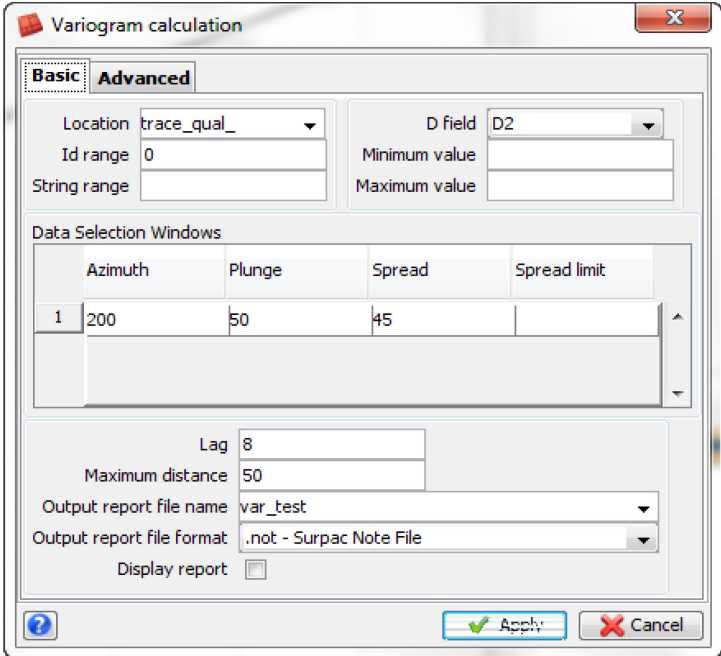


Figure 72: Surpac window with variogram calculation parameters calculation of the MgO distribution. Dip direction of the ore body 200°; dip 50° and the full spread angle is 90°.

The spherical variogram model has a nugget value of 0.107, a sill value of 1.802 and a range of 25.6. The sill is the semivariance value at which the variogram levels off. At this point the maximum variance value that can be attained by variography is reached. The range describes the lag distance at which the variogram reaches the sill value. Presumably, autocorrelation is essentially zero beyond the range. The nugget value represents the variability at distances smaller than the typical sample

spacing, including measurement error. The variogram model such obtained is shown in Figure 73.

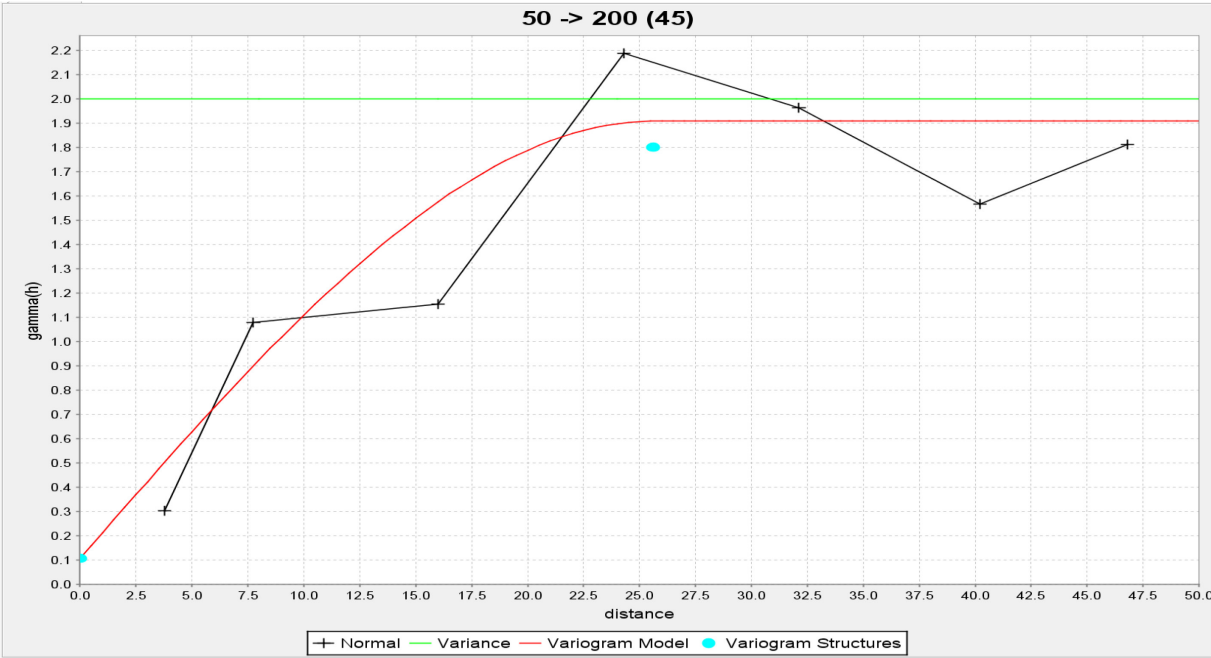


Figure 73: Variogram model of the MgO distribution. Green line → variance; Red line → variogram model; Black line → experimental variogram; Blue points → variogram structure.

The variogram model indicates that the amount of available information is insufficiently complete to predict a purposeful quality distribution of the ore body via Kriging method. Also, it should be noticed that the analyzed magnesite ore drill cores of the main ore body show minimal variance in quality. The MgO quality deviations vary in a range of few percentages ($\approx 2\%$) only (Figure 74). It is not feasible to forecast these quality refinements with geostatistic methods (Kriging). Particularly worth mentioning is the forecast radius of 25.6m. By taking drill hole distances of 100m (N-S) and 200m (W-E) into account, only 10% of the deposit can be predicted with geostatistic methods, respectively. As a consequence the forecast via Kriging method itemized 80% of the predicted blocks with the mean MgO value of 46,63% and with a variance of 1.99%.

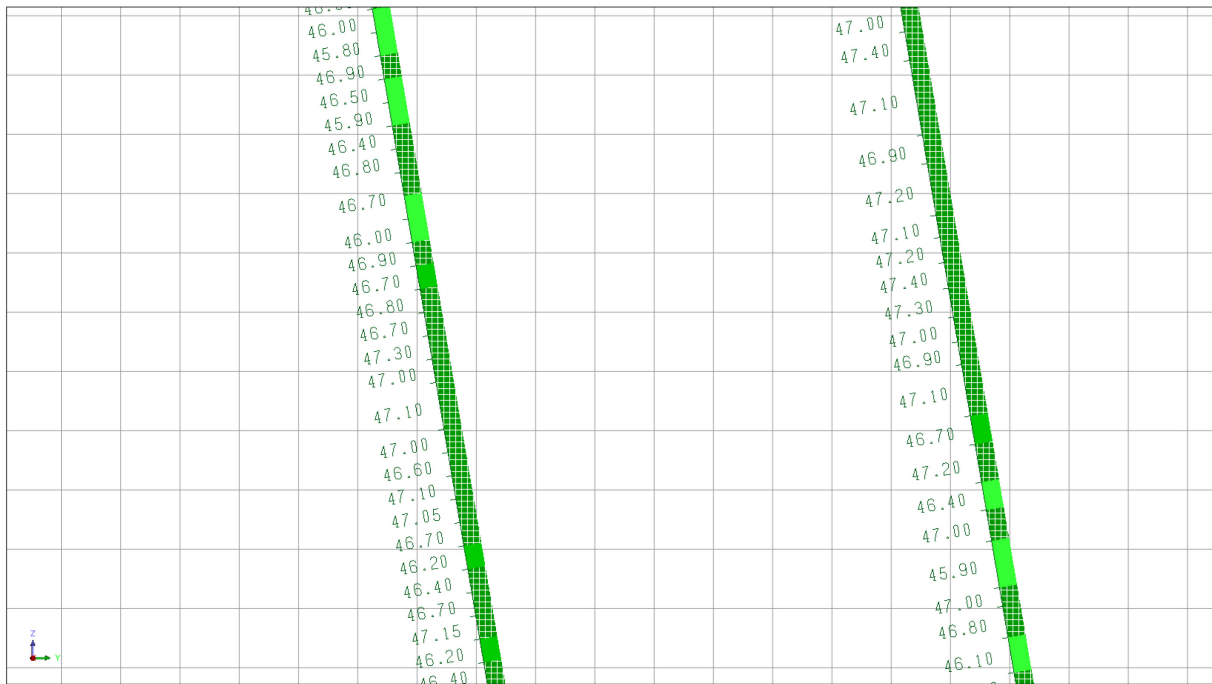


Figure 74: Drill hole section inside the ore body showing the MgO grades [%].

Another geostatistic sphere influence concept is the inverse distance weighting technique. The influence of surrounding grades varies inversely with the distance separating the grade and the block center. It is obvious that the grade of the block should be more similar to nearer points than to those far away. To emphasize this dependence, the weighting with distance can be increased. This can be done by the commonly used inverse distance squared (IDS) weighting formula

$$g = \frac{\sum_{i=1}^n \frac{g_i}{d_i^2}}{\sum_{i=1}^n \frac{1}{d_i^2}}$$

where g_i is the given grade at distance d_i away from the desired point. It is generally acknowledged that the IDS has been found to be suitable for a number of different kinds of deposits and is widely used.

In the case of the Aihai magnesite deposit the IDS weighting technique has been applied with an anisotropic search ellipsoid, to estimate the unknown block grades. An anisotropic condition exists when the rate of change of the data values is different in different directions. This is the case for nearly all data sets which represent

samples taken from mineral deposits. The anisotropy is caused by the geological conditions. The Aihai magnesite deposit is dominated by layering. The determination of the magnitude of anisotropy for a data set may be done qualitatively or quantitatively (by estimation or by numerical calculation). The variogram (Figure 73) gives only low quality information, so the IDS parameters (Figure 75) base on the geological fieldwork and experience.

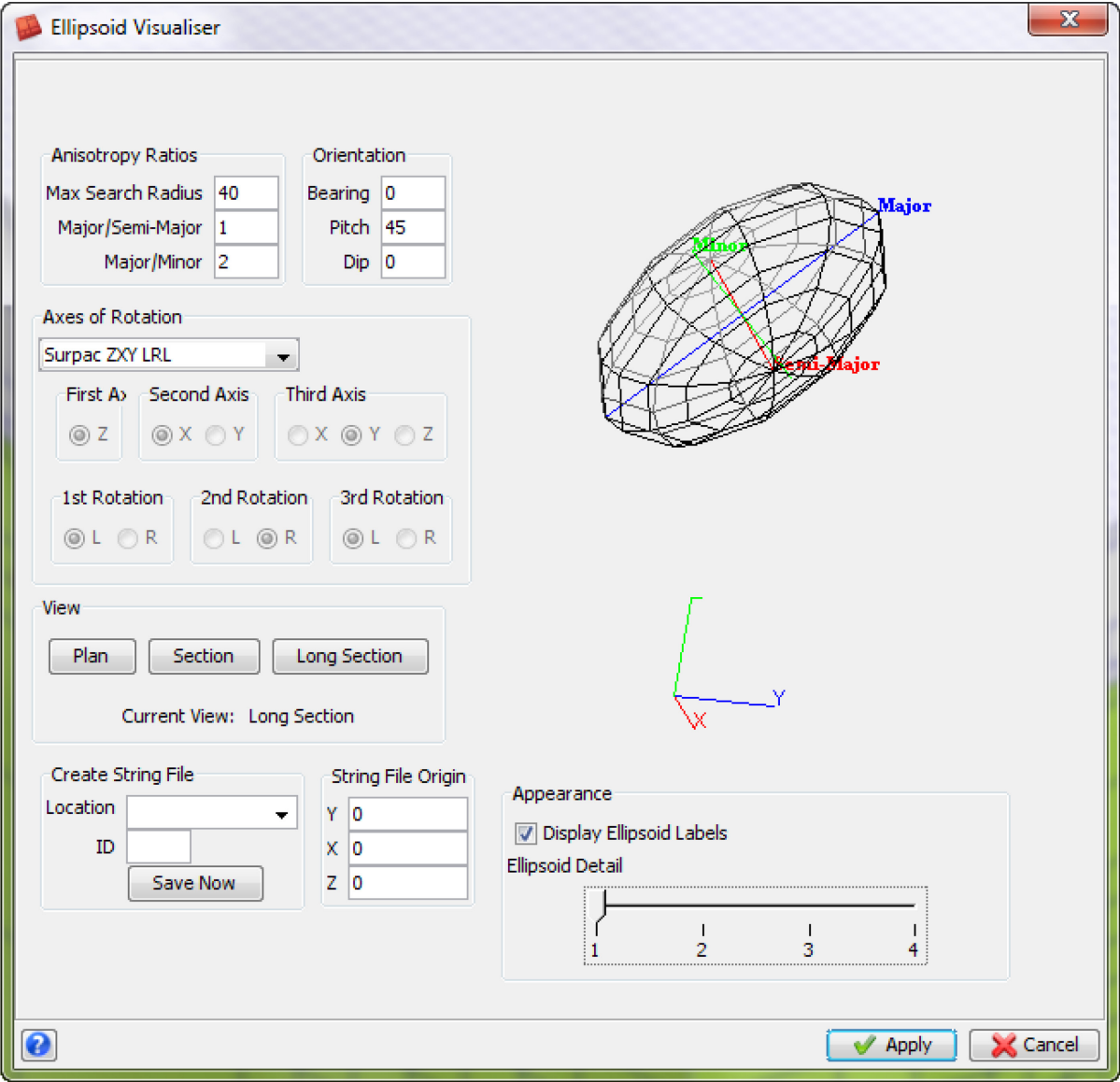


Figure 75: Search ellipsoid parameters.

The 40m radius was chosen for the anisotropic search ellipsoid because the ore layers show a homogenous trend in dip direction and parallel to the strike. The anisotropy ratio 1:2 says that the samples in the XY plane were weighted equal, while the sample influence in the YZ plane was reduced. The YZ plane stands vertical to

the ore layering. The IDS weighting estimation results are shown in figures 76 and 77. By increasing the forecast search radius from 25.6m to 40m, more than 20% of the ore body can be predicted. These 20% of the projected blocks show a rather high quality (relating to the quality determining grades of MgO, CaO, SiO₂). 1164 predicted blocks (10m x 10m x 10m) are distributed as follows: 20% T (“super grade”), 15% T1, 45% T2, 1% T3, T4 19%. The grade classifications in categories are shown in Table 6. The quality deteriorating factor is the CaO content in most cases.

级 别 Grade	化 学 成 份 Chemical composition (%)			
	MgO	CaO	SiO ₂	Distribution
特级品 super grade	≥47	≤0.6	≤0.6	20%
1 级品 grade 1	≥46	≤0.8	≤1.2	15%
2 级品 grade 2	≥45	≤1.5	≤1.5	45%
3 级品 grade 3	≥43	≤1.5	≤3.5	1%
4 级品 grade 4	≥41	≤ 6	≤ 2	19%

Table 6: Grades of magnesite ore (Standard → Liaoning Geological Survey Bureau).

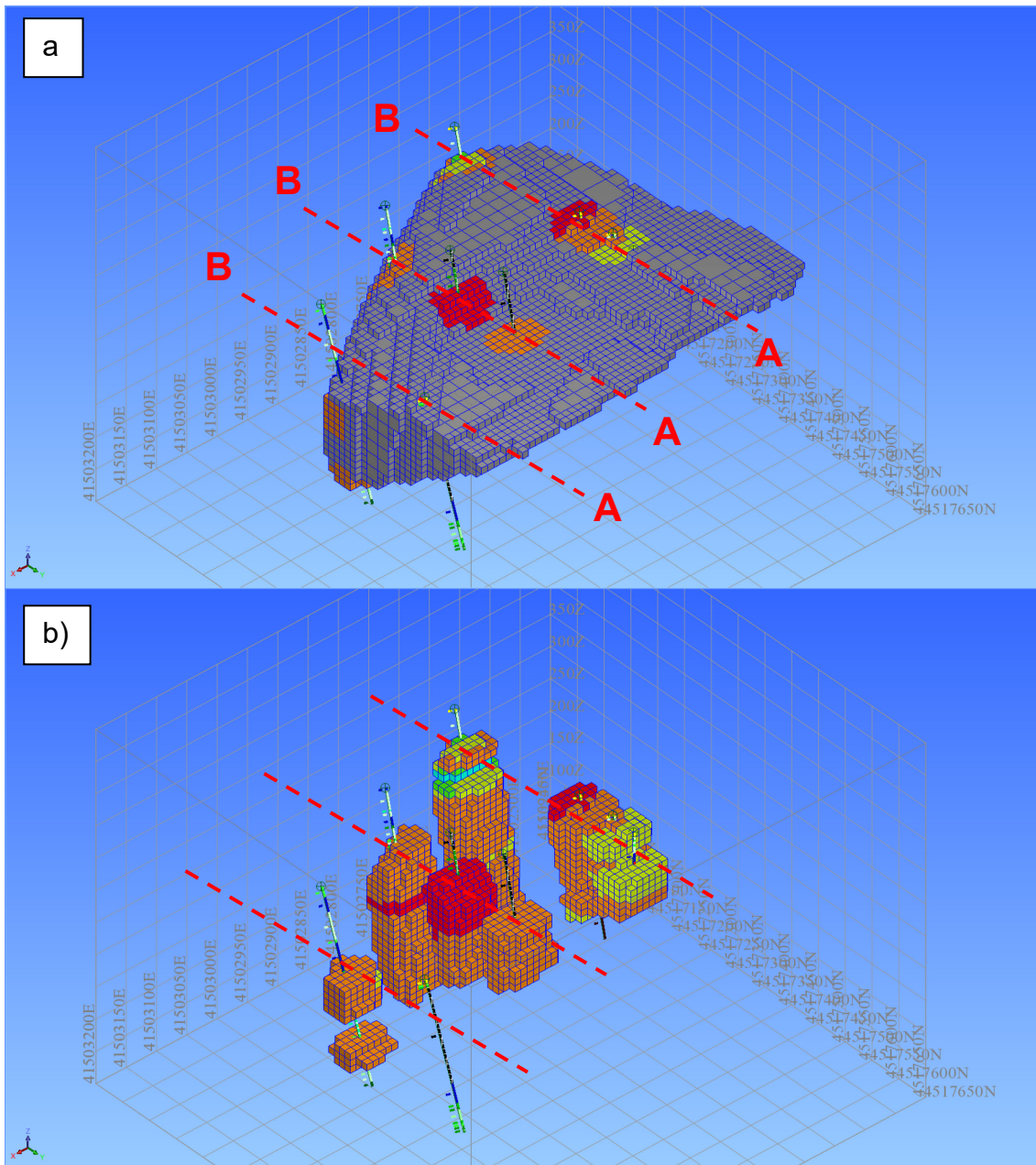


Figure 76: (a) Block model of the Aihai magnesite deposit; colored blocks were assigned quality grades through IDS estimation. Grey blocks are not affected by the IDS weighting, because they are outside of the search ellipsoid and (b) shows only the estimated blocks. It is obvious that the predicted blocks are accumulated around the drill holes where nearby data are available. The block colors according to MgO content. Red → MgO \geq 47%; Orange → MgO 46-47%; Yellow → MgO 45-46%; Green → MgO 43-45%; Blue → MgO 41-43%. Red dashed lines are section lines (Figure 77). View to the SW.

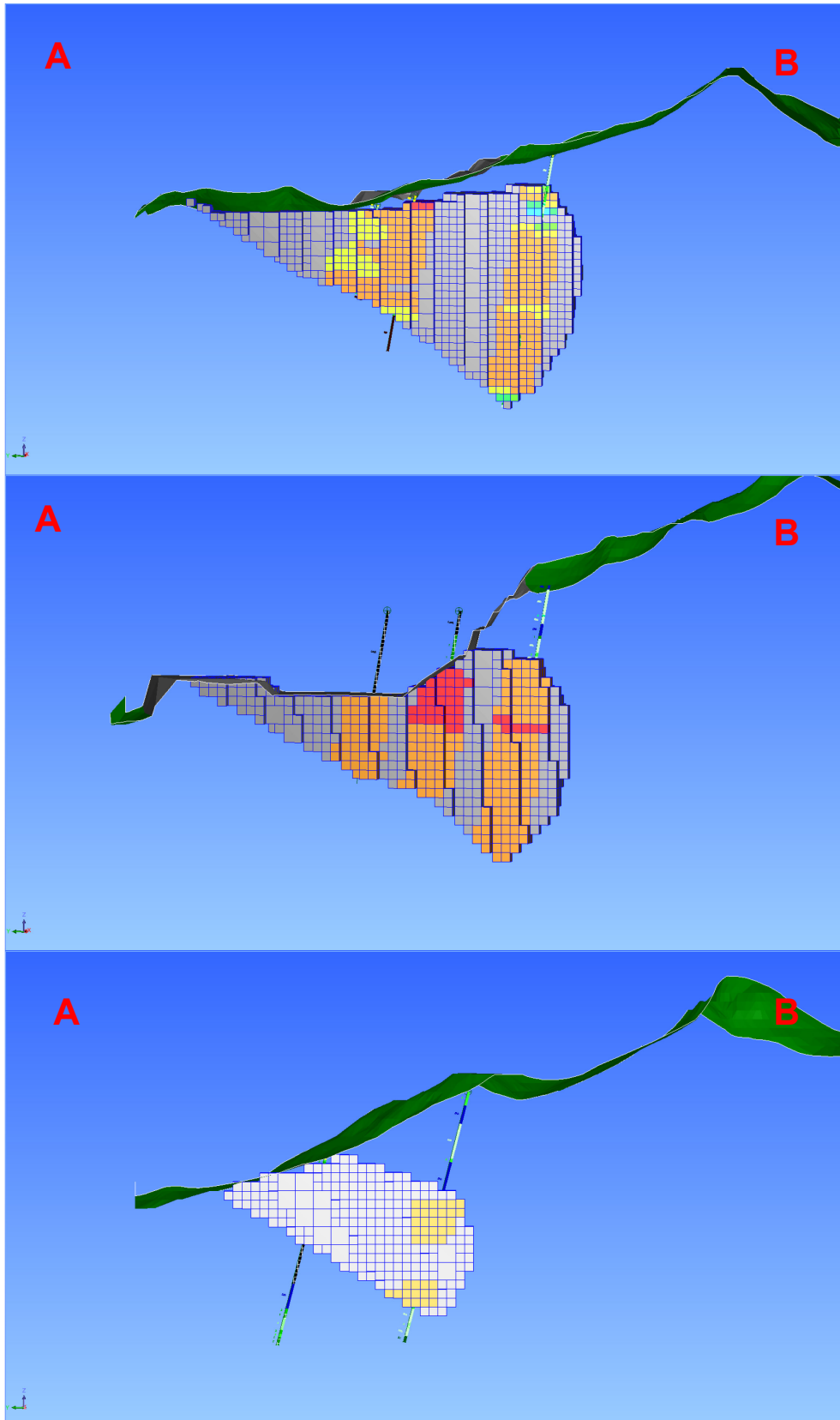


Figure 77: Vertical sections of the block model with drill-holes (color code see Figure 76). The green planes display the topographical surface.

1.22 Magnesite resource calculation

A “Mineral Resource” is a concentration or occurrence of material of intrinsic economic interest in or on the Earth’s crust in such form and quantity that there are reasonable prospects for eventual economic extraction. The location, quantity, grade, geological characteristics and continuity of a Mineral Resource are known, estimated or interpreted from specific geological evidence and knowledge. Mineral Resources are sub-divided, in order of increasing geological confidence, into Inferred, Indicated and Measured categories (AusIMM, 2005). The general relationship between Exploration Results, Mineral Resources and Ore Reserves are shown Figure 78.

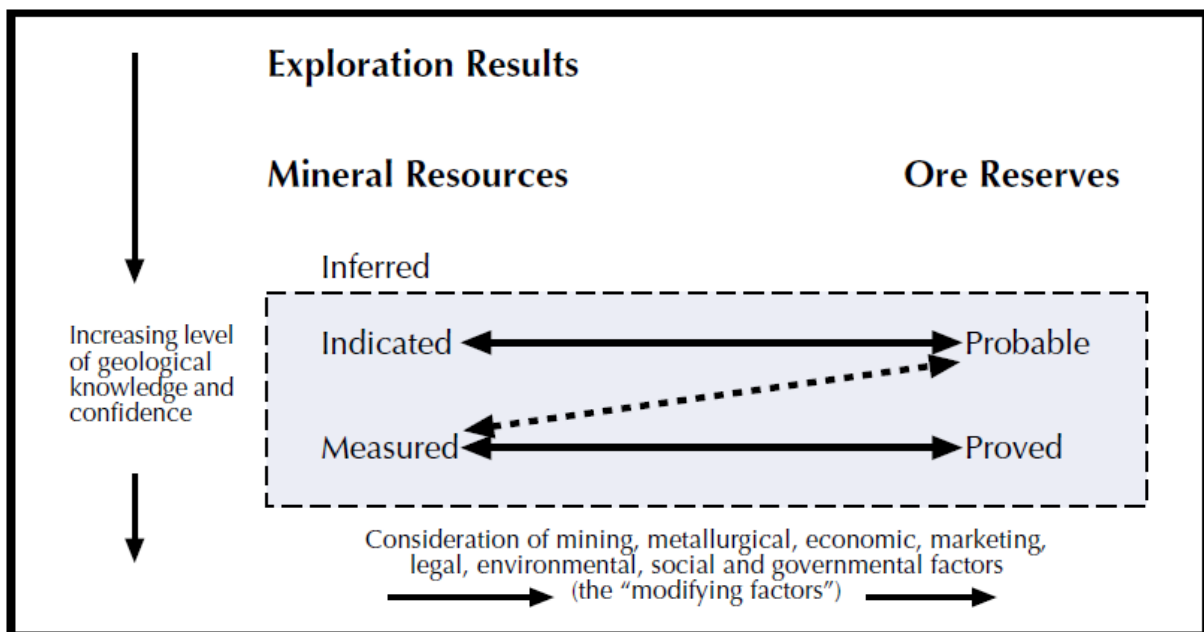
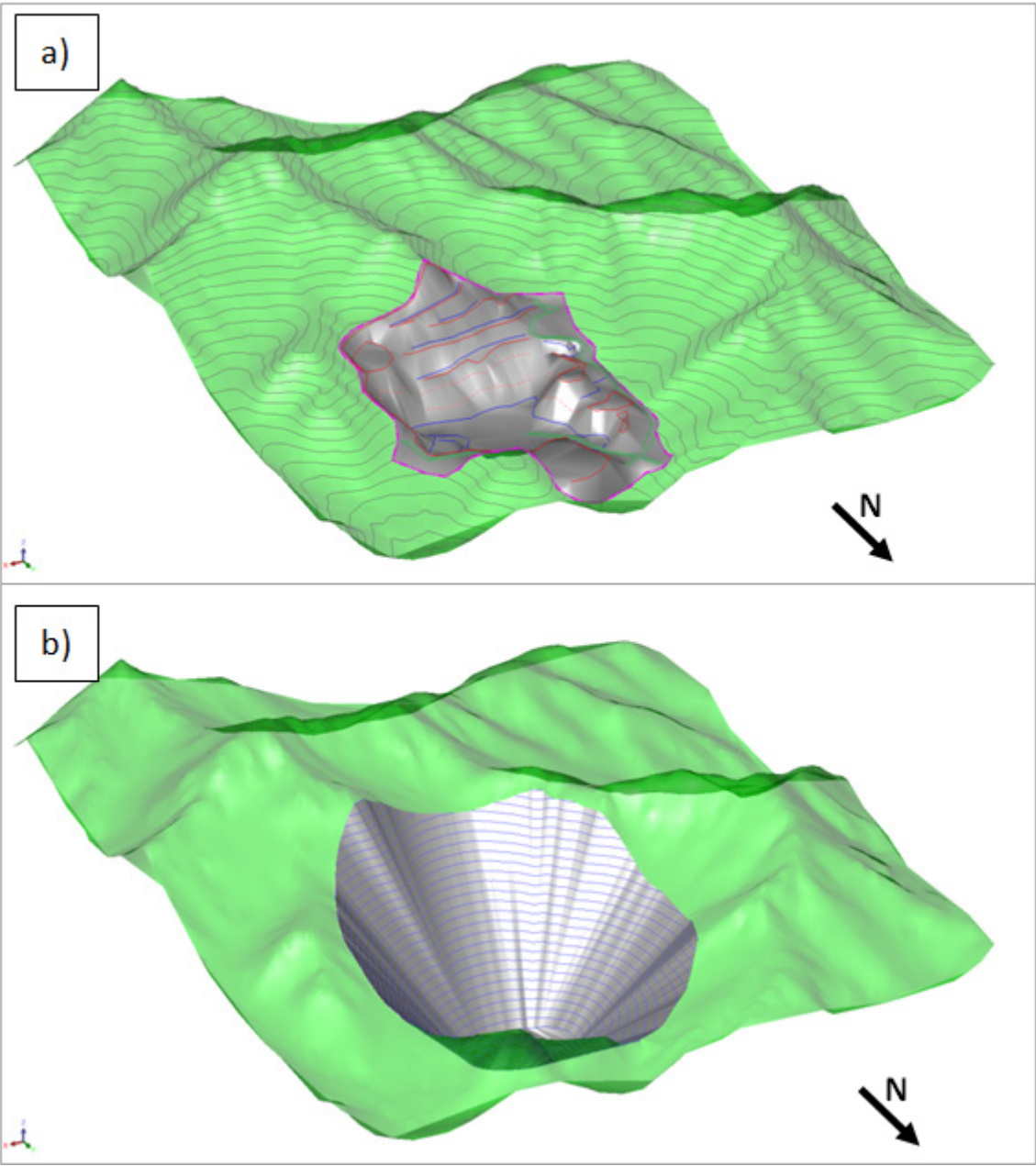


Figure 78: The general relationship between exploration results, mineral resources and ore reserves (AusIMM, 2005).

A big portion of the Aihai magnesite deposit does not have the potential for eventual near future economic extraction in the next 20 years because the ore body extends high depth where the dolomitic overburden is unfavorably thick. It should be also listed that the drilling campaign did not explore the continuity of the ore body into depth and laterally outside of the concession area. So it is not constructive to calculate the mineral resource for the entire magnesite ore body, because the quantity of available data is generally not sufficient to allow any reasonable estimates of mineral resource. To tackle this issue a simplified long term mine plan was designed for a mineral resource calculation in a defined geometric area. The

advantage of such an approach is that comprehensible, actual geological surface data from a defined area can be used. In addition the long term mine plan was elaborated. For the next thirty years it proposes a possible development of the open pit and the individual stripping ratios for each bench.

The long term open pit design is rather primitive; it is a cone with flattened tip, without any ramps, benches or dump site design (Figure 79). This open pit design focuses on the overall slope angle only. The overall slope angle is an important geometric parameter which has significant economic impact.



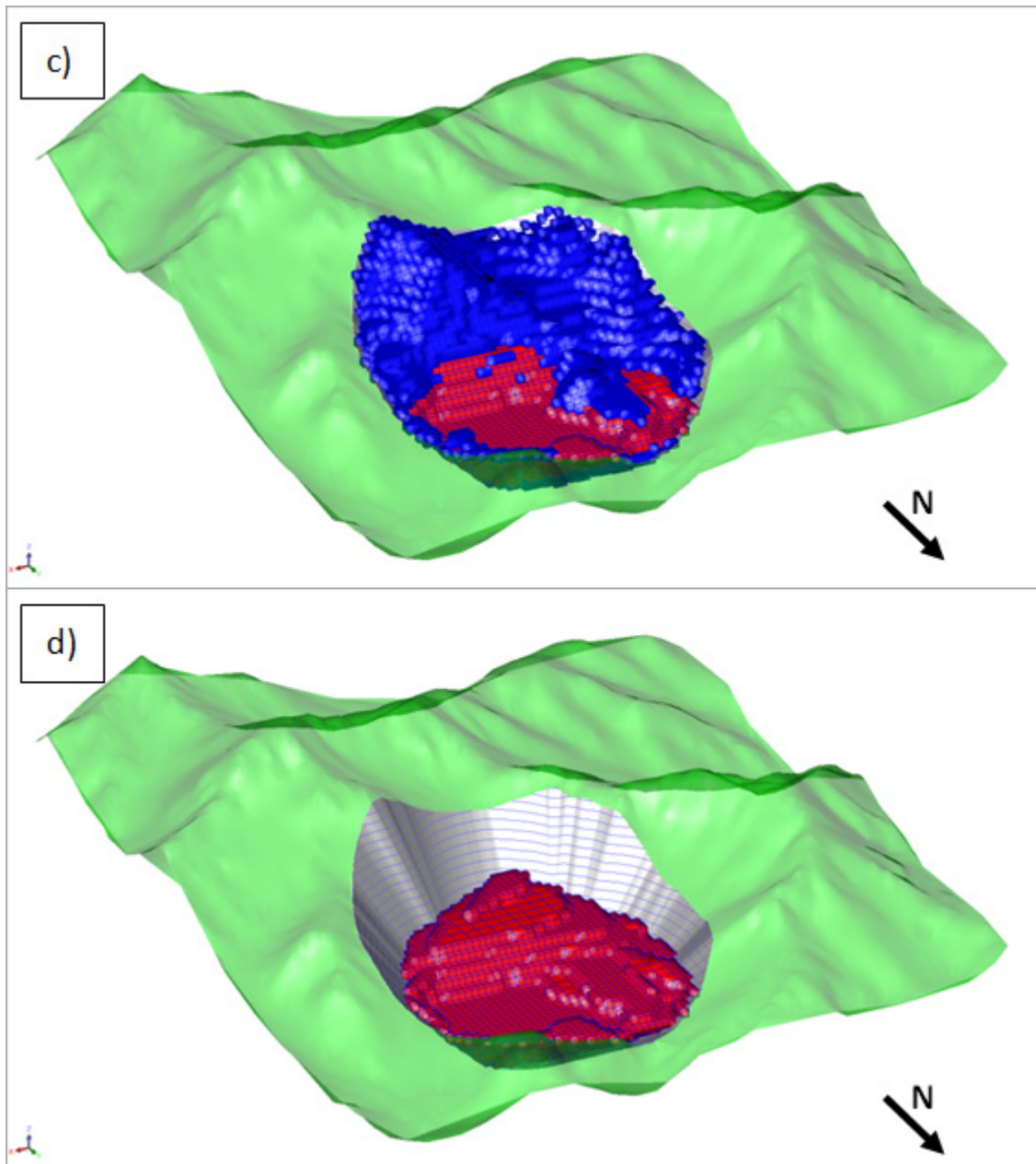


Figure 79: (a) Actual open pit situation. (b) Long term mine plan with the ultimate pit design after 30 years. Proposed pit bottom is 200m above sea level then. (c) Ultimate pit design including the block model. Red → magnesite ore; Blue → overburden. (d) Ultimate pit design with the mineable magnesite ore, displayed as red blocks.

The ultimate pit design is characterized by three different overall pit slope angles at different positions of the mine. Every one of these should be handled as final overall slope angle. The first overall pit angle from the North pit wall is the most critical one, because the North pit wall has the same orientation like the ore layering. For stability purposes the North overall pit slope should be flatter by $>5^\circ$ than the dipping angle of

the ore layering, i.e. 30°-35° (Figure 80). For the South pit wall an angle of 45°-50°, and for the E & W pit walls an angle of 45° are proposed.

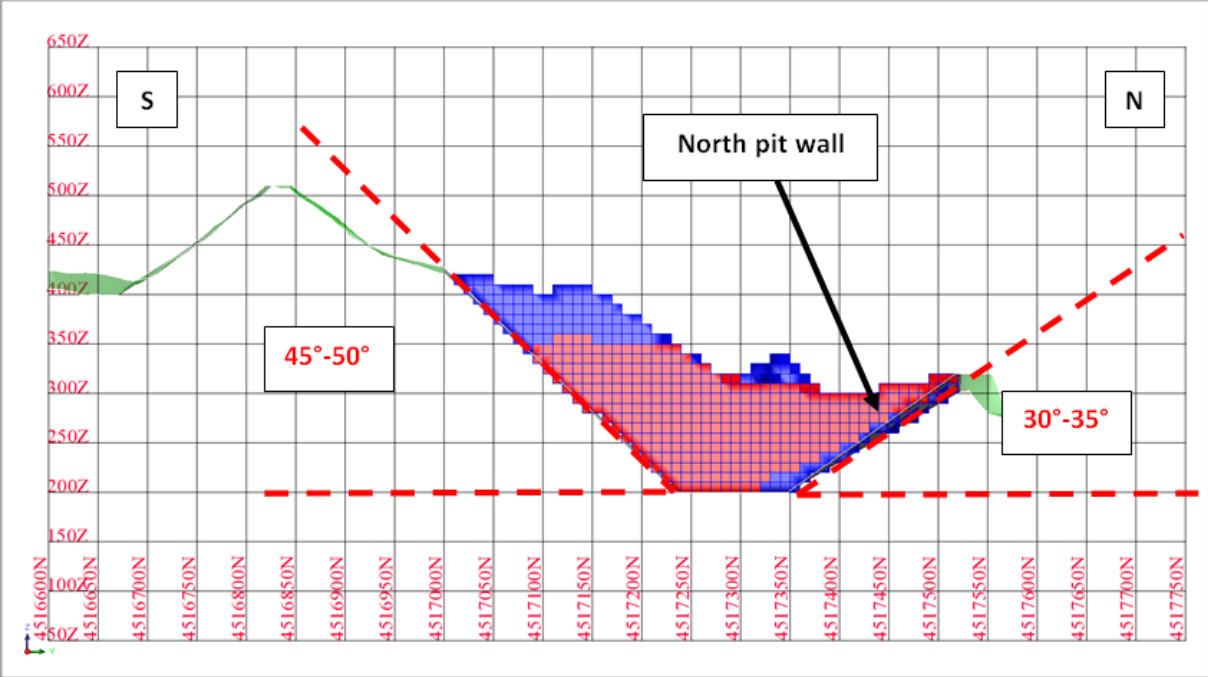


Figure 80: North-South cross section of the ultimate pit design, showing two different overall slope angles.

For the ore resource calculation an approximated magnesite density of 2.95 g/cm³ was used. This is an average value which means that inclusions of dolomite, diabase dykes and silicified marbles inside the ore layers have to be subtracted from the ore, to figure out the real magnesite resources. These impurities were not registered by the drilling campaign and represent a minor portion of the whole ore resources (< 2%).

Within the Aihai concession area the geologically interpreted ore body, which is a partition of the entire ore body, has a tonnage of 75.107 million tons and a volume of 25.46 million cubic meters. This tonnage value can be termed as Inferred Resources according to JORC-Code.

Considering the thirty years mine plan, in total 21.948 million tons (Volume = 7.44 million m³) of ore can be mined. These resources can be sub-divided into 4.45 million tons of Indicated Resources and in 17.5 million tons of Inferred Resources. The

calculation of Indicated Resources is based on geological field investigations and on actual mining data.

To get access to all 21.948 million tons of resources about 12.08 million tons of overburden has to be removed. These values result in an overall stripping ratio of 1:0.55 (Ore: Waste). The ore/waste ratio is shown in Figure 81 for 10 meter thick horizontal slices between the proposed pit bottom at 200m up to 480m above sea level.

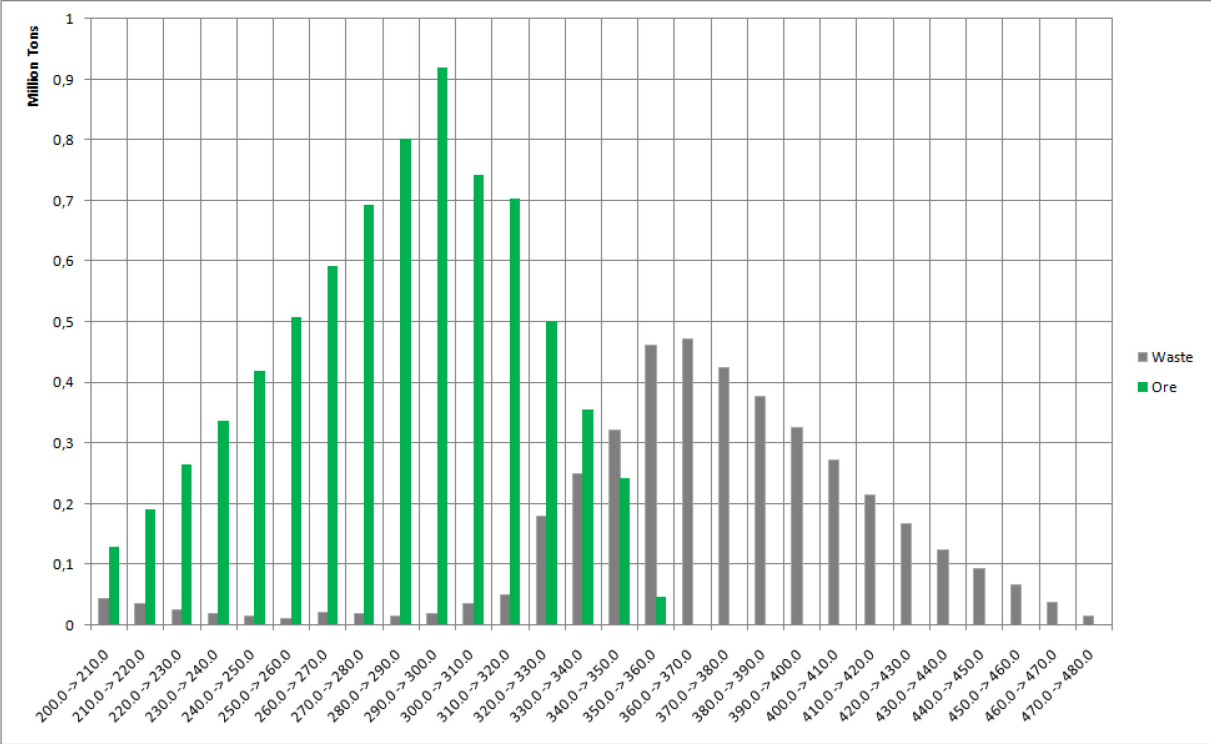


Figure 81: The diagram shows the ore/waste ratios for the different elevation steps (10m ranges).

Discussion

The present report is considered to be a base of further investigations regarding the magnesite genesis in the Liaohe Group. Additionally, the geochemical, petrographical and 3D modeling results should support the company in various issues.

In future projects the 3D modeling concept should be pushed. The establishment of basic principles in this area is vital for a prosperous development of the Aihai open pit. This 3D model is the basis for continuous improvement and development of quality control and quality forecast. For the establishment of a quality distribution block model additional comprehensive data are required. A reliable and reproducible sampling and analyzing procedure depending on well-defined quality criteria is of paramount importance. For the determination of the MgO, SiO₂, CaO average contents, drilling chips of the bench blast holes could be taken. The chemical data should be added to the existing data base.

Every short and long term mine plan has to be based on a well-founded quality distribution. The plan should provide the ways and means of further qualitative and quantitative growth of the Aihai magnesite operation. Additional concepts of ongoing optimization, fine-tuning of the mining process and open pit design shall be included there.

The concession area is the most limiting factor in the open pit mining operation. The set borderlines confine the geometry of the open pit. The consequences are manifold: increase of the general slope angle, stability and safety problems, loss of flexible mining points, short-term decrease of the ore to waste and significant shortening of the mines' lifetime. An extension of the concession area would have several benefits like a spacious access to the ore, possibility of more selective mining for better quality control, greater work safety, bigger dump capacity for the overburden, storage space for ore products in the mine area, higher rate of recovery and increase of lifetime.

References:

Aharon, P., 1988. A stable isotope study of magnesite from the Rum Jungle Uranium field, Australia: implications for the origin of strata-bound massive magnesite. *Chem. Geol.*, 69, 127-145.

AusIMM, 2005. Australasian Code for reporting of exploration results, mineral resources and ore reserves: The JORC Code – 2004 Edition. http://www.jorc.org/docs/jorc2004web_v2.pdf

Bai, J. 1993. The Precambrian geology and Pb-Zn mineralization in the northern margin of North China Platform. Geological Publishing House, Beijing; 1–123 ,in Chinese with English Abstract.

Bai, J., Wang, R.Z., and Guo, J.J., 1992, The major geologic events of Early Precambrian and their dating in Wutaishan Region. Beijing, Geological Publishing House.

Bau, M., 1996. Controls on the fractionation of isovalent trace elements in magmatic and aqueous systems: Evidence from Y/Ho, Zr/Hf, and lanthanide tetrad effect. *Contributions to Mineralogy and Petrology*. 123, 323-333.

Bau, M., Möller, P., 1992. Rare Earth Element Fractionation in Metamorphogenic Hydrothermal Calcite, Magnesite and Siderite. *Mineralogy and Petrology*. 45, 231-246.

Botz, R., von der Borch, C., (1984). Stable isotope study of carbonate sediments from the Coorong Area, South Australia. *Sedimentology*, 31, 837-849

Chen, C., 2000. A Study of the Minerogenic System of Magnesian Non-metallic Deposits in Early Proterozoic Magnesian Carbonate Formations in Eastern Liaoning Province, China. PH.D. thesis, China University of Geosciences.

Chen, C., Cai, K., 1998. A study of magnesian non-metallic deposits and minerogenesis in early Proterozoic magnesian carbonate formations in Eastern Liaoning province China. *Geology of Mineral Deposits* 17, 465-468.

Chen, C., Cai, K., 2000. Minerogenic System of Magnesian Nonmetallic Deposits in Early Proterozoic Mg-rich Carbonate Formations in Eastern Liaoning Province. *Acta Petrologica Sinica* 74, 623-631.

Chen, C., Jiang, S., Cai, K., Ma, B., 2003. Metallogenic conditions of magnesite nonmetallic deposits in the Early Proterozoic Mg-rich carbonate formations, eastern Liaoning province. *Mineral Deposits*, 22, 166-167, in Chinese.

Chen, C., Lu, A., Cai, K., Zhai, Y., 2002. Sedimentary characteristics of Mg-rich carbonate formations and minerogenic fluids of magnesite and talc occurrences in early Proterozoic in eastern Liaoning Province, China. *Science in China* 45, 84-92.

Chen, R. & Wang, Y., 1994. The evolution and metallogesis of early Proterozoic palaeorift in eastern Liaoning and southern Jilin provinces. *Precambrian Geology and Tectonics in China*. Beijing: Seismological Publishing House, 186-200.

Cheng Y.Q., 1994. *Outline of Regional Geology of China*. Geological Publishing House, Beijing.

Condie, K.C., Boryta, M.D., Liu, J.Z., Qian, X.L., 1992. The origin of Khondalites – Geochemical evidence from the Archean to Early Proterozoic Granulite Belt in the North China Craton. *Precambrian Res.* 59, 207-223.

Dong, Q., Feng, B., Li, X., 1996. The lithofacies and paleogeographical setting of Haicheng-Dashiqiao superlarge magnesite deposits, Liaoning province. *J. Changchun Univ. Earth Sci.* 26, 69-73.

Fairchild, I., Marshall, J., Bertrand-Sarafati, J., 1990. Stratigraphic shifts in carbon isotopes from Proterozoic stromatolitic carbonates (Mauritania): influences of primary mineralogy and diagenesis. *American Journal of Science*, 290, 46-79.

Fallick, A., Ilich, M., Russell, M., (1991). A stable isotope study of the magnesite deposits associated with the alpine-type ultramafic rocks of Yugoslavia. *Econ. Geol.*, 86, 847-861.

Faure, M., Lin, W., Monie, P., Bruguier, O. 2004. Palaeoproterozoic arc magmatism and collision in Liaodong Peninsula (north-east China). *Terra Nova* 16, 75–80.

Feng, B., Zhu, G., Dong, Q., 1995. The geological characteristic and origin of superlarge magnesite deposits in Haicheng-Dashiqiao, Liaoning province. *J. Changchun Univ. Earth Sci.* 25, 121-124.

Fleet, A., 1984. Aqueous and sedimentary geochemistry of the rare earth elements. In P. Henderson and W. Fyfe, eds., *Rare Earth Geochemistry*. Elsevier, Amsterdam. 343-373.

Fraley, C., Raftery, A., 2007. Model-based Methods of Classification: Using the mclust Software in Chemometrics. *Journal of Statistical Software*, 18, 6.

Franz, E., Ponce, J., Wetzstein, W., 1979. Geochemie und Petrographie der Magnesitlagerstätten des Alto Chapere/Bolivien. *Radex- Rundschau*. 699-706.

Godovikov, A., 1975. *Mineralogija*. Nedra, Moskva.

Greaves, M., Elderfield, H., Sholkovitz, E., 1999. Aeolian source of rare earth elements to the Western Pacific Ocean. *Marine Chemistry*. 68, 31-38.

Guerrera, A., Peacock, S., Knauth, L., 1997. Large ^{18}O and ^{13}C depletion in greenschist facies carbonate rocks, western Arizona. *Geology*, 25, 943-946.

Guo, J.H. and Zhai, M.G., 2001. Sm-Nd age dating of high-pressure granulites and amphibolite from Sanggan area, North China craton. *Chinese Science Bulletin*, 46, 106–111.

He, G.P., Ye, H.W. 1998. Two types of Early Proterozoic metamorphism in the eastern Liaoning and southern Jilin provinces and their tectonic implication. *Acta Petrologica Sinica* 14, 152–162, in Chinese with English abstract.

Huang, J.Q., 1977. The basic outline of China tectonics. *Acta Geol. Sin.* 52, 117-135.

Hudson, J., 1977. Stable isotopes and limestone lithification. *Journal of Geological Society London*, 133, 637-660.

Jiang, C., 1987. The early Precambrian Geology of Eastern Liaoning Province and Jilin Province. Shenyang: Liaoning Sci. & Tech. Publ. House, 135, in Chinese.

Jiang, S., Chen, C., Chen, J., Jiang, J., Dai, B., Ni, P., 2004. Geochemistry and genetic model for the giant magnesite deposits in eastern Liaoning Province, China. *Acta Petrologica Sinica*, 20, 765-772.

Jiang, S.Y., Palmer, M.R., Peng, Q.M., Yang, J.H., 1997. Chemical and stable isotopic compositions of Proterozoic metamorphosed evaporates and associated tourmalines from the Houxianyu borate deposit, eastern Liaoning, China. *Chemical Geology* 135, 189–211.

Jiang, Y., Jiang, S., Zhao, K., Ni, P., Ling, H., Liu, D., 2005. SHRIMP U-Pb zircon dating for lamprophyre from Liadong Peninsula: Constraints on the initial time of Mesozoic lithosphere thinning beneath eastern China. *Chinese Science Bulletin* 50, 2612-2620.

Kamber, B., Webb, G., 2001. The geochemistry of late Archean microbial carbonate: implications for ocean chemistry and continental erosion history. *Geochimica et Cosmochimica Acta*. 65, 2509-2525.

Keith, M., Weber, J., 1964. Carbon and oxygen isotopic composition of selected limestones and fossils. *Geochim. Cosmochim. Acta.* 28, 185-193

Komiya, T., Hirata, T., Kitajima, K., Yamamoto, S., Shibuya, T., Sawaki, Y., Ishikawa, T., Shu, D., Li, Y., Han, J., 2008. Evolution of composition of seawater through geological time, and its influence on the evolution of life. *Gondwana Research.* 14, 159-174.

Kralik, M. and Hoefs, J., 1978. Die Isotopenzusammensetzung der Karbonate in der Magnesitlagerstätte Eugui West-pyrenäen. *Tschermaks Mineral. Petrogr. Mitt.*, 25, 185-193

Kralik, M., Aharon, P., Schroll, E., Zachmann, D., 1989. Carbon and oxygen isotope systematics of magnesite: review. In: *Magnesite. Geology, Mineralogy, Geochemistry, Formation of Mg-Carbonates* (Ed. P. Möller), *Monogr. Ser. Mineral Deposits*, 28, 197-223.

Kusky, T.M., Li, J.H., 2003. Paleoproterozoic tectonic evolution of the North China Craton. *J. Asian Earth Sci.* 22, 383-397.

Lambert, I., Donnelly, T., Etminan, H., Rowlands, N., 1984. Genesis of Late Proterozoic copper mineralisation, Copper Claim, South Australia. *Econ. Geol.*, 79, 461-475.

Lawrence, M., Greig, A., Collerson, K., Kamber, B., 2006. Rare earth element and Yttrium variability in South East Queensland waterways. *Aquatic Geochemistry.* 12, 39-72.

Li, S.Z., Han, Z.Z., Liu, Y.J., Yang, Z.S., Ma, R. 2001. Continental dynamics and regional metamorphism of the Liaohe Group. *Geological Review* 47, 9–18, in Chinese with English Abstract.

Li, S.Z., Yang, Z.S., Liu, Y.J., 1995. Paleoproterozoic tectonic framework of the eastern North China Craton. *J. Changchun Univ. Sci. Tech.* 25, 14-21, in Chinese.

Li, S.Z., Zhao, G.C. 2007. SHRIMP U-Pb zircon geochronology of the Paleoproterozoic Liaoji granitoids: constraints on the tectonic evolution of the Eastern Block, North China Craton. *Precambrian Res.* 158, 1–16.

Li, S.Z., Zhao, G.C., Santosh, M., Liu, X., Dai, L.M., 2011. Paleoproterozoic tectonothermal evolution and deep crustal processes in the Jiao-Liao-Ji Belt, North China Craton: a review. *Geol. J.*, Online Publication in Wiley Online Library (wileyonlinelibrary.com).

Li, S.Z., Zhao, G.C., Sun M., Wu, F.Y., Hao, D.F., Han, Z.Z, Luo, Y., Xia, X.P., 2004. Deformational history of the Paleoproterozoic Liaohe Group in the Eastern Block of the North China Craton. *J. Asian Earth Sci.*

Li, S.Z., Zhao, G.C., Sun, M., Han, Z.Z., Luo, Y., Hao, D.F., Xia, X.P. 2005. Deformation history of the Paleoproterozoic Liaohe assemblage in the Eastern Block of the North China Craton. *Journal of Asian Earth Sciences* 24, 659–674.

Liu, J.L., Liu, Y.J., Chen, H., Sha, D.M., Wang, H.C. 1997. The inner zone of the Liaoji Paleorift: its early structural styles and structural evolution. *Journal of Asian Earth Sciences* 15, 19–31.

Liu, S., Liu, Y., Lin, G., Zhou, Y., Gong, F., Zhang, D., 2006. REE geochemical characteristics and geological significance of mudstone from Neogene, Nanpu Sag, Bohai Basin. *Geoscience.* 20, 449-456.

Lloyd, R., 1966. Oxygen enrichment of sea water by evaporation. *Geochem. Cosmochim. Acta*, 30, 801-819.

Luo, Y., Sun, M., Zhao, G.C., Li, S.Z., Xia, X.P. 2006. LA-ICP-MS U-Pb zircon geochronology of the Yushulazi Group in the Eastern Block, North China Craton. *International Geology Review* 48, 828–840.

Luo, Y., Sun, M., Zhao, G.C., Li, S.Z., Xu, P., Ye, K., Xia, X.P. 2004. LAICP-MS U-Pb zircon ages of the Liaohe Group in the Eastern Block of the North China Craton: constraints on the evolution of the Jiao-Liao-Ji Belt. *Precambrian Res.* 134, 349–371.

Mao, D.B., Zhong, C.T., Chen, Z.H., Lin, Y.X., Li, H.M., and Hu, X.D., 1999, Isotopic ages and geological implications of high-pressure mafic granulites in the northern Chengdearea, HebeiProvince, China. *Acta Petrologica Sinica*, 15, 524–534.

Miladinovic, M., Cebasek, V., Gojkovic, N., 2011. Computer programs for design and modeling in mining. *Underground Mining Engineering*, 19, 109-124.

Möller, P., 1989. Magnesite-Geology, Mineralogy, Geochemistry, Formation of Mg-Carbonates. – Monograph Series on Mineral Deposits, 300 S., Borntraeger, Berlin-Stuttgart.

Möller, P., 1989. Minor and trace elements in magnesite. In: Möller P. (Eds.). *Monograph Series on Mineral Deposits* 28; 105-113.

Möller, P., Kubanek, F., 1976. Role of magnesium in nucleation processes of calcite, aragonite and dolomite. *N. Jb. Miner. Abh.* 126, 199-220.

Murphy, K., Dymond, J., 1984. Rare earth element fluxes and geochemical budget in the eastern equatorial Pacific. *Nature.* 307, 444-447

Nothdurft, L., 2001. Rare earth element geochemistry of Late Devonian reefal carbonates, Canning Basin, Western Australia: a proxy for ancient seawater chemistry. Honour thesis, Queensland University of Technology. 103.

Nozaki, Y., Zhang, J., Amakawa, H., 1997. The fractionation between Y and Ho in the marine environment. *Earth and Planetary Science Letters*. 148, 329-340.

O'Neil, J., Barnes, I., 1971. ^{13}C and ^{18}O compositions in some fresh water carbonates associated with ultramafic rocks and serpentinites; western United States. *Geochim. Cosmochim. Acta*, 35, 687-697.

O'Driscoll, M.J. (2008). "Chinese magnesia movers and shakers". *Industrial Minerals*; November 2008, pp.12-13.

Parekh, P., Möller, P., Dulski, P., Bausch, W., 1977. Distribution of trace elements between carbonate and non-carbonate phases of limestone. *Earth Planet. Sci. Lett.* 34, 39-50.

Parekh, P., Möller, P., Dulski, P., Bausch, W., 1977. Distribution of trace elements between carbonate and non-carbonate phases of limestone. *Earth Planet. Sci. Lett.* 34, 39-50.

Parente, C., Ronchi, L., Sial, A., Guillou, J., Arthaud, M., Fuzikawa, K., Verissimo, C., 2004. Geology and geochemistry of Paleoproterozoic magnesite deposits (1.8 Ga), State of Ceara, Northeastern Brazil. *Carbonates and Evaporites*. 19, 28-50.

Peng, Q., Palmer, M., 1995. The Palaeoproterozoic boron deposits in eastern Liaoning province, China metamorphosed evaporate. *Precambrian Research* 72, 185-197.

Peng, Q., Xu, H., 1994. *Palaeoproterozoic Evaporitic Sequence and Boron deposits in Jilin-Liaoning, China*. Changchun: Northeast Normal University Press.

Perry, E., Tan, F., 1972. Significance of oxygen and carbon isotope determinations in early Precambrian cherts and carbonate rocks in southern Africa. *Bull. Geol. Soc. Am.*, 83, 647-664

Pohl, W. (1992). Lagerstättenlehre. Schweizerbart Stuttgart, 504.

Ray, J., Veizer, J., Davis, W., 2003. C, O, Sr and Pb isotope systematics of carbonate sequences of the Vindhyan Supergroup, India: age, diagenesis, correlation and implications for global events. *Precambrian Research*, 121, 103-140.

Sayles, F., Fyfe, W., 1973. The crystallisation of magnesite from aqueous solution. *Geochimica Cosmochimica Acta*. 37, 87-99.

Schroll, E., 2002. Genesis of magnesite deposit in the view of isotope geochemistry. *Boletim Paranense de Geociências*, 50, 59-68. Editora UFPR.

Shen, Q.H., Qian, X.L., 1995. Archean rock assemblages, episodes and tectonic evolution of China. *Acta Geol. Sin.* 2, 113-120.

Sholkovitz, E., 1988. Rare earth elements in the sediments of the north Atlantic Ocean, Amazon delta, and East China Sea: reinterpretation of terrigenous input patterns to the oceans. *American Journal of Science*. 288, 236-281.

Spötl, C., Vennemann, T., 2003. Continuous-flow IRMS analysis of carbonate minerals. *Rapid Communications in Mass Spectrometry*, 17, 1004-1006.

Tang, H., Wu, G., Lai, Y., 2009. The C-O isotope geochemistry and genesis of the Dahiqiao magnesite deposit, Liaoning Province, NE China. *Acta Petrologica Sinica*, 25, 455-467, in Chinese.

Taylor, S., McLennan, S., 1985. *The continental Crust: Its Composition and Evolution*. Blackwell, Oxford. 312.

Tu, G., 1996. The discussion on some CO₂ problems. *Earth Science Frontiers*. 3, 53-62.

Wang, Z.H., Wilde, S.A., Wang, K.Y., and Yu, L.J., 2004. A MORB-arc basalt-adakite association in the 2.5 Ga Wutai greenstone belt. Late Archean magmatism and crustal growth in the North China Craton. *Precambrian Res.* 131, 323–343.

Weber, L., Zsak, G., Reich, C., Schatz, M., 2011. *WORLD-MINING-DATA / WELT-BERGBAU-DATEN. Minerals Production / Rohstoffproduktion, Vienna 2011, Volume 26.*

Wilson, I. & Ebner, F., 2005. A review of world's current and potential magnesite resources. *Industrial Minerals MagMin, Vienna Austria.*

Wu, J.S.; Geng, Y.S., Shen, Q.H., Liu, D.Y., Li, Z.I., Zhao, D.M., 1991. The Early Precambrian significant geological events in the North China Craton. Geological Publishing House, Beijing.

Yang, Z.S., Li, S.G., Yu, B.X., Gao, D.H., Gao, C.G. 1988. Structural deformation and mineralization in the Early Proterozoic Liaojitite suite, eastern Liaoning province, China. *Precambrian Res.* 39, 31–38.

Yin, A., Nie, S. 1996. A Phanerozoic palinspastic reconstruction of China and its neighboring regions. *The Tectonic Evolution of Asia*, Yin, A., Harrison, T.M. (eds). Cambridge University Press: New York; 442–485.

Yin, C.Q., Zhao, G.C., Sun, M., Xia, X.P., Wei, C.J., Leung, W.H., 2009. LA-ICP-MS U-Pb zircon ages of the Qianlishan Complex: Constraints on the evolution of the Khondalite Belt in the Western Block of the North China Craton. *Precambrian Res.* 174, 78–94.

Zachmann, D., (1989). Mg-carbonate deposit in freshwater environment. In: *Magnesite. Geology, Mineralogy, Geochemistry, Formation of Mg-Carbonates* (Ed. P. Möller). *Monogr. Ser. Mineral Deposits*, 28, 61-94.

Zhang, Q., 1984. Geology and metallogeny of the Early Precambrian in China. Jilin Peoples Publishing House, Changchun, China. 300-336, in Chinese.

Zhang, Q.S., Yang, Z.S. 1988. Early Crust and Mineral Deposits of Liaodong Peninsula, China. Geological Publishing House, Beijing. 218–450, in Chinese with English Abstract.

Zhang, S., 1996. The study of Minerogenic Series of Nonmetallic Deposits in Magnesian Marble Formation in Southwest Henan Province. Beijing: Geo. Publ. House.

Zhao, G.C., He, Y.H., Sun, M., 2009a. Xiong'er volcanic belt in the North China Craton: Implications for the outward accretion of the Paleo-Mesoproterozoic Columbia (Nuna) Supercontinent: *Gondwana Res.* 16, 170–181.

Zhao, G.C., Li, S.Z., Sun, M., Wilde, S.A., 2011. Assembly, accretion, and break-up of the Paleo-Mesoproterozoic Columbia supercontinent: record in the North China Craton revisited. *Int. Geol. Rev.* 53, 1331-1356.

Zhao, G.C., Sun, M., Wilde, S.A., Li, S.Z., 2005. Late Archean to Paleoproterozoic evolution of the North China Craton: Key issues revisited. *Precambrian Res.* 136, 177-202.

Zhao, G.C., Wilde, S.A., Cawood, P.A., Lu, L.Z., 1998. Thermal Evolution of Archean basement rocks from the eastern part of the North China Craton and its bearing on tectonic setting. *International Geological Review* 40, 706-721.

Zhao, G.C., Wilde, S.A., Cawood, P.A., Sun, M., 2001. Archean blocks and their boundaries in the north China Craton: lithological, geochemical, structural and P-T path constraints and tectonic evolution. *Precambrian Res.* 107, 45-73.